2015

Attosecond Transient Absorption in Gases and High Harmonic Generation in Solids

Mengxi Wu
Louisiana State University and Agricultural and Mechanical College

ATTOSECOND TRANSIENT ABSORPTION IN GASES AND HIGH HARMONIC GENERATION IN SOLIDS

A Dissertation

Submitted to the Graduate Faculty of the
Louisiana State University and
Agricultural and Mechanical College
in partial fulfillment of the
requirements for the degree of
Doctor of Philosophy

in

The Department of Physics and Astronomy

by
Mengxi Wu
BS, Huazhong University of Science and Technology, 2009
August 2015

Acknowledgements

I would never have been able to finish my dissertation without the guidance of my committee members, help from friends, and support from my family.

First and foremost I wish to thank my advisors, professor Kenneth Schafer and professor Mette Gaarde for their guidance, patience and caring in supervising my research. Thanks to them I had the opportunities to collaborate with many different groups around the world and to learn from different people from conferences and workshops. I feel deeply grateful and extreme lucky to have the opportunities to have Ken and Mette as my advisors.

This dissertation would not be possible without help from my colleagues and friends in our group. I wish to especially thank Shaohao Chen, the former postdoc in our group, who helped me tremendously in my research. I also thank my officemate Seth Camp, Renate Pazourek and Xiaoxu Guan for their support and encouragement and for many helpful discussions.

I also wish to thank my friends outside the group. I thank Enzhi Li whom I have had countless discussions about physics and life in general. And I also wish to thank Jianping Lai, Yun Ding, who have always supported me and willing to help me. And also Bin Yang, my best friend in college, and Wei Wang my new friend mete at the conference.

And finally I thank my girlfriend Liuli Huang for her love and support in all the good and bad days.

Preface

The work presented in this thesis has been done at the Department of Physics and Astronomy, Louisiana State University, under the supervision of Dr. Kenneth Schafer and Dr. Mette Gaarde. This thesis is divided into two parts, corresponding to the two different subjects I have studied during my time in graduate school. The first part of the thesis focuses on attosecond transient absorption in gases, while the second part focuses on high harmonic generation in solids.

Attosecond transient absorption is a very new subject, with the first experimental demonstration in 2007. It is an all optical method to measure electron dynamics at the sub-femtosecond time scale using an attosecond extreme ultraviolet (XUV) pulse and a synchronized infrared (IR) pulse. I have studied attosecond transient absorption using a variety of methods from full solution of the time-dependent Schrödinger equation (TDSE) to few-level models and Floquet theory, in order to put forward a time-dependent picture of the absorption process. In this thesis, I give an introduction to attosecond transient absorption in Chapter 1. In Chapter 2, I discuss the transient absorption process when the IR wavelength is near resonant to an atomic transition. In Chapter 3, I discuss the use of second order perturbation theory to calculate transient absorption and its domain of applicability to transient absorption. Finally, the Floquet picture, which uses a steady state description of laser-dressed absorption, is discussed in Chapter 4. The theory work presented in these chapters are part of an experiment/theory collaboration with Stephen Leone's group at University of California Berkley, Ursula Keller's group at Institute of Quantum Electronics at ETH and Giuseppe Sansone's group at Politecnico Milano.

An even newer subject is high harmonics generation (HHG) in transparent solids, which was first reported in 2010. In chapter 5, I give an introduction to HHG in solids. In chapter 6, I discuss the band structure in field-free solids, and interaction of a solid with a DC field is discussed in Chapter 7. In chapter 8, the HHG generation in a solid with an AC field is discussed. My work on HHG in solid presented in this thesis has been part of the theory and experiment collaberation with David Reis and Shambhu Ghimire's group at Stanford University.

Parts of the work presented in this thesis have appeared in the following publications:

- M. Wu, S. Chen, M. Gaarde, and K. Schafer, *Time-domain perspective on Autler-Townes splitting in attosecond transient absorption of laser-dressed helium atoms*, Phys. Rev. A 88, 043416 (2013). Parts of Chapter 2 are based on this publication.
- S. Chen, M. Wu, M. Gaarde, and K. Schafer, *Laser-imposed phase in resonant absorption of an isolated attosecond pulse*, Phys. Rev. A 88, 033409 (2013). Parts of Chapter 3 are based on this publication.
- M. Reduzzi, J. Hummert, A. Dubrouil, F. Calegari, M. Nisoli, F. Frassetto, L. Poletto, S. Chen, M. Wu, M. Gaarde, K. Schafer, G. Sansone, *Polarization-*

control of absorption of virtual dressed-states in helium, submitted to Phys. Rev. A. Parts of Chapter 4 are based on this publication.

- M. Wu, S. Ghimire, D. Reis, K. Schafer, and M. Gaarde, *High-harmonic generation from Bloch electrons in solids*, Phys. Rev. A 91, 043839 (2015). Parts of Chapters 5-8 are based on this publication.

Besides the above publications that are directly related to the chapters in this thesis, I have also contributed to the follow publications that have led to many of the ideas in this thesis:

- S. Chen, M. Bell, A. Beck, H. Mashiko, M. Wu, A. Pfeiffer, M. Gaarde, D. Neumark, S. Leone, and K. Schafer, *Light-induced states in attosecond transient absorption spectra of laser-dressed helium*, Phys. Rev. A 86, 063408 (2012).

- M. Wu, S. Chen, K. Schafer, and M. Gaarde, *Ultrafast time-dependent absorption in a macroscopic three-level helium gas*, Phys. Rev. A 87, 013828 (2013).

- S. Chen, M. Wu, M. Gaarde, and K. Schafer, *Quantum interference in attosecond transient absorption of laser-dressed helium atoms*, Phys. Rev. A 87, 033408 (2013).

- A. Beck, B. Bernhardt, E. Warrick, M. Wu, S. Chen, M. Gaarde, K. Schafer, D. Neumark, and S. Leone, *Attosecond transient absorption probing of electronic superpositions of bound states in neon: detection of quantum beats*, New J. Phys. 16, 113016 (2014).

- J. Herrmann, M. Lucchini, S. Chen, M. Wu, A. Ludwig, L. Kasmi, K. Schafer, L. Gallmann, M. Gaarde, and U. Keller, *Multiphoton transitions for delay-zero calibration in attosecond spectroscopy*, New J. Phys. 17, 013007 (2015).

Table of Contents

List of Figures

Abstract

We present a theoretical study of attosecond transient absorption in gases and high harmonic generation in solids. In this thesis, different features in the attosecond transient absorption laser-dressed spectrum are studied, including features near bright (dipole allowed) atomic states and features that appear approximately one or two laser photons away from the bright states due to the laser-induced coupling to dark (non-dipole allowed) states. The calculations are carried out using both numerical and analytic solutions to the time-dependent Schrödinger equation (TDSE). From these solutions, several models of time-dependent absorption and electron dynamics at the femtosecond time scale are presented. We discuss transient absorption in two different regimes: a resonant regime when the dressing field resonantly couples bright and dark states; and a non-resonant regime when the dressed states are detuned. Moreover, a Floquet picture of the transient absorption process is presented, in which the different features in the absorption spectrum are explained as the Floquet states induced by the strong probe pulse. We demonstrate that this Floquet picture applies even though dressing field lasts only a few cycles.

We also present a theoretical study of high harmonic generation (HHG) by Bloch electrons in a model transparent solid. This model applies to the recent experiments in ZnO. We solve the TDSE using a velocity gauge numerical method and the resulting harmonic spectrum exhibits a plateau due to the coupling of the valence band to the first conduction band. The energy cutoff of the plateau scales linearly with field strength, which agrees with the ZnO experiment. To facilitate the analysis of the time-frequency characteristics of the emitted harmonics, the TDSE is also solved in the so-called Houston basis which allows the separation of the interband and intraband contributions to the time-dependent current. The interband and intraband transitions are shown to correspond to diabatic and adiabatic dynamics of the system, respectively. The contributions from interband and intraband display very different time-frequency characteristics, which can potentially be used as an experimental signature of the intraband and interband dynamics.

Part I
Attosecond Transient Absorption

Chapter 1
Introduction to transient absorption

1.1 Introduction to attosecond transient absorption

With the breaking of the femtosecond barrier, attosecond pulses arrived with the new millennium [1–3]. The pursuit of attosecond pulses dates back to the early 1990s when researchers discovered high-harmonic generation (HHG) [4, 5], in which extreme ultraviolet radiation was found to be emitted from an inert gas when illuminated with intense infrared laser pulses. The physical mechanism of HHG is explained by a semi-classical model, where the electron is first tunnel ionized from the atom and accelerated in the laser field, and then recaptured by the core [6, 7]. In 2001, the first attosecond pulse train was demonstrated experimentally through the HHG process, and later in the same year, an isolated attosecond pulse was reported [8, 9].

Attosecond pulses have proven to be a very useful source of XUV radiation [10, 11]. From a fundamental physics point of view, they allow us to study ever faster dynamics in atoms and molecules. While picosecond pulses reveal molecular rotation and femtosecond pulses capture molecular vibrations, attosecond pulses enable us to observe or even control the electron motion [12–16], which is the fastest motion outside the atomic nucleus. Along with the birth of attosecond pulses comes many novel technologies and applications. For example, coherent short X-ray pulses have already been used in protein crystallography by so called "diffraction before destruction" techniques [17–20]. Moreover, attosecond pulses have been demonstrated to be able to control the conductivity of a semiconductor during one laser cycle, which can be potentially used to produce peta-Hertz transistors [21, 22].

Many attosecond studies involve a time-resolved spectroscopy called transient absorption, where the absorbance at a particular wavelength of a sample is measured as a function of time after an ultrashort pulse excites the system [10, 23–25] . Since the ultrashort pump pulse comes from the generated harmonics that are locked in phase with the driving field, the pump and probe pulses are naturally synchronized. This automatic synchronization is one of the reasons that this particular pump-probe scheme is widely used. A typical attosecond transient absorption setup is shown in Fig 1.1. A strong infrared (IR) pulse is split into two beams. One beam is used as the probe beam, and the other goes through a HHG process and creates a short, extreme ultraviolet (XUV) pulse as the pump beam. The pump pulse excites the material to some transient excited state, which is then probed by the IR probe pulse, and the delay-dependent absorption of the pump pulse is measured.

The difference of arrival time between the pump and probe pulses can be varied with attosecond precision and a delay dependent absorption spectrum can be recorded. Although the detector measures a time-integrated quantity, by control-

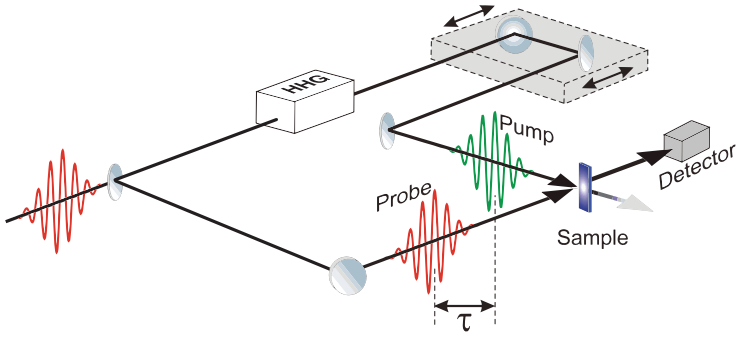

Figure 1.1: A typical transient absorption experiment setup. A strong IR pulse is split into two beams. One beam is used directly as the probe pulse, generates XUV harmonics which are used as the probe pulse. The delay between the pump and probe pulses can be varied, which results in a time-dependent absorption spectrum being recorded at the detector. Adapted from [26] with permission from the European Society for Photobiology, the European Photochemistry Association, and The Royal Society of Chemistry.

ling the delay between pump and probe pulses, the information of the dynamics is encoded into the delay dependent transient absorption spectrum. One of our main tasks is then to deconvolve this absorption spectrum and retrieve the time evolution history of the system. This deconvolution is very much like the process of cracking of encryption algorithms in cryptography. Given an cryptographic encryption module, a cryptanalyst can change the input slightly each time and get a serials of output that depends on the inputs. Then by comparing these outputs, the cryptanalyst may reconstruct the algorithm used in the encryption. The change of input is like the varying the delay between the two pulses, while the algorithm the cryptanalyst tries to reconstruct is like the laser-material dynamics in our transient absorption system.

Recent experimental and theoretical studies [22, 25, 27–35] have revealed many interesting dynamics of the laser-material system. One area that has been extensively studied is the light induced structures (LISs) in transient absorption spectra. In a joint theory and experiment study of transient absorption in a helium gas, Chen *et. al.* [36] showed that LISs can be seen in the absorption spectrum, at energies that are not allowed in the laser-free atom. They showed that the LISs come from the coupling between the dipole allowed states to the nearby dipole forbidden states. Following this study, Chen *et. al.* [37] studied the strong sub-IR-cycle modulations near the ionization threshold. They showed that these structures come from the interference between direct and indirect pathways to excited states. Later in the same year, Klünder *et. al.* [38] demonstrated theoretically that these subcycle structures from the direct and indirect pathways are also present in the photoelectron spectrum from helium atoms, and that they can be used to retrieve the phases of all the states that make up the wave packets. Another area that has been studied greatly is the modification of the absorption line shape of the atomic state in the regime where

the pump and probe pulses overlaps. Recent work from Pfeifer's group [30] showed experimentally that the line shape of the atomic states change between Lorentzian-like and Fano-like as the delay between the pump and probe changes, and that these changes can be explained using a simple laser induced phase model [33] . In the following papers in 2014 [34], they pushed this idea further and demonstrated the possibility of using the laser induced phase to reconstruct the dynamics of the two-electron wave packet from the transient absorption spectrum. Besides, there are many other areas have been studied. For example, quantum beating in transient absorption, transient absorption near autoionizing states which can be used to extract their lifetimes [39], transient absorption in the near-resonant case where time-dependent Autler-Townes splitting features can be observed [40], quarter-cycle oscillations in transient absorption for the use of calibration of the delay-zero in the experiment [41], etc.

1.2 Theoretical calculation of the transient absorption spectrum

In order to theoretically calculate the transient probability, we first solve the time-dependent Schrödinger equation (TDSE) for a laser coupled He atom, using the single active electron (SAE) approximation [42, 43]. Then the transient absorption spectrum can be expressed as a single atom response function which is related to the time-dependent dipole moment. The TDSE for a laser coupled atom is

$$i\hbar|\dot{\psi}\rangle = \hat{H}|\psi\rangle, \tag{1.1}$$

where $\hat{H}$ is the Hamiltonian

$$\hat{H} = \hat{H}_A + \mathcal{E}(t)\,\hat{z}, \tag{1.2}$$

and $\hat{H}_A$ is the atomic Hamiltonian, $\mathcal{E}(t)$ is the electric field and $\hat{z}$ is the position operator. The rate of energy gain by the single atom can be written as

$$\frac{dE}{dt} = \frac{d}{dt}\langle\psi|\hat{H}|\psi\rangle. \tag{1.3}$$

Then the single atom response function can be derived by equating the total energy gained by the atom ΔE with the excitation probability via the relation

$$\Delta E = \int \frac{dE}{dt}\,dt = \int \omega\,\widetilde{S}(\omega)\,d\omega, \tag{1.4}$$

where $\widetilde{S}(\omega)$ is the response function we are aiming for. And we have

$$\frac{dE}{dt} = \frac{d}{dt}\langle\psi|H|\psi\rangle \tag{1.5}$$

$$= \langle\dot{\psi}|H|\psi\rangle + \langle\psi|H|\dot{\psi}\rangle + \langle\psi|\frac{\partial H}{\partial t}|\psi\rangle \tag{1.6}$$

$$= \langle z\rangle\frac{\partial\mathcal{E}}{\partial t}, \tag{1.7}$$

where we have denote $\langle z\rangle$(t) by $z(t)$. Then the energy gained by the atom can be further written as

$$\Delta E = \int_{-\infty}^{\infty} z(t)\frac{\partial \mathcal{E}}{\partial t}\,dt \tag{1.8}$$

$$= \frac{1}{2\pi}\int_{-\infty}^{\infty} \tilde{z}(\omega)(-i\omega')\mathcal{E}(\omega')e^{-i(\omega+\omega')t}\,dt\,d\omega\,d\omega' \tag{1.9}$$

$$= \int_{-\infty}^{\infty} i\omega\,\tilde{z}(\omega)\widetilde{\mathcal{E}}(-\omega)\,d\omega \tag{1.10}$$

$$= \int_{-\infty}^{\infty} i\omega\,\tilde{z}(\omega)\widetilde{\mathcal{E}}^*(\omega)\,d\omega. \tag{1.11}$$

If $f(\omega) = i\omega\tilde{z}(\omega)\widetilde{\mathcal{E}}^*(\omega)$ then clearly $f(-\omega) = f^*(\omega)$ and we have therefore

$$\Delta E = \int_0^{\infty} 2\,\mathrm{Re}\Big\{i\omega\,\tilde{z}(\omega)\widetilde{\mathcal{E}}^*(\omega)\Big\}\,d\omega \tag{1.12}$$

$$= \int_0^{\infty} -\omega\,2\,\mathrm{Im}\Big\{\tilde{z}(\omega)\widetilde{\mathcal{E}}^*(\omega)\Big\}\,d\omega. \tag{1.13}$$

So finally we can write down the response function as

$$\widetilde{S}_+(\omega) = -2\,\mathrm{Im}\Big[\tilde{z}(\omega)\widetilde{\mathcal{E}}^*(\omega)\Big] \qquad \omega > 0. \tag{1.14}$$

Since the position of the electron is related to the dipole moment by $d(t) = -z(t)$ in atomic units, the response function is related to the dipole moment and the pump electric field by

$$\tilde{S}(\omega) = 2\ \mathrm{Im}\left[\tilde{d}(\omega)\widetilde{\mathcal{E}}^*(\omega)\right]. \tag{1.15}$$

The response function $\tilde{S}(\omega)$ defined this way represents the absorption probability density at a certain frequency, so that positive (negative) $\omega\tilde{S}(\omega)$ equals the amount of energy gained (lost) by the atom per unit frequency at ω. A typical transient absorption spectrum calculated using the response function is shown in Fig. 1.2.

1.3 Basic pictures

In this last section of this introduction, we will try to establish some basic pictures for transient absorption, which we believe are very helpful in understanding transient absorption.

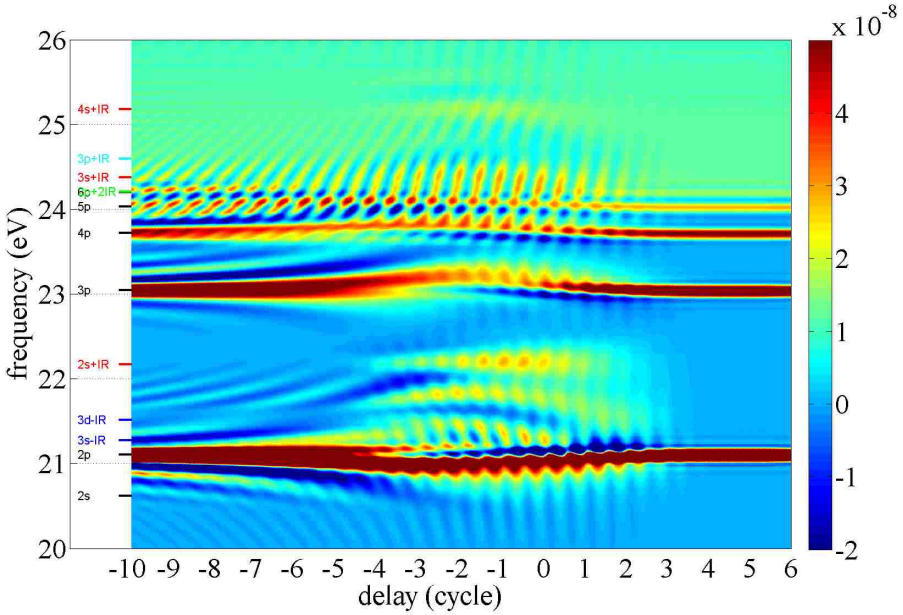

Figure 1.2: A transient absorption spectrum of helium is calculated. This time-dependent absorption spectrum contains the time information of the system evolution. Reprinted from [37] with permission.

1.3.1 Short pulse as a time starter

In a typical transient absorption setup, the pump pulse usually has a duration of a few hundreds attosecond and a central energy of a few tens of eV, while the probe pulse usually has a duration of a few tens of femtosecond and a central frequency of about 1 eV. The dramatic differences in the duration and central frequency of the pump and probe pulses suggest two important points about the system dynamics. First of all, the very different central frequencies dictate that dynamics induced by the pump and probe pulses are on different time scales. The pump pulse couples the ground state and the dipole allowed excited states (also known as bright states) which are a few tens of eV apart, while the probe pulse couples those excited states to the nearby excited states (also known as dark states because they are not coupled to the ground state by the field) which are about 1 eV apart. In this sense, the system dynamics separates into two parts

$$f(t) = f_{\text{fast}}(t) \times f_{\text{slow}}(t), \tag{1.16}$$

where $f_{\text{fast}}(t)$ and $f_{\text{slow}}(t)$ denote the fast and slow dynamics introduced by the pump and probe pulses, respectively. Moreover, since the probe pulse cannot excite the ground state, the start of the system dynamics only relies on the pump pulse. No matter what the delay between the two pulses is, the system dynamics always start at the time when the pump pulse arrives. Combining these two ideas, we get a picture of the system dynamics: The pump pulse excites population from the ground state to the bright states and starts the fast system dynamics. The probe pulse couples the bright states to nearby darks states and introduce a slow dynamics

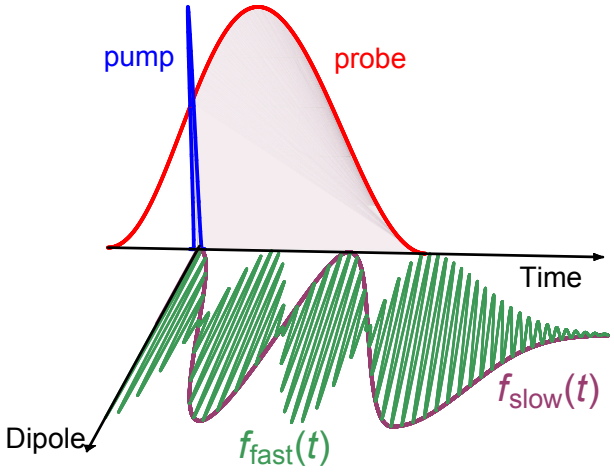

Figure 1.3: Schematic plot of the dynamics introduced by the pump and probe pulses. The short pump pulse starts the fast system dynamics and the probe pulse modifies this dynamics at a longer time scale. Reprinted from [40] with permission.

on top of the fast one. A schematic plot of this process is shown in Fig. 1.3. As we will show in the following section, usually the fast dynamics f_{fast} involves only the natural oscillation of the bright states and thus becomes trivial. In this sense, the dynamics of the system is mostly determined by f_{slow} which is the dynamics induced by the probe pulse.

1.3.2 Waiting time – all about phases

In a transient absorption setup, the frequency-dependent absorption is recorded as a function of delay, and the system dynamics is encoded in the delay dependent spectrum. From the simple picture we described above, varying the delay between the two pulses has two combined effects. The first effect is that the system sees different pulses at different delays. This is because the system dynamics starts only after the pump pulse arrives, so that the system is transparent to the part of the probe pulse that arrives before the pump pulse. This is the most dominant effect in the overlap regime, where the absorption spectrum changes dramatically with delay. The second effect of varying the delay is the change of the waiting time between the excitation of the bright state population and its manipulation by the probe pulse. During this waiting time, the population gains a phase that is proportional to the waiting time. So in the time domain, the dynamics induced by the probe pulse will have a frequency dependent phase

$$f_{\text{slow}}(t-\tau) = e^{-i\omega\tau} f_{\text{slow}}(t), \tag{1.17}$$

while in the spectrum, this phase gives a delay dependent phase factor

$$\mathscr{F}\left[f_{\text{slow}}(t-\tau)\right] = e^{-i\omega\tau}\mathscr{F}\left[f_{\text{slow}}(t)\right], \tag{1.18}$$

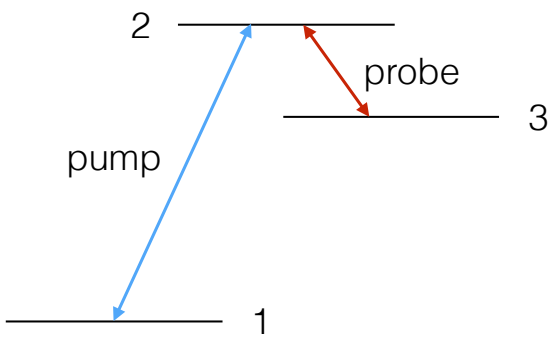

Figure 1.4: A transient absorption system involving three states. State 1 and 2 are coupled by the pump pulse, and state 2 and 3 are coupled by the probe pulse.

where $\mathscr{F}$ denotes the Fourier transform. Since the transient probability is proportional to the imaginary part of the electric field spectrum as shown in Eq.(1.15), this delay dependent phase factor will show up in the absorption spectrum as a family of stripes that satisfies

$$|\omega \cdot \tau| = \text{constant}, \tag{1.19}$$

where τ is the delay and ω is the frequency of in the absorption spectrum. In Fourier transform nuclear magnetic resonance spectroscopy, this phenomenon is well-known as the "perturbed free induction decay" [44, 45].

1.3.3 Primitive – two-level system

For a complicated system that is controlled by multiple parameters, it is usually beneficial to identify the primitives of that system. The primitives should capture most of the important characteristics of the system in the simplest possible form. Then after a thorough understanding of the primitives, they will act like an island from where we can start to explore the sea of parameters. If we are successful in identifying and understanding the primitives, then we can have a very general theory that applies to not only the phenomena we started from, but many more. [46]. For transient absorption, a two-level system is one such primitive.

In the simplest form of transient absorption, we consider a three-level system coupled by two laser pulses, as shown in Fig. 1.4. The short pump pulse couples states 1 and 2 and the probe pulse couples states 2 and 3. Then the absorption spectrum can be calculated using the response function in Eq. (1.15). Since the response is mainly near the pump frequency, the total electric field in Eq. (1.15) can be replaced by the electric field of the pump pulse only. Moreover, since the pump pulse is usually very short, it can be approximately by a delta function with its strength proportional to the pulse area. With these approximations, the response function can be simplified as

$$\tilde{S}(\omega) = 2A_{\text{pump}} \operatorname{Im}[\tilde{d}(\omega)], \tag{1.20}$$

where A_{pump} is the pulse area of the pump pulse. With the delta function approximation of the pump pulse, the initial population excited by the pump pulse will then be delay independent. This means that the initial condition for the coupling between states 2 and 3 is also delay independent. Thus the three-level system can be further simplified into a two-level system involving only state 2 and 3 and the probe pulse. So in this sense, the simplest transient absorption system is a two-level system driven by a single probe pulse. In the following chapters, we will explore more about this two-level primitive.

In summary, in this introductory chapter, we discussed the background of transient absorption and its basic experimental setup. We also discussed the theoretical approaches to calculate the transient absorption spectrum that is comparable to experiments. Finally, we established some basic pictures for transient absorption process. In the following chapters, we will continue to develop these methods and pictures, and apply them to some concrete examples of transient absorption. Specifically, we will discuss a near resonant coupling case in helium in chapter 2 and a detuned case in chapter 3.

Chapter 2
Rabi oscillations and coherence control in transient absorption

2.1 Introduction

In the previous section, we gave an brief introduction to transient absorption. We briefly described the theoretical method of calculating the transient absorption spectrum and established some basis pictures for the transient absorption process. In this chapter, we will discuss in detail the transient absorption in the resonant regime where the wavelength of the IR laser is near resonant with an atomic transition, and leave the detuned regime to the next chapter.

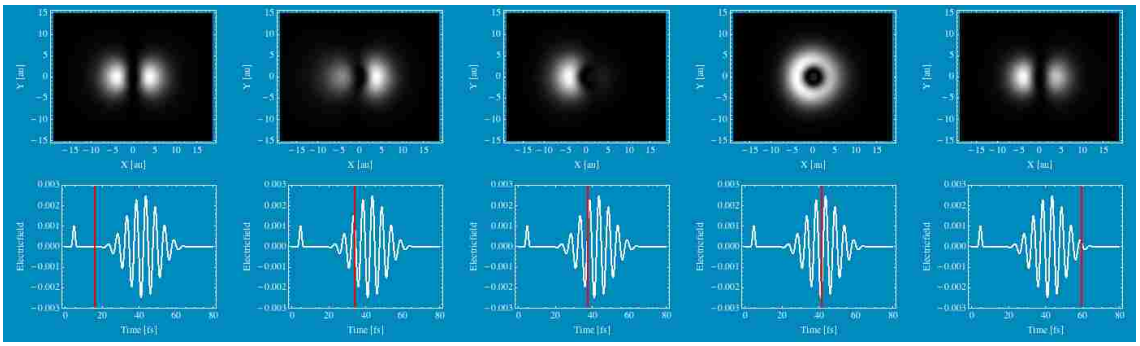

Figure 2.1: The wave function evolution (upper panel) for a large negative delay where the XUV pulse is leading the IR pulse (lower panel). The upper panel shows the wave functions at certain times that are indicated by the vertical line in the lower panel. The IR pulse is resonant with the helium 1s-2p transition and we see a complete Rabi oscillation in the wave function evolution.

When the laser is near resonant with the atomic transition, the laser-atom interaction can be described in terms of Rabi oscillations, in which the laser drives the population cyclically through the atomic states it couples. As an example, Fig. 2.1 shows the wave function evolution of a helium atom when excited by an XUV pulse followed by an IR pulse, calculated by solving the TDSE. The IR pulse resonantly couples the helium 2p and 2s state and has a pulse area of 2π, where the pulse area is defined by the integration of the pulse envelope $A = \int_{-\infty}^{\infty} \mathcal{E}_{\text{env}}(t)dt$ [47]. As shown in Fig. 2.1, the XUV pulse first excites the atom from the ground 1s state (not plotted) into the 2p state, then the 2π IR pulse arrives and drives the atom into 2s state and back to the 2p state, making the atom perform a complete cycle of Rabi oscillation.

A typical transient absorption spectrum for a resonant case is shown in Fig. 2.2(a), where the 2s-2p state is resonantly coupled by a 2250 nm IR pulse with 34 fs in FWHM and an intensity of 3.0×10^{12} W/cm^2. From the absorption spectrum we can see several interesting features. The most dominant one is the fork-like structure around 21.1 eV, where the $2p$ absorption line is split into two curved lines above and below the resonant frequency when the XUV and IR overlap. This structure is very similar to the ordinary Autler-Townes (AT) structure where an atomic spectral line is split by a resonant oscillating electric field [48], except the spacing between the two features depends on the IR intensity and thus changes with delay as the delay is scanned. Inside the AT splitting structure, there are also fork like structures going from positive to negative delays. Moreover, at large negative delays ($\tau < -5$ cycles), where the XUV pulse leads the IR pulse, there are hyperbolic sidebands near the $2p$ resonant line. These structures have also been seen recently in the absorption spectrum of a laser coupled an autoionizing system [29]. In addition, in the region above and below the main AT splitting structure, namely above 21.5 eV and below 20.5 eV, we can see vertical stripes across the delay scan.

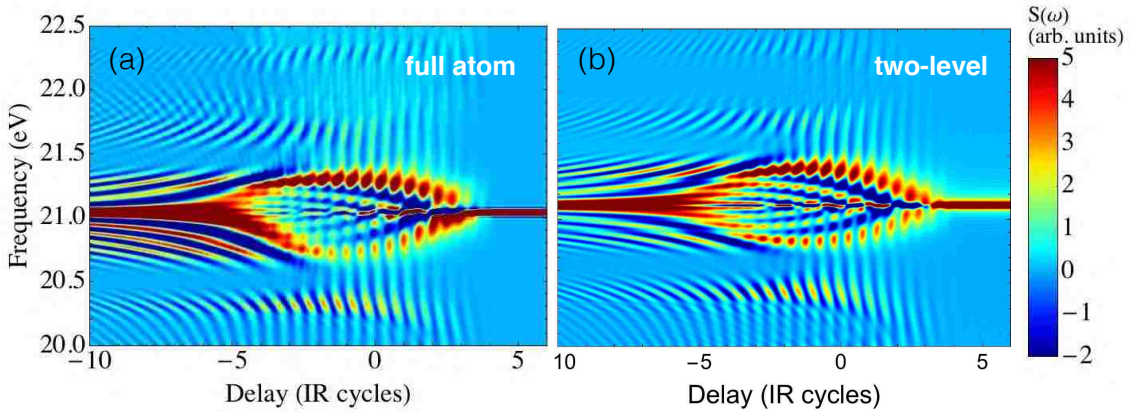

Figure 2.2: (a) Full TDSE calculation of the transient absorption spectrum of helium atom dressed by a two color field. The XUV pulse has a FWHM duration of 356 as, centered at 25 eV. The IR pulse has a duration of 34 fs and a wavelength 2550 nm which is resonant with the $2p-2s$ transition. (b) The transient absorption spectrum for 2p-2s two-level system driven by the same IR pulse. The two-level calculation reproduces many of the features of the full calculation. reprinted from [40] with permission.

In this resonant case, the IR pulse is resonant with the helium $2p-2s$ energy, so that the atomic response near 21 eV is dominated by the $1s-2s-2p$ three level dynamics. In this sense, we can use only the lowest three levels $1s-2p-2s$ to approximate the dynamics of the field and the helium atom, ignoring all the higher energy states. Moreover, since the XUV pulse is short and weak in our case, we can approximate it as a delta function with its strength proportional to the pulse area of the full XUV field. With these approximations, the resonant coupling of the helium atom and the laser pulses can be simplified to an effective two-level system. The absorption spectrum calculated using this effective two-level system is

shown in Fig. 2.2(b). Comparing Fig. 2.2(b) to Fig. 2.2(a), we see that the two-level model reproduces many features in the absorption spectrum of the full atom. Thus, this two-level calculation result will be the starting point for our discussion in this chapter. In the remainder of this chapter, we will devote ourselves to understand the different features in Fig. 2.2(b). We will show that the main structure is due to the Rabi oscillations between the 2p and 2s states while the stripes and the 2ω oscillations come from the effects of the counter-rotating terms (CRT) in the Hamiltonian.

2.2 Rabi oscillations in a two-level system

In this section, we will set up the formalism of Rabi oscillations in a the 2p-2s two-level system, and will show that the main structures in the absorption spectrum can be understood using Rabi oscillations.

In the rotating wave approximation (RWA) [49], the two-level TDSE reads

$$i\dot{C}_{2s} = \frac{1}{2}\Omega(t,\tau)\ C_{2p}, \tag{2.1a}$$

$$i\dot{C}_{2p} = \frac{1}{2}\Omega(t,\tau)\ C_{2s}, \tag{2.1b}$$

with the initial condition of

$$C_{2s}(0,\tau) = 0, \tag{2.2a}$$

$$C_{2p}(0,\tau) = C^0_{2p}, \tag{2.2b}$$

where C^0_{2p} is the initial amplitude of the $2p$ state excited by the XUV pulse, and $\Omega(t,\tau)$ is the time-dependent Rabi frequency whose expression will be given below. This equation has the analytical solution:

$$C_{2s}(t,\tau) = -iC^0_{2p}\sin\frac{\phi(t,\tau)}{2}, \tag{2.3a}$$

$$C_{2p}(t,\tau) = C^0_{2p}\cos\frac{\phi(t,\tau)}{2}, \tag{2.3b}$$

where

$$\phi(t,\tau) = \int_0^t \Omega(t',\tau)dt'. \tag{2.4}$$

Next, consider an IR pulse that has an envelope of $\cos^2$, so that the delay-dependent IR electric field is

$$\mathcal{E}_{IR}(t,\tau) = \begin{cases} \mathcal{E}^0_{IR}\cos^2\frac{\omega(t-\tau)}{2n}\sin\left[\omega(t-\tau)\right] & 0 \le t \le \frac{\pi n}{\omega} + \tau \\ 0 & \frac{\pi n}{\omega} + \tau < t, \end{cases} \tag{2.5}$$

and the time- and delay-dependent Rabi frequency is

$$\Omega(t,\tau) = \begin{cases} \Omega_0 \cos^2 \frac{\omega(t-\tau)}{2n} & 0 \le t \le \frac{\pi n}{\omega} + \tau \\ 0 & \frac{\pi n}{\omega} + \tau < t, \end{cases} \tag{2.6}$$

where $\Omega_0 = \mu_1 \mathcal{E}^0_{IR}$ is the peak Rabi frequency, μ_1 is the dipole matrix element between the 2p and 2s state, n is the number of cycles in the full IR pulse and τ is the delay between the XUV pulse and the IR pulse. In these expressions, we have set time zero to be the time when the XUV pulse arrives, before which the C_{2p} is always zero. Substituting Eq. (2.6) into Eq. (2.3) we obtain an analytical expression for the delay-dependent state amplitude:

$$C_{2p}(t,\tau) = \begin{cases} C^0_{2p} \cos\left[\frac{\Omega_0}{4\omega}\left(\omega t + n\,\sin\frac{\omega\tau}{n} + n\,\sin\frac{\omega(t-\tau)}{n}\right)\right] & 0 \le t \le \frac{\pi n}{\omega} + \tau \\ C^0_{2p} \cos\left[\frac{\Omega_0}{4\omega}\left(n\pi + \omega\tau + n\sin\frac{\omega\tau}{n}\right)\right] & \frac{\pi n}{\omega} + \tau < t. \end{cases} \tag{2.7}$$

Then the time-dependent dipole moment can be calculated by

$$d(t,\tau) = \mu_0 C^*_{1s}(t,\tau) C_{2p}(t,\tau) e^{-i\omega_0 t} + c.c \tag{2.8}$$

where μ_0 is the dipole transition element between the $1s-2p$ states. C_{1s} is the amplitude of the $1s$ state and is assumed to be always 1 since the XUV pulse is weak. The response function then can be calculated using the time-dependent dipole moment and the result is shown in Fig. 2.3(a). It looks very similar to Fig. 2.2(b) in the sense that it can reproduce the main structure and the fork like structures in that plot. The final state amplitude at the end of IR pulse can also be written down, as a function of delay:

$$C^f_{2p}(\tau) = C^0_{2p}\,\cos\left[\frac{\Omega_0}{4\omega}\left(n\pi + \omega\tau + n\,\sin\left[\frac{\omega\tau}{n}\right]\right)\right]. \tag{2.9}$$

A plot of Eq. (2.9) (normalized) is shown in Fig. 2.3(b) overlayed in white on the absorption spectrum. We see from Fig. 2.3(b) that the final state amplitude oscillates between positive and negative values, which matches well to the oscillation of the response function between absorption and emission on the $2p$ resonant line at 21.1 eV. This oscillation in final state amplitude comes from the fact that as we are scanning the XUV pulse, the remaining IR pulse area will change as a function of delay. This causes the response function to oscillate between absorption (when the $2p$ amplitude at the end of the IR pulse is large and positive) and emission (when the $2p$ amplitude at the end of the IR pulse is large and negative).

2.3 Strong driven Rabi oscillations – counter-rotating term

In the previous section, we saw that the main features of the transient absorption spectrum in Fig. 2.2 is reproduced by the Rabi oscillation model between the helium

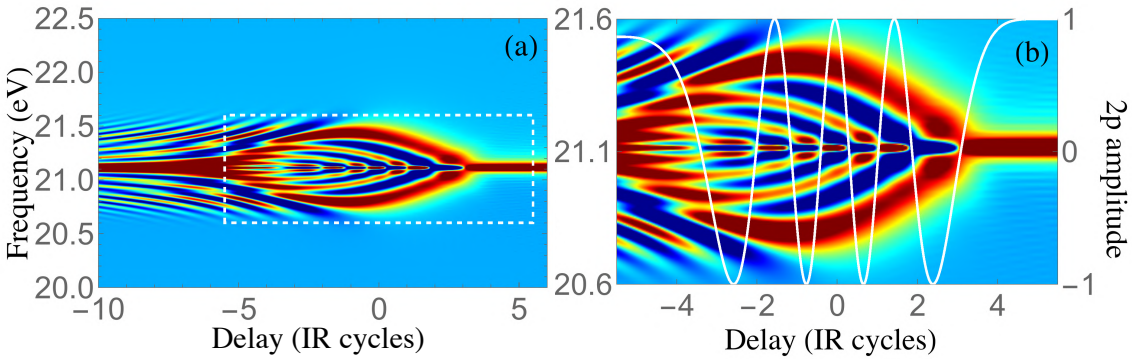

Figure 2.3: (a) Response function calculated directly from Eq.(2.7). We can see that the two-level Rabi treatment can reproduce the fork-like structure in Fig. 2.2. (b) Closeup from (a), showing that the Rabi oscillation at the resonant line matches with the oscillation of the final 2p state amplitude (white line). Adapted from [40] with permission.

2p-2s states in Fig. 2.3(a). However, the sub-cycle oscillations and the stripes above and below the main structure are not present in the simple Rabi model. In this section, we will show that those extra features are due to the CRT, and will provide a simple model to incorporate that into the Rabi model.

In the derivation of the Rabi oscillation model, we used the RWA in which the CRT are ignored. The condition for the RWA to apply is

$$\Omega << \omega, \tag{2.10}$$

which means the CRT oscillate so fast that their average contribution to the dynamics of the system is almost zero. However, in the strong coupling case, the above condition can easily be violated. For example, in the parameters of Fig. 2.2, $\Omega = 1.4\omega$, which means the effect of the CRT cannot be ignored. Indeed, the effects of the CRT are the extra features in Fig. 2.2(b) that are absent in Fig.2.3.

To confirm that the extra features come from the CRT, we change the ratio of the Rabi frequency to laser frequency by changing the laser frequency and the two level frequency at the same time, and the result is shown in Fig. 2.4. One can see that as the ratio decreases, and we thus enter the RWA regime, the 2ω features start to disappear. This is expected because we are essentially enter the RWA regime.

Now that we have identified the extra features such as sub-cycle oscillations and the stripes are due to the CRT effect, the next step is to construct a model that can take them into account. Since the CRT have a 2ω effect as we see in Fig. 2.2, we can empirically model the CRT effects by adding a term $\sin(2\omega t)$ directly into the time-dependent state amplitude in Eq. (2.7). As we have seen, the strength of the CRT may be characterized approximately by the ratio Ω/ω, since strong coupling results in large CRT effects. Combining all of these estimates, we get a

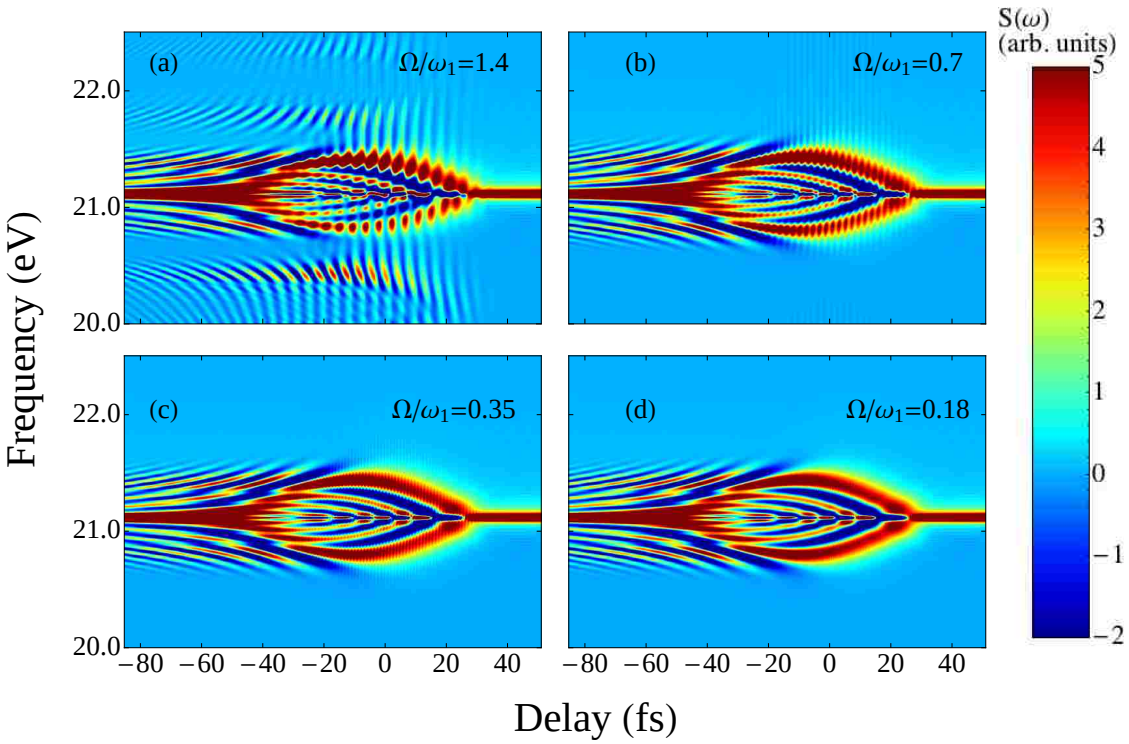

Figure 2.4: Stepping into the RWA regime as we decrease the ratio Ω/ω. Absorption spectrum for a two-level system using (a) the original $\Omega/\omega = 1.4$ (b) $\Omega/\omega = 0.7$, (c) $\Omega/\omega = 0.35$, (d) $\Omega/\omega = 0.18$. The non-RWA features such as sub-cycle oscillations and stripes are eliminated while the RWA features of the main AT splitting are preserved. reprinted from [40] with permission.

model time-dependent $2p$-amplitude:

$$\begin{aligned} C_{2p}(t,\tau) = \; & C_{2p}^{0}\cos\left[\tfrac{\Omega_0}{4\omega}\left(\omega t + n\sin\tfrac{\tau\omega}{n} + n\sin\tfrac{\omega(t-\tau)}{n}\right)\right] \\ & \times\left(1+\beta\tfrac{\Omega(t,\tau)}{\omega}\sin[2\omega(t-\tau)]\right) \end{aligned} \tag{2.11}$$

where β is a free parameter which we take to be $1/2$.

Using Eq. (2.11), we can get a model response function, as shown in Fig. 2.5. We can see that by putting in a 2ω oscillations directly into the state amplitude, the model can reproduce the striped structure outside the main AT splitting region. These stripes appear at two photons above and bellow the main AT structure (at about $\omega_0 \pm 2\omega \pm \Omega_0/2$), which is reasonable since they represent the frequency mixing of the $\Omega/2$ and 2ω components in the time-dependent dipole. Absorption (and emission) is possible at these frequencies because they are all within the broad bandwidth of the XUV pulse. Adding the 2ω component by hand to the state amplitude also generally reproduces the tilt of the sub-cycle oscillations, with a positive (negative) tilt of the stripes above (below) the AT structure. This is because

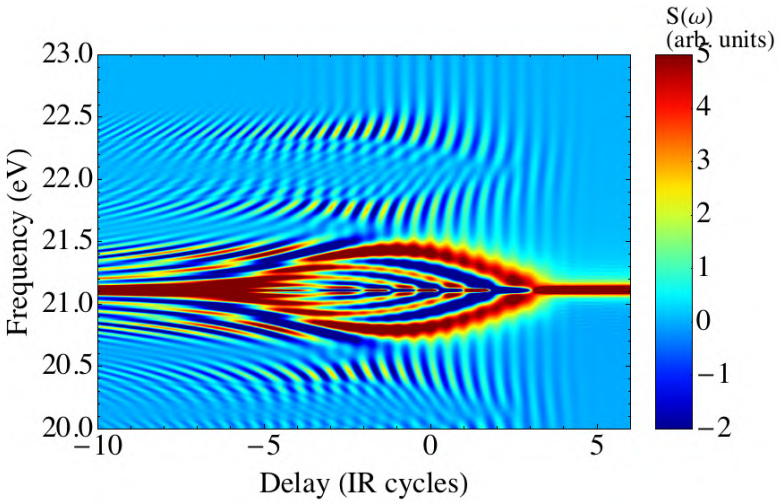

Figure 2.5: Adding 2ω oscillation directly into the time-dependent state amplitude (Eq. (2.11)) reproduces the sub-cycle oscillation and the delay-dependent stripes. These stripes can be explained as a result of frequency mixing in the dipole oscillation. reprinted from [40] with permission.

the sub-cycle oscillations originate in an interference between the excitations that are separated by 2ω, see for instance [37]. These excitations result directly from adding the (lowest-order non-linear) 2ω term to C_{2p}. We note, though, that since the simple model incorporates neither higher order terms nor the change of the effective Rabi frequency, it does not agree quantitatively with the numerical solution of the two-level system in Fig. 2.2(b), particularly on the phase of the fringes.

2.4 Summary

In this chapter, we have studied the transient absorption process for the case where the IR pulse is resonant with the 2s-2p transition. We have shown that the well-known Autler-Townes splitting of an absorption line in the presence of a resonant coupling field generalizes and becomes delay-dependent when the coupling pulse is short. We found prominent, delay-dependent interference features which lead to both absorption and emission within the AT structure. We showed that the dynamics of this delay dependence can be understood from the time-dependent population dynamics of a strongly driven two-level system. We showed that although the main AT structure and its delay-dependence is well described within the rotating-wave approximation, the full delay-dependent absorption spectrum is strongly influenced by counter-rotating terms which give rise to sub-IR-cycle oscillations as well as additional absorption lines corresponding to nonlinear mixing of the IR frequency and the Rabi frequency.

Chapter 3
Perturbation and transient population in transient absorption

In the previous chapter, we discussed the transient absorption process in a regime where the probe (IR) pulse is near resonant with the spacing between two atomic states. In that regime, the dynamics of the system can be understood mainly in terms of Rabi oscillations between those resonant states. However, in many systems, atomic couplings are more likely to be largely detuned with the laser wavelength. Specifically, in those largely detuned systems the detuning between the central frequency of the driving pulse is much larger than the bandwidth of that pulse

$$\tau_{\mathrm{IR}}|\omega_{\mathrm{pulse}} - \omega_0| \gg 1. \tag{3.1}$$

For instance, in our "standard" transient absorption calculation for helium, the left hand side of the above equation is about 15 for the 2p-2s coupling driven by a 10 fs, 800 nm IR pulse. This detuned driving accounts for the 2s light-induced states (LIS) feature at around 22.2 eV, as shown in Fig. 1.2, and repeated here in Fig. 3.1.

In this chapter, we will focus our discussion of transient absorption to the regime where Eq. 3.1 is satisfied. We will show that in this regime, perturbation theory can be used to model the transient absorption process. We will first set up the equations of perturbation theory for a two-level system. We then calculate an absorption spectrum using this formalism, and compare the result to that of a two-level TDSE calculation. From the comparison, we will show that in the large detuning regime, second order perturbation is in general a good approach to study the dynamics. Moreover, we will discuss the transient population of the dark states and show that it is connected to the final population as a function of delay. This allows us to connect our delay-dependent calculations to a time-dependent picture of absorptions.

3.1 Absorption spectrum from perturbation theory

As we have discussed in the introduction, the absorption feature near 22.2 eV in Fig. 3.1 is mainly due to the off-resonant coupling between the 2p and 2s states. So to simplify the problem, we focus only on the 1s-2p-2s three-level system. We further simplify the problem by assuming the XUV pulse is very short so that it can be approximated as a delta function, which reduces the system from three levels to 2p and 2s two levels. In the remainder of this section, we will set up a formalism using perturbation theory to calculate transient absorption in a two-level system. We will show that second order perturbation can well reproduce a two-level TDSE

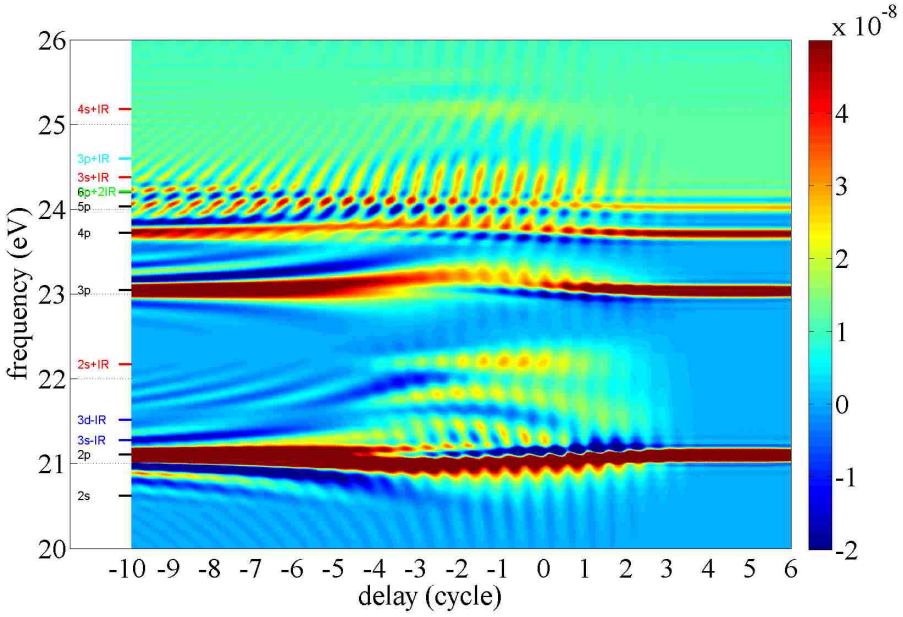

Figure 3.1: The 2s LIS at near 22.2 eV come from the off-resonant coupling between the 2p and 2s states. We will show that this feature can be explained using perturbation theory. reprinted from [37] with permission.

calculation. In particular, we will show that both calculations give rise to the 2s LIS features seen in the full calculation.

For the 2p-2s two-level system, the wave function can be written as

$$|\psi(t)\rangle = C_{2p}(t)e^{-i\omega_{2p}t}\,|2p\rangle + C_{2s}(t)e^{-i\omega_{2s}t}\,|2s\rangle\,, \tag{3.2}$$

where $C_{2p}(t)$ and $C_{2s}(t)$ are the amplitudes of $2p$ and $2s$ states, respectively. The TDSE reads

$$i\frac{\partial}{\partial t}\,|\psi(t)\rangle = \hat{H}\,|\psi(t)\rangle\,, \tag{3.3}$$

and the Hamiltonian is

$$\hat{H} = \hat{H}_0 + \mu E(t)\hat{X}, \tag{3.4}$$

where μ is the dipole transition element between the two states, $\hat{X}$ is the position operator. Then the IR pulse can be written as a smooth envelope with a carrier frequency

$$E(t) = f(t)\cos(\omega t). \tag{3.5}$$

In matrix form, the TDSE is

$$i\begin{pmatrix} \dot{C}_{2p} \\ \\ C_{2s} \end{pmatrix} = \begin{pmatrix} 0 & \Omega(t)\cos(\omega t)e^{-i\omega_0 t} \\ \\ \Omega(t)\cos(\omega t)e^{i\omega_0 t} & 0 \end{pmatrix} \cdot \begin{pmatrix} C_{2p} \\ \\ C_{2s} \end{pmatrix}, \tag{3.6}$$

where $\Omega(t)$ is the time-dependent Rabi frequency

$$\Omega(t) = \mu f(t), \tag{3.7}$$

and ω_0 is the energy difference between 2p and 2s state $\omega_0 = \omega_{2p} - \omega_{2s}$. We have approximated the XUV pulse as a delta function, so the initial condition is that the 2p state is populated

$$C_{2p}(0) = 1, \quad C_{2s}(0) = 0. \tag{3.8}$$

Using perturbation theory [50], the amplitude of the two states can be written as:
Zeroth order:

$$C_{2p}^{(0)}(t) = 1, \qquad C_{2s}^{(0)}(t) = 0. \tag{3.9}$$

First order:

$$C_{2p}^{(1)}(t) = 1, \qquad C_{2s}^{(1)}(t) = -i \int_0^t \Omega(t') \cos(\omega t') e^{i\omega_0 t'} dt'. \tag{3.10}$$

Second order:

$$C_{2p}^{(2)}(t) = 1 - \int_0^t dt' \, \Omega(t') \cos(\omega t') e^{-i\omega_0 t'} \int_0^{t'} dt'' \, \Omega(t'') \cos(\omega t'') e^{i\omega_0 t''}, \tag{3.11a}$$

$$C_{2s}^{(2)}(t) = -i \int_0^t \Omega(t') \cos(\omega t') e^{i\omega_0 t'} dt'. \tag{3.11b}$$

We can also go to higher orders, but second order perturbation theory is usually enough for capturing the main dynamics in our 2p-2s system, as will be shown below.

After the derivation of the two state amplitude in perturbation theory, we can then use $C_{2p}^{(2)}(t)$ to calculate the response function. The procedure for calculating the response function is the same as in the previous chapters (see Eq. (2.8)). Fig 3.2 shows the absorption spectrum calculated by perturbation theory compared to the two-level TDSE. In these calculations, the IR pulse has a FWHM of 15 fs, an intensity of 3×10^{12} W/cm^2 and a wavelength of 800nm, which couples the helium $2p-2s$ states with energy difference of 0.49 eV. With these parameters, the peak Rabi frequency is $\Omega_0 = 0.7$ eV, and the detuning is 1.06 eV. We can see the absorption calculated from perturbation theory looks almost identical to that of the two-level TDSE. And the LIS feature near the 22.2 eV in the full calculation in Fig. 3.1 is well reproduced in both results.

From the excellent agreement of Fig. 3.2(a) and (b), we can see that when large detuning is satisfied, perturbation theory works well, even under strong coupling conditions that the Rabi frequency is comparable to the resonant frequency $\Omega_0 \sim \omega$. The RWA, on the other hand, will break down in this regime. This is because the RWA assumes the counter-rotating term has no contribution. In the detuned regime, this is not satisfied because the counter-rotating term dominants the dynamics. And this counter-rotating term is contained in the second order perturbation theory.

The excellent agreement of the perturbation calculation suggests a strong promise of using perturbation as a framework to study transient absorption. In many cases, for example the continuous wave and the Gaussian pulse, the integrations in Eq. 3.11a and Eq. 3.11b can be carried out analytically. In those cases, the analytical form of the population and response function may provide clear pictures for the different features in the transient absorption that are difficult to understand

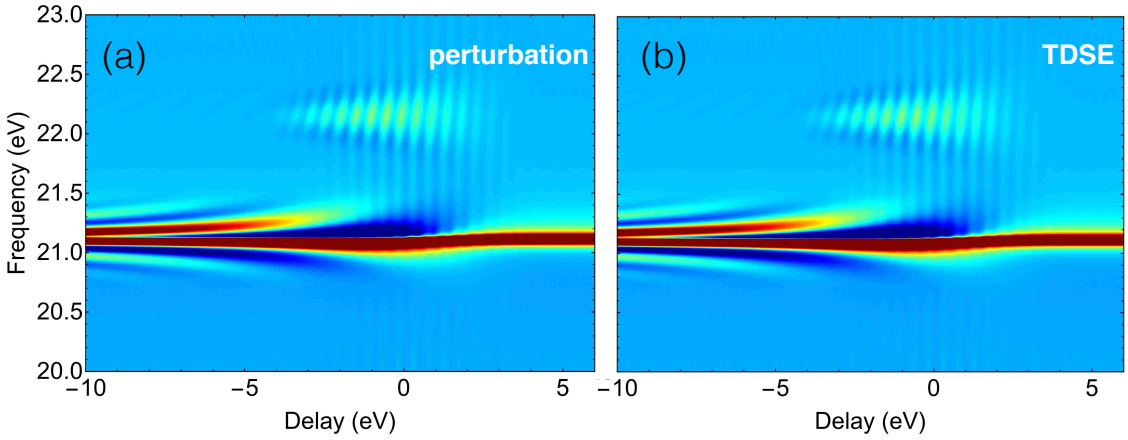

Figure 3.2: Transient absorption spectra calculated from second order perturbation theory (b) compared to that from two-level TDSE (b). We see the perturbation calculation reproduces most of the TDSE results.

otherwise. Moreover, these analytical expressions may be used as a tool to extract information from the transient absorption spectrum, such as dipole coupling strength of the bright and dark state, the IR pulse shape, etc.

3.2 Transient population and final population

When the natural frequency of a system is largely detuned from that of the external driving force, the system in general responds at the driving frequency. A familiar example is the classical harmonic oscillator. When driven off-resonantly, the harmonic oscillator responses at the driving force frequency. Similarly, if an atomic transition is driven off-resonantly, the responds of the atom also mainly happens at the driving frequency. One signature of this off-resonant driving is the transient population transfer, where population is cycling between coupled atomic states repeatedly each half laser cycle. This population last transiently only when the laser field is present and goes to zero when the pulse is over. In this section, we will discuss this transient population transfer and show its connection to the final population transfered when the pulse is over. Specifically, we will establish the connection between population as a function of time at a certain fixed delay and the final population as a function of delay when the pulse is over.

As an example, a comparison of these two quantities is shown in Fig. 3.3(a), using the same parameters as those in the previous section. In this figure, the blue curve shows the final 2s population at the end of the pulse as a function of delay and the red curve shows the 2s population evolution as a function of time at a large negative delay (-10 optical cycle, however the number does not matter as long as it's a large negative delay). We can see these two curves agree very well, which means in this case, the population as function of the delay directly traces the evolution of the population as a function of time.

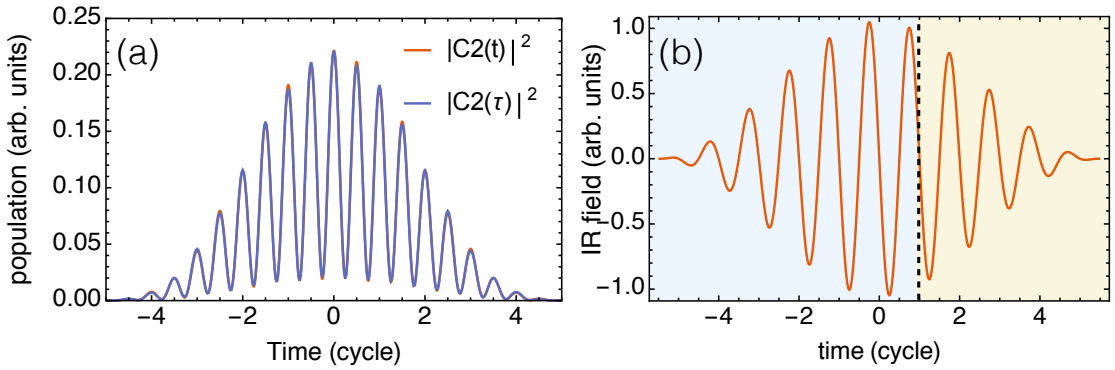

Figure 3.3: (a) compares the population as a function of time and the final population as a function of delay on the dark state. (b) shows the IR pulse. The population at the dark state at a certain time is determined by the part of the IR pulse that prior to that time, but also can be thought of as determined by the part of the IR pulse that after that time, since the net population transfered to the dark state by a complete IR pulse is near zero.

In a simple picture, this agreement can be understood as follows. Shown in Fig. 3.3(b) is the IR pulse. One can then imagine the pulse is separated into two parts at a time t (indicated by the dashed line). Then we can think the population at t is driven by the part of the pulse that precedes t (light blue region). However, we can also think this amount of population is driven by the part of the pulse that arrives after time t (light red region), since the total population should return to zero at the end of the pulse. This agreement can also be seen from the following derivations. Because $\Omega(t)$ is slowly varying, it can be taken out from the integral in Eq. (3.11b),

$$C_2(t) = -i\Omega(t) \int_0^t \cos(\omega t') e^{i\omega_0 t'} dt', \tag{3.12}$$

so that

$$C_2(0, \tau_0) = 0, \tag{3.13}$$

where τ_0 is the end of the IR pulse. This means the final population on the dark state is zero after the pulse ends, as can be expected from Eq. (3.1). Now if the XUV pulse starts at time τ, then the final population at the end of the IR pulse is a function of τ:

$$C_2(\tau, \tau_0) = -i \int_\tau^{\tau_0} \Omega(t') \cos(\omega t') e^{i\omega_0 t'} dt'. \tag{3.14}$$

But according to Eq. 3.13, this can be written as

$$C_2(\tau, \tau_0) = i \int_0^{\tau} \Omega(t') \cos(\omega t') e^{i\omega_0 t'} dt' \tag{3.15}$$

$$= -C_2(0, \tau) \tag{3.16}$$

which means that the final population as function of delay is the same as the population as a function of time except for a negative sign. This direct mapping of the

final population to the population evolution can potentially be used to retrieve the information of the system evolution.

3.3 Summary

In summary, in this section, we showed that perturbation theory is very effective in describing the dynamics in a transient absorption system where the IR pulse is largely detuned. In particular, we showed that the 2s LIS in the full calculation can be well reproduced from a two-level system that involves only the 2p and 2s states. We showed that the 2p-2s two-level system can be well described using second order perturbation theory. The excellent agreement of the perturbation theory with the TDSE potentially opens a new platform on which many of the common transient absorption features can be described analytically. The analytical descriptions of the system may provide a framework to extract the information from the absorption spectrum as well as to formulate physical pictures of the dynamics. Moreover, we have shown that in the large detuning case, the population as a function of time for large negative delay is the same as the final population as a function of delay for the overlap regime. This means that in these cases, the absorption spectrum acts more like a recorder, which records the time evolution of the system directly into a delay dependent absorption spectrum.

Chapter 4
Floquet theory

In the previous chapters, we have described a general picture for transient absorption: The short XUV pulse starts the dynamics by suddenly populating bright states, and then the IR pulse transfers population between these bright states and their dipole allowed darks states. For example, in the near resonant case of helium in Chapter 3, the XUV pulse populates the $2p$ state and the IR pulse cycles the population between $2p$ and $2s$ states through Rabi oscillations. This picture describes a time-dependent process in which the system evolves in the laser-free eigenstates, driven by the laser field. In many quantum systems, time-dependent dynamics can be often described in a time-independent framework by switching to the true eigenstates of the system that take account of the external coupling. In transient absorption, those true eigenstates are the Floquet states. Although calculation in Floquet states are not supreme than that in the bare states, as we will show in this chapter, describing the dynamics in the Floquet states leads to a time-independent picture of transient absorption. In this picture, the strong IR pulse transfers the system into dressed states and the short XUV pulse probes these dressed states. We will show that in this new way of thinking, the light induced states are very intuitive and easy to understand.

4.1 Floquet formalism for a strongly driven two-level system

Floquet theory is best explained using a simple example. In this section we use a strongly driven two-level system as an example to set up the Floquet formalism. The TDSE for a periodically driven two level system is

$$i\left|\dot{\psi}(t)\right\rangle = \hat{H}(t)\left|\psi(t)\right\rangle, \tag{4.1}$$

where $\hat{H}(t)$ satisfies $\hat{H}(t+T) = \hat{H}(t)$ and $T = \frac{2\pi}{\omega}$. In matrix form, the Hamiltonian can be written as

$$\hat{H}(t) = \begin{pmatrix} -\frac{\omega_0}{2} & \Omega_{\mathrm{IR}}(t) \\ \Omega_{\mathrm{IR}}(t) & \frac{\omega_0}{2} \end{pmatrix}, \tag{4.2}$$

and the driving term takes the form

$$\Omega_{IR}(t) = \Omega_0 \cos(\omega t), \tag{4.3}$$

where ω_0 is the energy difference between the two states, ω is the driving frequency, Ω_0 is the Rabi frequency and is a constant here. According to Floquet theory, the wave function can be written in the form [51, 52]

$$\left|\psi(t)\right\rangle = \sum_f c_f e^{-i\epsilon_f t}\left|\phi_f(t)\right\rangle, \tag{4.4}$$

where $|\phi_f(t)\rangle$ satisfy

$$|\phi_f(t+T)\rangle = |\phi_f(t)\rangle\,, \tag{4.5}$$

and are called Floquet states, ϵ_f are the Floquet energies (or quasi-energies) and are time-independent. So solving the TDSE is reduced to finding the Floquet states and the Floquet energies of the periodically driven system. After we have the Floquet states and Floquet energies, the time evolution of the wave function is trivial using Eq. (4.4). Substituting the expansion of the wave function Eq. (4.4) back into the Schrödinger equation Eq. (4.1), we have the equations for the Floquet states:

$$(\hat{H}(t) - i\frac{\partial}{\partial t})\,|\phi_f(t)\rangle = e^{-i\epsilon_f t}\,|\phi_f(t)\rangle\,. \tag{4.6}$$

There are two ways to solve this equation for the Floquet states. The first approach is to directly diagonalize the Floquet matrix in the product basis of the bare states and the photon number states [51, 52]. The other approach is to diagonalize the one period propagator directly in the bare state basis [53]. In the following, we will discuss the first method in detail.

Diagonalize Floquet Hamiltonian

Since the Hamiltonian of the system is periodic, the solution to the Schrödinger equation is determined only by the Hamiltonian in a single period $0 \le t \le T$. The periodicity of the Schrödinger equation can be taken advantages of using a Fourier transform:

$$\hat{H}(t) = \sum_n \hat{H}^{[n]} e^{-in\omega t}, \tag{4.7}$$

$$|\phi(t)\rangle = \sum_n |\phi^{[n]}\rangle\, e^{-in\omega t}, \tag{4.8}$$

where $\hat{H}^{[n]}$ and $|\phi^{[n]}\rangle$ are time-independent coefficients, and determined by

$$\begin{aligned} \hat{H}^{[n]} &= \frac{1}{T}\int_0^T e^{in\omega t}\hat{H}(t)dt, \\ |\phi^{[n]}\rangle &= \frac{1}{T}\int_0^T e^{in\omega t}\,|\phi(t)\rangle\,dt. \end{aligned} \tag{4.9}$$

Since the Fourier space is complete

$$\delta_{mn} = \frac{1}{T}\int_0^T e^{-in\omega t}e^{im\omega t}dt, \tag{4.10}$$

the Fourier transform of a general function $f(t)$ can be thought of as an expansion in a orthogonal basis

$$|n\rangle = e^{-in\omega t} \tag{4.11}$$

$$\langle n|f(t)\rangle = \frac{1}{T}\int_0^T e^{in\omega t}f(t)dt. \tag{4.12}$$

This Fourier basis is different from the ordinary basis in the sense that the basis contains time t as a parameter, and time now has a equal footing as position in the system. As we will explain below, the Fourier states can be thought of as the photon number states. Then the above Fourier transforms of $\hat{H}(t)$ and $|\phi(t)\rangle$ in Eq. (4.9) are the results of projecting onto this orthogonal basis:

$$\hat{H}^{[n]} = \langle n|\hat{H}(t)\rangle\,, \tag{4.13}$$

$$|\phi^{[n]}\rangle = \langle n|\phi(t)\rangle\,, \tag{4.14}$$

with the inversed process being:

$$\hat{H}(t) = \sum_n \langle n|\hat{H}(t)\rangle\,|n\rangle\,, \tag{4.15}$$

$$|\phi(t)\rangle = \sum_n \langle n|\phi(t)\rangle\,|n\rangle\,. \tag{4.16}$$

We can further construct a basis that is the direct product basis of the bare state $|\alpha\rangle = \{|1\rangle\,, |2\rangle\}$ and the Fourier basis $|n\rangle$:

$$|\alpha, n\rangle = |\alpha\rangle \otimes |n\rangle \tag{4.17}$$

and express Eq. (4.6) in this new basis. Then we have

$$\sum_\beta \sum_m \langle \alpha, n|\,\hat{H}_F\,|\beta, m\rangle\,\langle \beta, m|\phi_{\gamma l}\rangle = q_{\gamma l}\,\langle \alpha, n|\phi_{\gamma l}\rangle\,, \tag{4.18}$$

where $|\phi_{\gamma l}\rangle$ is the time-independent Floquet state and $q_{\gamma l}$ is its energy, $\hat{H}_F$ is the Floquet Hamiltonian

$$\hat{H}_F = \hat{H}(t) - i\frac{\partial}{\partial t}, \tag{4.19}$$

and it is the related to the Fourier transform of the Hamiltonian by

$$\langle \alpha, n|\,\hat{H}_F\,|\beta, m\rangle = \hat{H}^{[n-m]}_{\alpha\beta} + n\omega\delta_{\alpha\beta}\delta_{nm}. \tag{4.20}$$

The time-independent Floquet state $|\phi_{\gamma l}\rangle$ and the time-dependent Floquet state $|\phi(t)\rangle$ describes the same state in two different basis, with the former one being in the product basis $|\alpha, n\rangle$ while the latter one being in the bare state basis $|\alpha\rangle$. Since our two-level Hamiltonian in Eq. (4.2) only has three non-zero terms in its Fourier transform

$$\hat{H}^{[0]} = \begin{pmatrix} -\frac{\omega_0}{2} & 0 \\ 0 & \frac{\omega_0}{2} \end{pmatrix}, \hat{H}^{[+1]} = \begin{pmatrix} 0 & \frac{\Omega_0}{2} \\ \frac{\Omega_0}{2} & 0 \end{pmatrix}, \hat{H}^{[-1]} = \begin{pmatrix} 0 & \frac{\Omega_0}{2} \\ \frac{\Omega_0}{2} & 0 \end{pmatrix}, \tag{4.21}$$

the Floquet matrix $\hat{H}_F$ is a block tridiagonal matrix in the product basis, with $\hat{H}^{[0]}$ in its diagonal bands and $\hat{H}^{[\pm 1]}$ in its super-diagonal and sub-diagonal bands, respectively, as shown in Fig 4.1. From this Floquet matrix, we can see that the coupling between different states only takes place between the nearest neighbors in

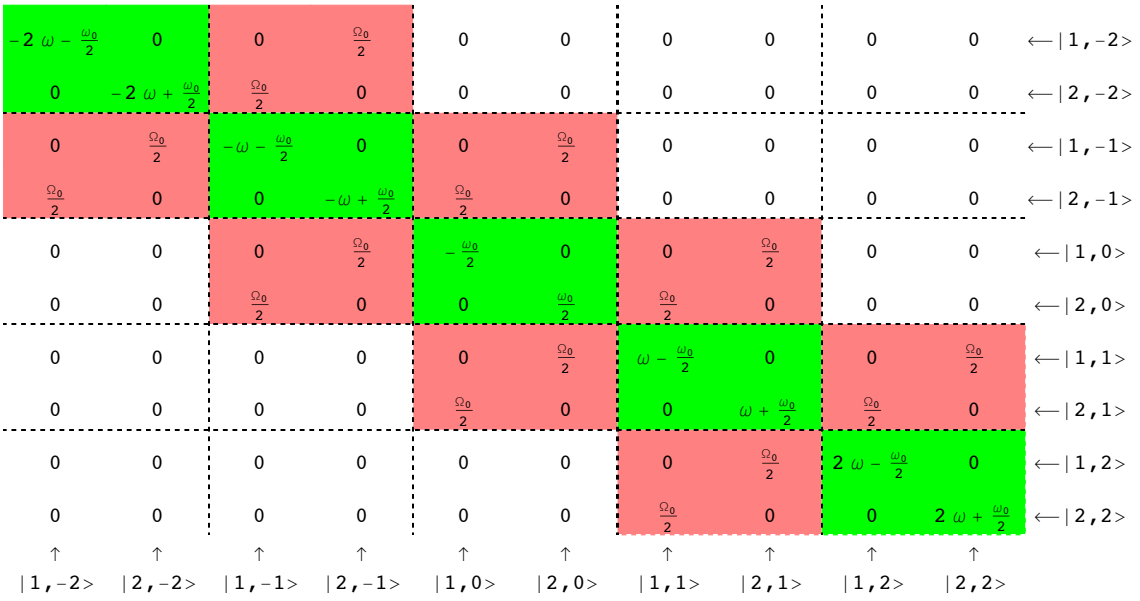

Figure 4.1: Floquet matrix $\hat{H}_F$ with the diagonal blocks is in green indicating the energy of the product states, and off-diagonal blocks in red indicating the coupling between different product states.

this new basis. For example, state $|1,0\rangle$ is only coupled to state $|2,1\rangle$ and $|2,-1\rangle$; state $|2,0\rangle$ is only coupled to state $|1,1\rangle$ and $|1,-1\rangle$. Diagonalizing the Floquet matrix yields the Floquet states and Floquet energies, which we can use to write down the wave function at any time (Eq. (4.4)).

Summarizing the above formalism, the procedure for solving a strongly driven two-level system using Floquet formalism are:

(1) Calculate the Floquet matrix from the Fourier transform of the time-dependent Hamiltonian using Eq. (4.20)

(2) Diagonalize the Floquet matrix and get the Floquet states and Floquet energies in the product basis $|\alpha, n\rangle$.

(3) After obtaining the Floquet states, the evolution of the system is simply the changing of phases of the Floquet states as in Eq. (4.4).

It's worthwhile to note that the Floquet formalism discussed above gives the exact solutions to the time evolution problem, without any approximations. However, approximations are made when we truncate the Floquet matrix to some finite dimensions, in order to diagonalize it numerically. Also, no Hamiltonian is truly periodic, since the field must always be turned on and off.

Calculate absorption spectrum using Floquet theory

After setting up the Floquet formalism for a two-level system, we can now calculate the transient absorption spectrum using this formalism. As in the previous chapter,

we will use a two-level system to model the transient absorption where the XUV pulse is treated as a delta function. Note that the Floquet formalism we set up above only works for a strictly periodic driving field, so the Floquet calculation is aimed to model a square IR pulse case, where the IR pulse starts and ends abruptly. In order to model the case of an actual IR pulse, we would need adiabatic Floquet theory [54], which is outside of the scope of this thesis.

Since the IR pulse is a square pulse, the delay dependence of the IR pulse with respect to the XUV pulse is reflected only in the phase of the IR field when the XUV pulse arrives, and the Hamiltonian is now delay-dependent through the phase of the IR pulse:

$$H(t,\tau) = \begin{pmatrix} -\frac{\omega_0}{2} & \Omega_0 \cos(\omega t + \phi(\tau)) \\ \Omega_0 \cos(\omega t + \phi(\tau)) & \frac{\omega_0}{2} \end{pmatrix}, \tag{4.22}$$

where $\phi(\tau) = \omega\tau$. Fig 4.2 (a) shows the transient absorption spectrum calculated using the Floquet formalism we discussed above for the 2s-2p coupling. The IR pulse is a square pulse with a wavelength of 800 nm, an intensity of 3×10^{12} W/cm^2 and a full duration of 11 cycles. Fig 4.2 (b) shows the spectrum with the same parameters calculated using the traditional approach where the TDSE is solved in the bare states. We can see the Floquet calculation gives an almost identical result as that from the TDSE calculation.

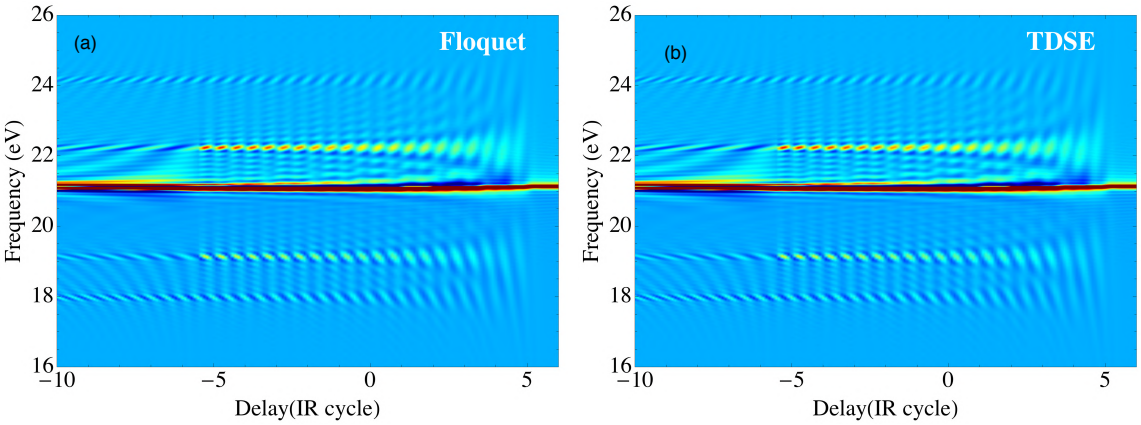

Figure 4.2: Floquet compared with TDSE in calculating the response function in a two-level system. The driving laser is a 11 cycle square IR pulse with a wavelength of 800 nm and an intensity of 3×10^{12} W/cm^2.

4.2 Floquet picture

As we have discussed in the previous section, the Floquet formalism can reproduce the absorption spectrum very well. However, this simple Floquet formalism is limited to only the square IR pulse cases, which seems to prevent it to be useful in calculating transient absorption spectra that can be compared with experiments. In

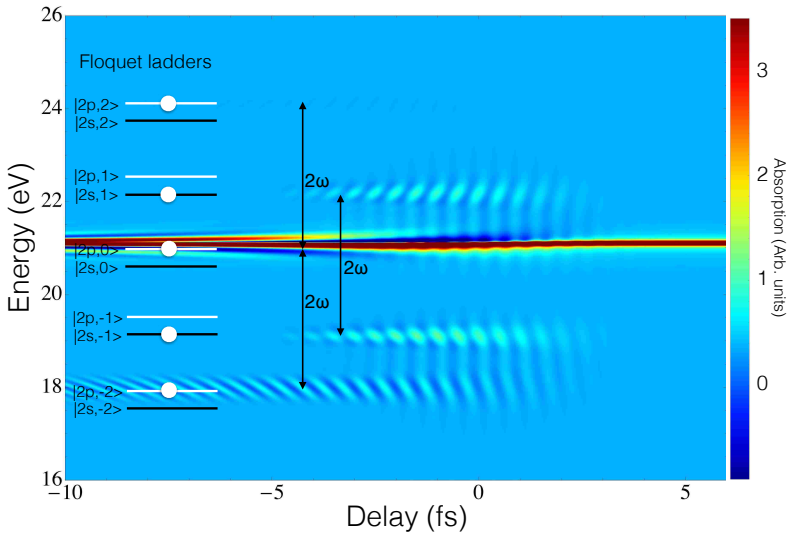

Figure 4.3: Calculated single atom response for the three level helium atom. On the left are shown the positions of the dressed states $|\alpha, n\rangle$ where α is either $2s$ or $2p$ depending on the state in zero field. The white dots show states that have a non-zero transition moment to the $1s$ ground state.

fact, the Floquet formalism is more useful in explaining the features in the absorption spectrum rather than serving as a calculation method. In this section, we will use the Floquet formalism to explain features of a three-level transient absorption spectrum, many of which are very common in transient absorption spectra in a variety of different systems. Moreover, we will show that the Floquet description leads to a new, intuitive picture of transient absorption.

We first simplify the helium atom to a three state system consisting of the ground $1s$ state and the $2s$ and $2p$ excited states. The energies and dipole couplings are the same as in the SAE full calculation in Fig. 1.2. We use the same laser parameters as in the full calculation, except that we move the central wavelength of the XUV to the $1s - 2p$ energy. The result of a full solution of the TDSE for the three state model is shown in Fig. 4.3. The absorption features appear near the $2p$ energy and also at energies that are approximately one IR photon away from the $2s$ state and approximately two photons away from the $2p$ state. There are also visible half cycle oscillations in these features. We now discuss how these features can be explained in terms of Floquet states.

In the three level model, the Floquet states that describe the excited dressed states are built from products of the $2p$, $2s$ states with an integer number of photons. Diagonalizing the two state plus IR field Floquet Hamiltonian (Eq. (4.18)) yields time-independent states which we label as $|\phi_{\alpha,n}\rangle$, where the α label refers to the state in zero field and is either $2s$ or $2p$ in our model, and n is the index for photon numbers involved. We obtain a "ladder" of states for each α with energies $\epsilon_\alpha + n\omega$. These energies are shown on the left hand side of Fig. 4.3. The states are constructed assuming that the IR field has a maximum at $t = 0$. We can use these basis states to

construct time-dependent Floquet states $|\Psi_\alpha(t,\tau)\rangle$ that are dressed states excited at $t = 0$ with an XUV-IR phase delay $\omega\tau$:

$$|\Psi_\alpha(t,\tau)\rangle = e^{-i\epsilon_\alpha t}\sum_n e^{-in\omega(t+\tau)}|\phi_{\alpha,n}\rangle. \tag{4.23}$$

If we ignore the XUV pulse duration, then the initial excited state wave function is a superposition of the Floquet states at $t = 0$:

$$|\Psi(t=0,\tau)\rangle = \sum_\alpha C_\alpha^\tau\,|\Psi_\alpha(t=0,\tau)\rangle, \tag{4.24}$$

where C_α^τ is the dipole transition element from the ground state to the different Floquet states,

$$\begin{aligned} C_\alpha^\tau &= \langle\Psi_\alpha(t=0,\tau)|\hat{\mu}_X|\psi_0\rangle \\ &= \sum_n e^{in\omega\tau}\langle\phi_{\alpha,n}|\hat{\mu}_X|\psi_0\rangle, \end{aligned} \tag{4.25}$$

and $\hat{\mu}_X$ is the dipole operator of the XUV field. Once we have decomposed the excited state wave function at $t = 0$ into dressed states, we can write it at any time $t > 0$ using Eq. (4.23):

$$|\Psi(t,\tau)\rangle = \sum_\alpha C_\alpha^\tau\,|\Psi_\alpha(t,\tau)\rangle. \tag{4.26}$$

Then the time-dependent dipole can be constructed using this expression

$$d(t,\tau) = \sum_{\alpha,m,n} e^{-i(\epsilon_\alpha+m\omega-E_0)t}e^{i(n-m)\omega\tau}\langle\phi_{\alpha,n}|\hat{\mu}_X|\psi_0\rangle\langle\psi_0|\hat{\mu}_X|\phi_{\alpha,m}\rangle + \text{c.c.}, \tag{4.27}$$

where E_0 is the ground state energy.

Using this expression, we can explain many general features in the delay dependent absorption spectrum. The dipole moment oscillates at frequencies $\epsilon_\alpha + m\omega - E_0$, which means there is absorption at those frequencies if they are present in the XUV spectrum. The absorption is also modulated as a function of delay at frequency $(n-m)\omega\tau$. Due to the parity conservation, the XUV pulse can only populate every other state in each Floquet ladder, and in Fig. 4.3 we have put a white dot on the states in each ladder that have a non-zero transition moment to the ground state. Since $m - n$ must therefore be an even number we expect to see oscillations in the absorption with a period of $T_0/2$, $T_0/4$, etc., with the half cycle (2ω) oscillations being the strongest.

The light-induced states we have referred to as $2s^{\pm1}$ are simply the $|2s,\pm1\rangle$ dressed states. They appear close to the $E_{2s} \pm \omega$ energy due to the detuning of the $2s - 2p$ energy difference from ω. The light-induced oscillations in $d(t)$ obviously last only until the IR field ends. This explains why these features are broadened at positive delays. We note that absorption at the $|2p,-2\rangle$ energy can be seen for

negative delays where the XUV and IR pulses do not overlap. In this case the dressed state is populated by the turn on of the IR pulse when $2p$ population is redistributed over the $2p$ dressed states.

In summary, the Floquet formalism gives us a new picture of transient absorption process. In this new picture, the XUV can be thought of probing the IR dressed states — the Floquet states of the atom. In this picture, the presence of the laser field upgrades the bare atomic state Hilbert space by another dimension and lifts the degeneracy of the bare states there. This extra dimension can be thought as the photon number space. This new basis is the product basis of the bare states and the photon number states. Moreover, in the new basis, one can diagonalize the atom-laser Hamiltonian and get the Floquet states as its eigenstates. Then the time evolution can be carried out in the Floquet states. Since the Floquet states are the eigenstates of the Hamiltonian, time evolution will only attach phases to the Floquet states components. After the time propagation, one can go back to the bare states simply by summing over all the photon number states in the product basis. What's more, as we will discuss in regards to the dynamics in solids in the second part of this thesis, the electron dynamics in solids is very similar to that of in a periodic driven system here, since the Hamiltonians are periodic in both cases. Actually, as we will discuss more in detail there, the Bloch theorem, which is one of most important fundamental principles for solids, is essentially the Floquet theorem expressed in space.

Part II
High Harmonic Generation in Solids

Chapter 5

Introduction to high harmonic generation in solids

Since high harmonic generation (HHG) in inert gases was first discovered in 1987 [4], it has become one of the most active research areas in ultrafast atomic physics. With about three decades of development, HHG has become a fundamental tool for modern laser technologies in creating tunable short pulses [1, 9, 55, 56]. It has been used widely in studying ultrafast dynamics in atoms and molecules, and in biological molecular imaging and structure identification [9, 57–59]. A high harmonic spectrum generated by an inert gas usually exhibits a general structure as shown in Fig. 5.1(a). After the initial rapid decline in harmonic intensity, the harmonics form a plateau where a series of harmonics have the same intensity. This plateau ends abruptly with a cutoff at energy $E_{\max} = I_p + 3.17U_p$ [6], where I_p is the ionization potential and U_p is the ponderomotive energy, which is the quiver energy of an electron in an oscillating laser field and is proportional to the laser intensity and wavelength squared. This general structure of the harmonic spectrum can be explained by a three step model [6, 7], as illustrated in Fig. 5.1(b). In the first step, the laser field distorts the atomic potential so that the electron is tunnel ionized from the atom. In the second step, this tunneled electron accelerates in the oscillating laser field and gains kinetic energy. In the third step, if this electron recombines with the ion core, the electron energy is converted to the emission of a high energy photon. In atomic systems, which have inversion symmetry, three steps happen periodically every half-cycle of the laser field, which accounts for the absence of the even harmonics in the spectrum.

However, since the whole high harmonic generation process is highly nonlinear, the intensity of the output high harmonics is typically $5 - 10$ orders of magnitude lower than the fundamental field intensity [61]. This poor conversion efficiency is still one of the unresolved problems that prevents HHG from being used as a high energy photon source outside the labs. From the single atom perspective, the efficiency for generating extreme ultraviolet (XUV) pulses is less than 1 in a billion. Although later on there were phase matching techniques discovered to increase the efficiency, the overall output is still orders of magnitude lower than the input light [62–66]. Recently, Ghimire *et al.* discovered that high order harmonics can also be generated from a bulk crystal [67], which has opened new possibilities to solve this efficiency problem [68]. The higher density in a solid compared to a gas means that more atoms are emitting high harmonics. More importantly, we may be able to engineer the structure of the solids on the micro-meter scale, and design periodic structures that satisfy the phase matching condition, which may greatly enhance the conversion efficiency.

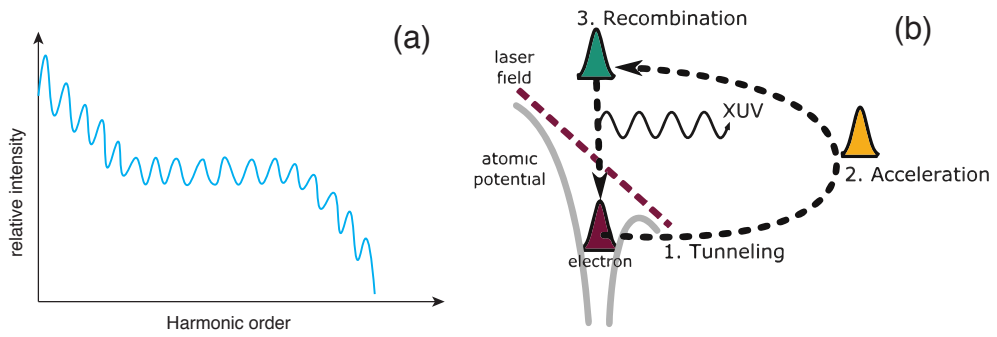

Figure 5.1: Three-step model for HHG in gas. In the first step, the electron is tunnel ionized from the atom. In the second step, the electron gains energy from the laser field. In the third step, the electron is recaptured by the core and emits a high energy photon. Adapted from [60] which is released under the Creative Commons Attribution-Share-Alike License 3.0.

5.1 Recent experiments of HHG in solids

In this section, we briefly review the recent experiments of HHG in solids. HHG from solids was actually reported about two decades ago, first in the metal surface interaction with strong laser field [69]. Researcher noticed that when shining a strong infrared laser on the metal surface, high order harmonics were generated in a surface effect and could be detected in the reflected light. More recently, Ghimire *et al.* reported that high harmonics can also be generated in transmission in zinc oxide crystal [67]. Zinc oxide is a semi-conductor and has a band gap of about 3.2eV and lattice spacing about 2.8 Å. The laser has a wave length of 3.5 μm, which corresponds to a photon energy of 0.38 eV.

Fig 5.2(a) shows the harmonic spectrum at two different laser intensities, as measured in [67]. At the higher intensity, harmonics up to the 25^{th} were observed. Since the inversion symmetry is ensured in the interior of the solid, only the odd harmonics appear in the spectrum. Fig 5.2(b) shows the behavior of the cut-off as a function of intensity. Surprisingly, the cutoff is shown to be linear with the laser field strength, which is different than HHG in gas, where the cutoff is linear in the field intensity. This difference in cut-off behavior suggests that the mechanism for generating harmonics in a solid is different from that in the gas phase.

5.2 Theories of HHG in solids

As discussed above, HHG in solids appears to come from different physics compared to HHG in gas. Currently there is not one common theory that is agreed upon in the community. An early theory, presented by the same team that performed the zinc oxide experiment, proposes that the high harmonics come from electrons moving anharmonically inside the conduction band. The electron motion in this model is treated classically, under the constraint of the anharmonic dispersion relationship

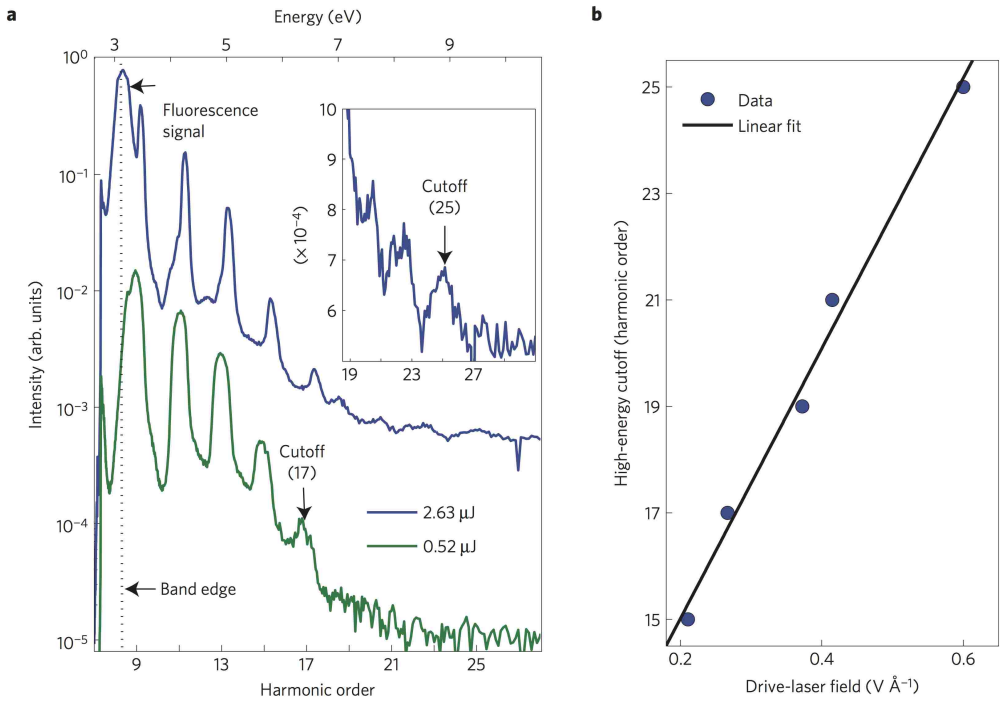

Figure 5.2: (a) HHG spectrum generated from ZnO using two intensities. (b) The high-energy cutoff scales linearly with driven field. reprinted from [67] with permission.

required by the solid. In this model, the group velocity of an electron wave packet is

$$v_g = \frac{\hbar}{m_0^* a_0} \sin\left[\frac{\omega_B}{\omega}\sin(kz - \omega t)\right], \tag{5.1}$$

where $\omega_B = Ea_0/\hbar$ is the Bloch frequency which is proportional to the driving field strength and the lattice constant, ω is the driving frequency of the laser field, and k is the wave vector of the electron. The $\sin\left[\frac{\omega_B}{\omega}\sin(kz - \omega t)\right]$ term in the group velocity expands to the higher frequency components at odd harmonics of the fundamental with an expansion coefficient proportional to the ratio between the Bloch frequency and the driving frequency $\frac{\omega_B}{\omega}$. Thus the cut-off in this theory is determined by $\frac{\omega_B}{\omega}$.

This model explains the linearity of the cut-off, but it does not take account of the inter-band transitions and the cut-off and only qualitatively agrees with the experiment. As collaborators of the Ghimire and Reis' group, we are interested in a theory that go beyond the limitation of intra-band transitions and takes into account both the inter-band and intra-band transitions. And developing a theory that includes both inter-band and intra-band dynamics will be the central goal for the remaining chapters in this part. Besides these two models, there is also a model proposed by Vampa *et. al* that describes the solid using semiconductor Bloch equation [70], and also a model proposed by Higuchi *et. al* that model the solid as a parametric two-level system [71].

In summary, in this introductory chapter, we briefly reviewed the background of HHG in solids and the recent experiments and theories. In the following chapters,

we will progressively establish an understanding of physics of HHG in solids. We will first consider an electron in a solid without the laser field, and show that the allowed energies for the electron form the band structure. We will then consider the case of a solid with a DC field, where we show that the electron performs a periodic motion in space. And finally, we will consider the solid interaction with an AC field, which models the process of HHG in solids.

Chapter 6
Field free band structure

The dispersion relation defines how fast a wave packet spreads out as it propagates in a medium, and it usually can be written as a relationship between the wavenumber of a particular wave component and its corresponding energy. A plane wave in free space has a simple dispersion relation $E(k) = \frac{\hbar^2 k^2}{2m}$ for a given wave number k, mass m and energy E. This means that the energy of a free particle in space increases quadratically as its momentum, and its energy can be any value that is greater than 0. An electron in a solid usually has a complicated form of the dispersion relation and, unlike the free particle, its energy can only have values within a certain regime. These allowed energies form energy bands that are divided by gaps between them. The dispersion relation that contains these bands and gaps is called the band structure of the solid [72–74].

In this chapter, we will review some of the basic concepts for describing an electron in a solid such as Bloch states and Wannier states. These basic concepts provide the foundation of the formalism for our discussion of electron transport in the following chapters. We will also discuss a commonly used numerical method for calculating the band structure from a periodic potential, as well as an analytical method that can be used for a particular class of potentials..

6.1 Band Structure and Bloch States

One of the most important characteristics of a solid is its band structure. In a simple picture, the band structure defines the transport properties of an electron in the solid. In this section, we will show that the band structure can be understood as emerging from the discrete eigenstates of the individual atomic potentials.

The eigenstates of a single, isolated, atomic-like potential usually form a set of discrete states. For example, Fig. 6.1 (a,b) shows the energies and the wave functions of the two bound states of a single atomic potential well

$$V(x) = -1.94 \ \mathrm{sech}^2(0.81x). \tag{6.1}$$

Fig. 6.2(a,c) shows the same with three potential wells, with a separation distance of 10 a.u.. Comparing Fig. 6.1(a) with Fig. 6.2(a) we see that each of the original atomic levels is split into three sub-levels. This splitting can be understood as the removal of the degeneracy of the eigenstates of the individual potential well by the perturbation of the other potentials. As more and more potentials are added, each of the original levels splits into more and more sub-levels. Eventually, these sub-levels are so close to each other that they form a continuous energy band. The band gaps are what remains of the energy regions between the atomic states that have not

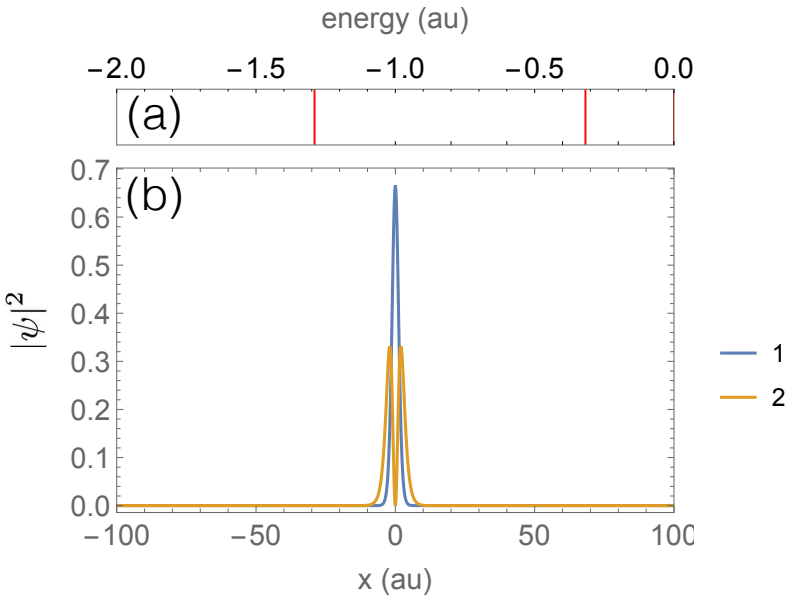

Figure 6.1: Eigenenergies (a) and eigenstates (b) of a single isolated Sech^2 potential. The red lines in (a) indicate the two discrete bound levels, and the curves in (b) represent the two bound state densities.

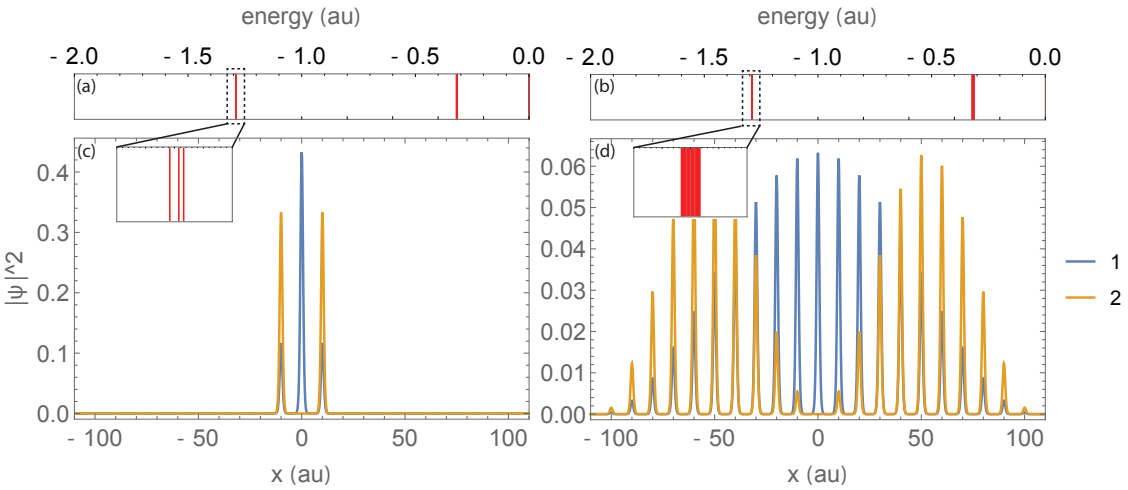

Figure 6.2: Eigenenergies (a) and eigenstates (b) of a potential well with three atomic potential well and (c,d) 200 atomic potential wells. In the three-potential well case, each level is split into three sub-levels. In the 200-potential well case, each level is split into 200 levels, approaching a continuous energy band.

been covered by the sub-levels. At the same time, each of the eigenstates spreads out more and more in space and eventually becomes completely delocalized. These delocalized eigenstates are called Bloch states [72–74]. As an example, Fig. 6.2(b,d) shows the eigenenergies and eigenstates for a potential with 200 wells, where the sub-levels already can't be distinguished at this scale.

After this brief review of the concept of band structure in solids, we will discuss

how to calculate the band structure for a given atomic potential, using two different methods. The first one is a numerical method that diagonalizes the laser free Hamiltonian in the plane wave basis, in which the band structure and the Bloch states are the eigenenergies and eigenstates, respectively. The second one is an analytical method for a special Mathieu-type potential [75]. In this special case, the band structure and Bloch states can be constructed from the tabulated Mathieu functions.

6.1.1 Diagonalizing the Hamiltonian

Since the Bloch states are the eigenstates of the Hamiltonian and the band structure is formed by its eigenvalues, we can diagonalize the Hamiltonian to get the band structure. The equation that governs the eigenstates of the system is the time-independent Schrödinger equation

$$\hat{H}_0 \left|\phi^n\right\rangle = E^n \left|\phi^n\right\rangle . \tag{6.2}$$

where $\hat{H}_0$ is the Hamiltonian

$$\hat{H}_0 = \frac{\hat{p}^2}{2m} + V(\hat{x}), \tag{6.3}$$

$\hat{V}$ is the periodic potential with a period of the lattice constant a_0

$$V(\hat{x} + a_0) = V(\hat{x}). \tag{6.4}$$

$|\phi^n\rangle$ is the nth eigenstate of the Hamiltonian which is the Bloch state. According to Bloch's theorem, the Bloch states can be written as a product of a plane wave and a periodic function [72–74]

$$\phi^n(x) = e^{ikx} u(x), \tag{6.5}$$

where k is called the lattice momentum and $u(x)$ is a periodic function

$$u(x + a_0) = u(x). \tag{6.6}$$

Since the Hamiltonian is periodic in space, we can take advantage of this symmetry by working in momentum space. The basis for momentum space are the plane waves $|K_j\rangle$, where

$$\langle x|K_j\rangle = e^{iK_j x}. \tag{6.7}$$

The wave vectors in this basis are the reciprocal lattice vectors

$$K_j = \frac{2\pi}{a_0} j, \tag{6.8}$$

where $j \in Z$ is an integer. In this basis, the Bloch states can be expanded as [76]

$$\left|\phi^n\right\rangle = e^{ikx} \sum_j C_j^n \left|K_j\right\rangle , \tag{6.9}$$

where k has values in the first Brillouin zone $-\pi/a_0 \leq k \leq \pi/a_0$. Inserting the expansion of $|\phi^n\rangle$ in Eq 6.9 into the Schrödinger equation in Eq. 6.2 and projecting onto a plane wave $|K_i\rangle$, we get the Schrödinger equation in terms of the expansion coefficients

$$\sum_j \left(\frac{\hbar^2}{2m}(k+K_j)^2 \delta_{ij} + V_{K_i - K_j} \right) C_j^n = E^n C_i^n. \tag{6.10}$$

The term $V_{K_i-K_j}$ is the Fourier transform of the periodic potential

$$V_{K_i-K_j} = \langle K_i | \hat{V} | K_j \rangle = \frac{1}{a_0} \int_{-a_0/2}^{a_0/2} V(x) e^{-i(K_i-K_j)x} dx. \tag{6.11}$$

This expansion can also be understood simply as the Fourier transform of the Schrödinger equation, because a continuous periodic function defined in real (x) space can be uniquely mapped onto a set of infinite numbers in momentum (k) space. The mathematical theorem underlines this is the Pontryagin duality [77].

Although in principle we have an infinite number of coefficients coefficients C_j^n, in practice we can truncate and diagonalize the infinite matrix in Eq. 6.10 to get the band structure and Bloch states. Note that this procedure is for calculating the band structure and Bloch states at one specific lattice momentum k only. In order to determine the complete band structure, we have to solve for all possible $k's$ in the first Brillouin zone.

Fig 6.3 shows the band structure calculated using a periodic potential that resembles SiO_2, with the lattice spacing $a_0 = 9.45$ au and lattice potential [76]

$$V(x) \quad = \quad -0.7\,[1+\tanh(x+0.8)]\,[1+\tanh(-x+0.8)]\,, \tag{6.12}$$

with all the quantities in atomic units.

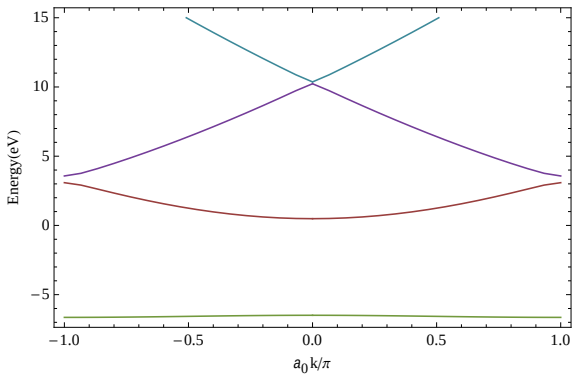

Figure 6.3: Band structure for a one dimensional solid with lattice constant $a_0 = 9.45$ and lattice potential $V(x) = -0.7[1+\tanh(x+0.8)][1+\tanh(-x+0.8)]$. We have used a 51×51 truncated Hamiltonian matrix and 161 k points in the first Brillouin zone in the calculation.

6.1.2 Band structure and Bloch states using Mathieu functions

In the previous section, we briefly reviewed the commonly used numerical method for calculating the band structure from a periodic potential. In this section, we will describe an analytical method that solves the band structure for a Mathieu type potential [75]. This special type of potential is often used as a textbook example because it is the next soluble 1D potential after the Kronig-Penney potential and its limiting case of the Delta function potential [72, 75]. This potential is also used extensively in the optical lattice community, because of its good description of optical lattice potentials [78, 79].

The Mathieu type potential usually has the form [75]

$$V(x) = -V_0 \left(1 + \cos\left(\frac{2\pi x}{a_0}\right)\right), \tag{6.13}$$

where V_0 is the strength of the potential and a_0 is the lattice constant. The time-independent Schrödinger equation we want to solve is

$$-\frac{1}{2}\psi'' - V_0 \left(1 + \cos\left(\frac{2\pi x}{a_0}\right)\right) = E\psi. \tag{6.14}$$

The solutions we want are Bloch states that can be written as

$$\phi(x) = e^{ikx}u(x), \tag{6.15}$$

where $u(x)$ is a periodic function

$$u(x + a_0) = u(x). \tag{6.16}$$

The Schrödinger equation is very similar to the standard Mathieu equation [80]

$$y'' + (a - 2q\cos(2z))y = 0, \tag{6.17}$$

where a and q are two parameters. Note that a is a parameter here and should not be confused with the lattice constant a_0. This Mathieu equation has a general solution

$$y(z) = C_1 \cdot C(a, q, z) + C_2 \cdot S(a, q, z), \tag{6.18}$$

where $C(a, q, z)$ and $S(a, q, z)$ are Mathieu sine (odd) and cosine (even) functions, respectively. The similarities between the Mathieu equation and the Schrödinger equation suggest the possibility of solving the Schrödinger equation by scaling the solution of the Mathieu equation.

Fig. 6.4(a,b) shows Mathieu cosine and sine functions for a series of a-values. The parameter q is set to 1 in both plots. We can see that the Mathieu functions can be both bound (with bluish color) and divergent (with reddish color) for different choices of the parameter a. The bound functions are the stable functions that we will use to construct the solution to Schrödinger's equation. The region in the $a - q$

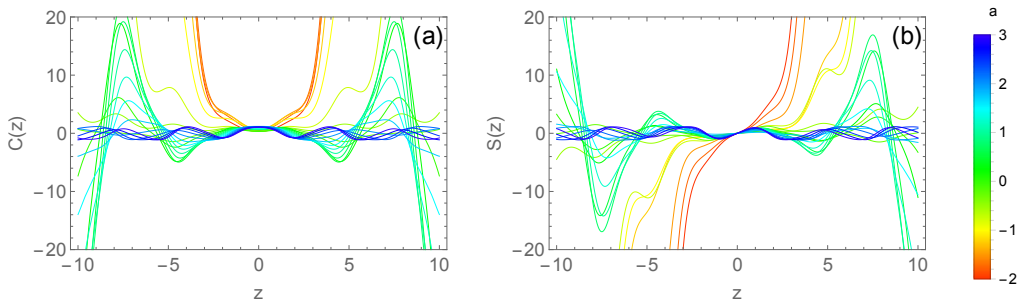

Figure 6.4: Mathieu (a) cosine and (b) sine functions for a set of a values ranging from -2 to 3. The q parameter is 1 in both plots. The Mathieu functions can be bounded or divergent depends on the value of the parameter a. For large positive a, the Mathieu functions are bounded (blue color), whereas for large negative a, the Mathieu functions are divergent (red color).

plane that supports stable Mathieu functions are shown in Fig. 6.5, and is defined as the Mathieu characteristic function [80]

$$a = a(r, q), \tag{6.19}$$

where r is a real number. This means that as long as the parameter a in the standard Mathieu equation in Eq. 6.18 satisfies takes on the allowed values of the characteristic function $a(r, q)$, the solutions of the Mathieu equation are stable. Moreover, these stable solutions can be written in the form

$$y = e^{irz} u(z), \tag{6.20}$$

where u is a periodic function and has $u(z + \pi) = u(z)$.

Comparing the Mathieu equation and the Schrödinger equation Eq. (6.17 ,6.14), and their stable solutions Eq. (6.15, 6.20), we can extract the transformation rules that takes the Schrödinger's equation in Eq. 6.14 and transforms it into the Mathieu equation in Eq. 6.17

$$\begin{aligned} a &\to \frac{2a_0^2(V_0 + \mathcal{E})}{\pi^2} \\ q &\to -\frac{a_0^2 V_0}{\pi^2} \\ z &\to \frac{\pi x}{a_0} \\ r &\to \frac{a_0 k}{\pi}. \end{aligned} \tag{6.21}$$

We can write down the band structure and Bloch states using these transformation rules. Substituting the transformation rules to the condition for stable solution of Mathieu equation in Eq. 6.19, we get the requirement on the relation between the lattice momentum k and the energy E so that stable solutions (the band structure) are supported in the solid, which is exactly the band structure

$$E(k) = -V_0 + \frac{\pi^2}{2a_0^2} \cdot a\left(\frac{a_0 k}{\pi}, -\frac{a_0^2 V_0}{\pi^2}\right). \tag{6.22}$$

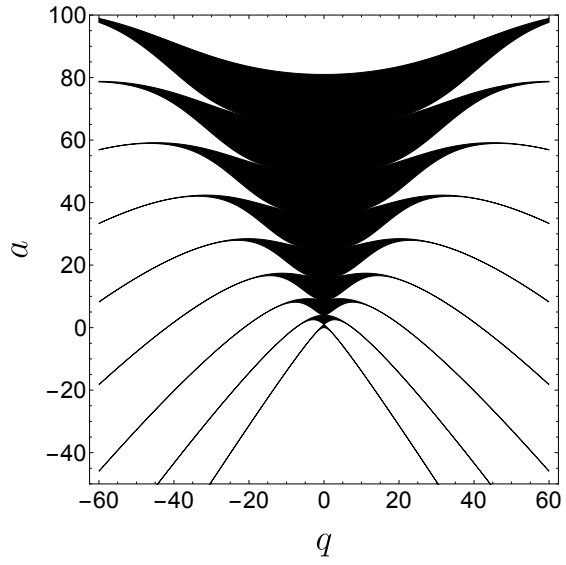

Figure 6.5: The region in the $a - q$ plan that supports stable Mathieu functions is shown in black. Only functions in this region are used in constructing the solution to Schrödinger's equation.

The Bloch states can be constructed from the combination of the even and odd Mathieu functions as [81]

$$\begin{aligned}\phi(x) =& C\left[a\left(\frac{a_0 k}{\pi}, -\frac{a_0^2 V_0}{\pi^2}\right), -\frac{a_0^2 V_0}{\pi^2}, \frac{\pi x}{a_0}\right] \\ &+ i\cdot \text{sign}(k)\cdot S\left[a\left(\frac{a_0 k}{\pi}, -\frac{a_0^2 V_0}{\pi^2}\right), -\frac{a_0^2 V_0}{\pi^2}, \frac{\pi x}{a_0}\right],\end{aligned} \tag{6.23}$$

The periodic part of the Bloch state is simply

$$u(x) = e^{-ikx}\phi(x). \tag{6.24}$$

So now we have both the Bloch states and band structure of our system. Note that the lattice momentum in these expressions is in the extended zone scheme, where k takes the values beyond the first Brillouin zone [72]. To get the band structure and Bloch states in the folded zone scheme, we can simply fold the lattice momentum into the first Brillouin zone by adding or subtracting corresponding reciprocal lattice vectors.

Since we have the analytical expression for the band structure, we can easily gain intuition about how the band structure depends on the potential depth V_0 and the lattice constant a_0. Fig. 6.6 and Fig. 6.7 show the band structure at a variety of parameters. From the varies band structures, we can gain intuition about the solid system:

(1) For large lattice constant and deep potential, the bands tend to flatten out. For example the first and second bands in Fig. 6.6 become flatter as the potential gets deeper. This is expected because in the deep potential case, each

atomic potential well is more isolated, which means that the dynamics are more concentrated in the individual potential well and less in other potential wells. At the limit of large lattice constant where the lattice constant approach infinity, we recover the single atomic case.

(2) For small lattice constant and shallow potential, the bands tend to approach the free electron band structure. For example, the third and fourth bands in Fig. 6.7 become more free-electron like when the lattice constant decreases. This is also expected because small lattice constant and shallow potential makes the wave function spread out into many wells and behave more like that of a free electron.

This intuition suggests that dynamics in solids may not necessarily have a universal simple model for all band structures, as compared to the universal applicability of the Strong Field Approximation [82] to all inert gases. Instead, the dynamics in solids will depend more strongly on the parameter regime of the problem at hand.

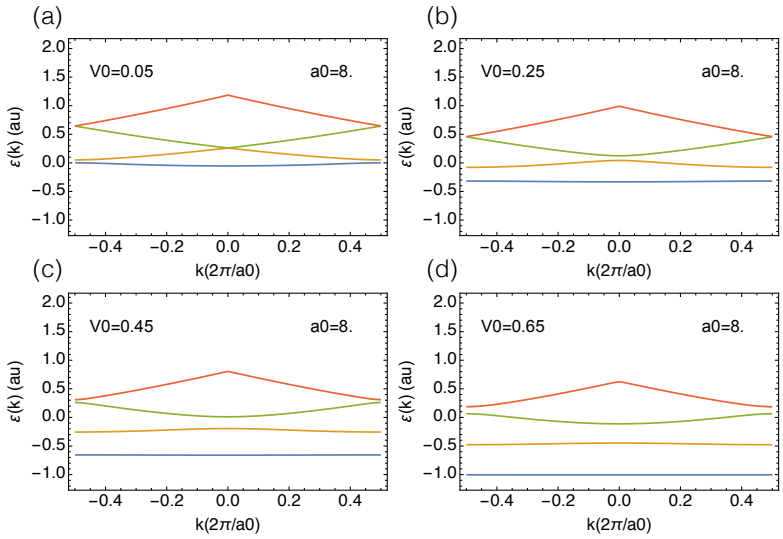

Figure 6.6: Band structure with different potential depth. As the potential depth increases, the first and second bands tend to flatten out and the band gaps gradually increase.

In summary, in this chapter we mainly considered the static problem of an electron in a solid without external forces. We have briefly reviewed the idea of forming band structure from discrete atomic states. We have also discussed a commonly used numerical method in calculating the band structure from a periodic atomic potential. Finally, for a Mathieu-type solid, we have shown an analytical method to calculate the band structure and Bloch states from rescaling of the standard Mathieu equation and its tabulated solutions. In the next chapter, we will discuss the dynamics of a electron in a solid, interacting with of a constant external field.

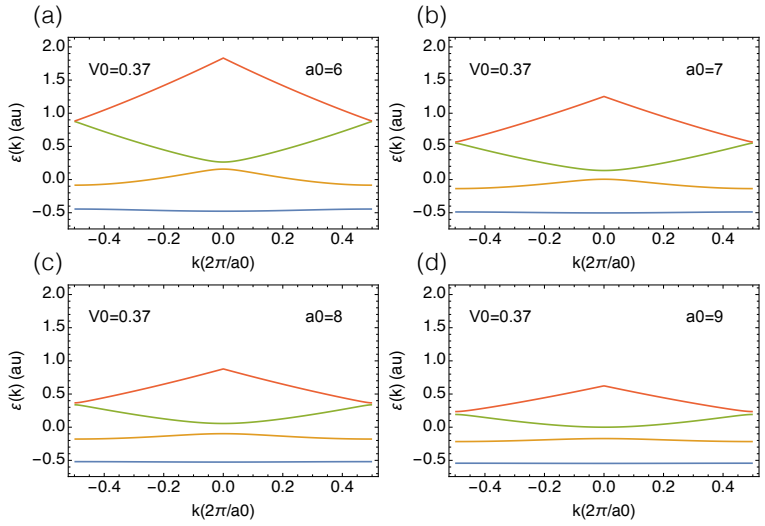

Figure 6.7: Band structure with different lattice constant. As the lattice constant decreases, the third and fourth bands tend to become free-electron like.

Chapter 7
Interaction of a solid with a DC field

7.1 Introduction

In the previous chapter, we have discussed the band structure and Bloch states of a 1D solid without external field. In this chapter, we will go to the next step and discuss the simplest case of a solid with a field – a constant field (DC field). Although this problem looks simple at first sight, adding a DC field introduces rich dynamics to the system, many of which are still being actively investigated in research. These dynamics include Bloch oscillation, Wannier-Stark localization, chaotic scattering, etc [78, 79, 83, 84]. In this chapter, we will first review the Bloch oscillation, and then discuss the Wannier-Stark states and finally discuss the connection between a DC field dressed system to a quantum well system.

7.2 Bloch Oscillation and Zener tunneling

7.2.1 Bloch oscillation

When applying a constant electric field to a free electron, the dynamics are trivial. The electron will constantly accelerate in the direction of the force. However, an electron subject to a constant field in a periodic potential will not accelerate along one direction, but instead will oscillate in space around some fixed point. This is quite counter-intuitive to our daily experience, since if we tilt a carton of eggs with the lid open we will never expect the eggs sometimes going up instead of falling down [85]. This counter-intuitive oscillatory motion is called Bloch oscillations, the oscillation frequency is the Bloch frequency, and the oscillation period is the Bloch period:

$$\omega_B = \frac{ea_0F}{\hbar} \tag{7.1}$$

$$T_B = \frac{2\pi}{\omega_B}, \tag{7.2}$$

where a_0 is the lattice constant and F is the external electric field. As an example, Fig. 7.1 shows snapshots of the wave packet evolution as it performs the Bloch oscillation in real space in a single Bloch period. We can see that initially the wave packet accelerates along the direction of the force, and then it reflects back in space

as if it had hit a wall, and finally it returns to its initial position. The wave packet will perform this oscillation periodically as long as the field is present. Fig. 7.2 shows the total current and the polarization (i.e. the integration of the current) of the electron wave packet, both of which also have a period of T_B.

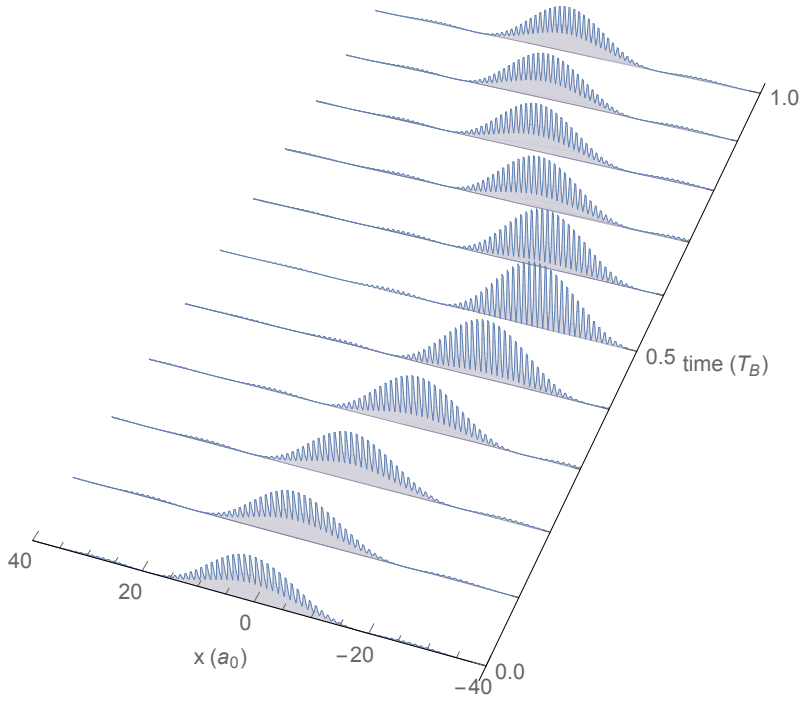

Figure 7.1: Bloch oscillation in real space. The lattice constant is $a_0 = 2\pi$ au, the periodic potential is $V(x) = -0.125(\cos[2\pi x/a_0] + 1)$, and the field strength is $F = 5.5 \times 10^{-4}$ au. The initial wave function spans about 10 lattice sites.

The motion of the electron in a solid with a DC field is governed by the TDSE

$$i\hbar \frac{\partial}{\partial t} |\psi(t)\rangle = (\hat{H}_0 + \hat{H}_{\text{int}}) |\psi(t)\rangle \,, \tag{7.3}$$

where $\hat{H}_0$ is the laser-free Hamiltonian

$$\hat{H}_0 = \frac{\hat{p}^2}{2m} + V(\hat{x}), \tag{7.4}$$

and $V(\hat{x})$ is a periodic function with the period of a lattice constant a_0

$$V(\hat{x} + a_0) = V(\hat{x}). \tag{7.5}$$

$\hat{H}_I$ is the interaction Hamiltonian, which in dipole approximation can be written both in length gauge and velocity gauge:

$$\hat{H}_I^L = e\hat{x}F(t) \tag{7.6}$$

$$\hat{H}_I^V = \frac{e}{m} A(t)\hat{p}. \tag{7.7}$$

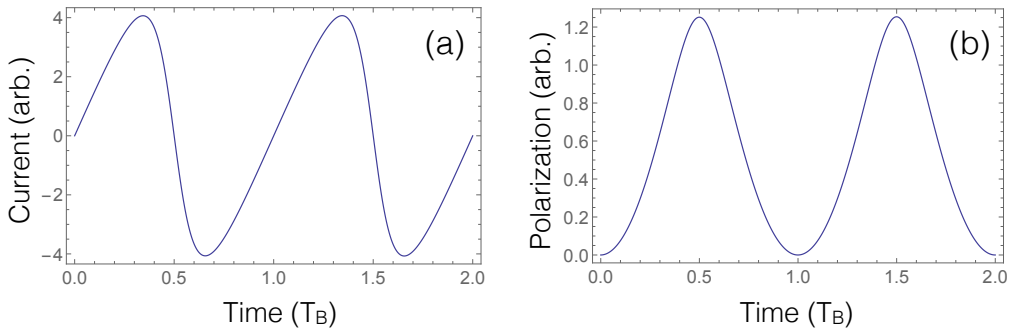

Figure 7.2: Both the (a) total current and (b) polarization of the electron wave packet have a period of T_B.Parameters are the same as in Fig. 7.1.

Starting from here, the Bloch oscillation can be described in either length gauge [86] or velocity gauge [87], corresponding to two physical pictures of the Bloch oscillation. We will discuss the velocity gauge picture in this section and leave the length gauge picture to the next section.

In the velocity gauge, the Bloch oscillation can be expressed in the "semi-classical" approach through the so-called acceleration theorem [88]

$$\hbar\dot{k} = -eF, \tag{7.8}$$

where k is the lattice momentum and F is the DC field. This model describes the response of the electron to the external field, and actually applies to any wave packet with a narrow distribution in k space. Together with the dispersion relationship of the electron

$$E = E(k), \tag{7.9}$$

the group velocity can be written as,

$$v(t) = \frac{1}{\hbar}\frac{\partial E(k)}{\partial k} \tag{7.10}$$

from which the electron motion is completely determined. For example, a free particle with zero initial momentum $k_0 = 0$ has the group velocity and position

$$v(t) = \frac{eFt}{m} \tag{7.11}$$

$$x(t) = \frac{eFt^2}{2m}, \tag{7.12}$$

which is the result we expected.

For an electron in a solid the dispersion $E(k)$ is periodic with $2\pi/a_0$, which means the allowed wave vector is confined in the the range $[-\pi/a_0, \pi/a_0]$. As the wave function reaches the right edge of the Brillouin zone, the electron will Bragg reflect and reappear at the left end of the Brillouin zone. This periodic process happens with a frequency

$$\omega_B = \left(\frac{eF}{\hbar}\right) / \left(\frac{1}{a_0}\right) = \frac{eFa_0}{\hbar}, \tag{7.13}$$

which is the Bloch frequency. For a solid, considering only the nearest neighbor [72], the dispersion relationship can be written as

$$E(k) = -\frac{\Delta}{2}\cos(ka_0), \tag{7.14}$$

where Δ is the band width. The group velocity and the position of the electron are then

$$v(t) = -\frac{\Delta a_0}{2\hbar}\sin(\omega_B t) \tag{7.15}$$

$$x(t) = \frac{\Delta}{2eF}\cos(\omega_B t), \tag{7.16}$$

which exhibits the Bloch oscillation with Bloch frequency ω_B as we expected.

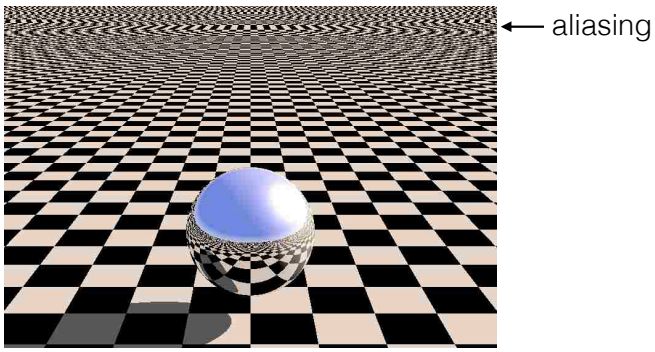

Figure 7.3: The aliasing effect in a digital picture of a large checkerboard. The stripes at the far field comes from the fact that the alternation frequency of the black and white cells exceeds the pixel density of the picture.

Although the acceleration theorem is usually referred to as a semi-classical theory, it can actually be rigorously derived from the TDSE in the velocity gauge, when the transitions to other bands are ignored [88]. We will elaborate more on this point in the following chapters when we discuss the solid in an AC field.

An analogy to Bloch oscillations is the aliasing effect in digital signal processing. An example is the backward rotation of the car wheels in movies. Initially when the speed of the car is slow, we see the wheels rotate forwards as expected. As the speed of the car increases, the wheels appear to rotate backwards. The apparent backward rotation is because that the actual rotation frequency has exceeded the Nyquist frequency [89] of the refresh rate of the movie, making the rotating wheels appear to rotate at a lower, negative frequency. Depending on how much a high frequency exceeds the refresh rate, it may appear as positive or negative low frequencies. This is very similar to the Bloch oscillation in a solid. The lattice momentum at the first Brillouin zone is the highest momentum that can be supported in the solid (refresh rate), and as the electron momentum exceeds the first Brillouin zone (fast forward rotating wheel), it will be identical to a negative momentum in the negative part of

the first Brillouin zone (slow backwards rotating wheel). Similar aliasing effects can be also seen in digital pictures where the change of the pattern exceeds the pixel density of the picture. For instance, in the picture of a infinite large checkerboard shown in Fig. 7.3, we can see stripes in the far background of the checkerboard. This is because the frequencies at which the black and white cells flip on the checkerboard in far field exceeds the pixel density of the image, and thus those fast frequencies appear as low frequency distortions.

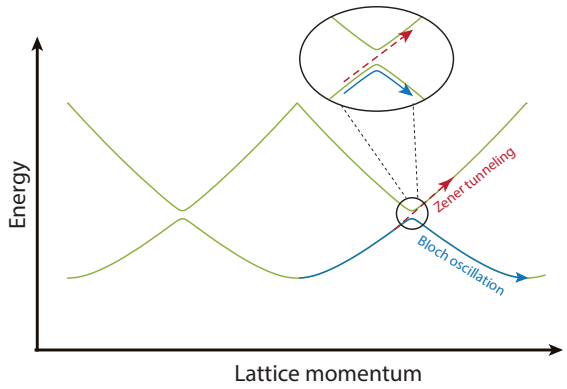

Figure 7.4: Schematic of Bloch oscillations and Zener tunneling. Bloch oscillations are the part of the wave packet that states on the same band while Zener tunneling is performed by the part that tunnels to higher bands.

7.2.2 Zener tunneling

The Bloch oscillation picture applies when tunneling to other bands is small. This condition is usually satisfied for the first band formed by the corresponding deeply bound atomic states, but not necessarily for bands formed by highly excited atomic states. In another perspective, Bloch oscillations dominate the dynamics if the atomic potential is deep and the avoided crossings near the band gaps are smooth. However, for a shallow potential, where the band gaps are small and the avoided crossings are sharp, a large population can leave the original band and tunnel to other bands at the avoid crossings. This tunneling is called Zener tunneling. The tunneling process is shown schematically in Fig. 7.4. The dynamics of the two parts of the wave packet are actually closely related to that of the diabatic and adiabatic transitions at an avoided crossing. The Bloch oscillation describes the part of wave packet that adiabatically follows the field and stays on the band, while the Zener tunneling describes the part of wave packet that diabatically tunnels through the band gap into other bands. We will come back to this point in the following chapters when we discuss a solid in an laser field.

To demonstrate Bloch oscillations in the presence of Zener tunneling, Fig. 7.5 shows the evolution of a wave packet at different potential depths. We start from a free wave packet that spans about 20 lattice sites in Fig. 7.5(a), and gradually

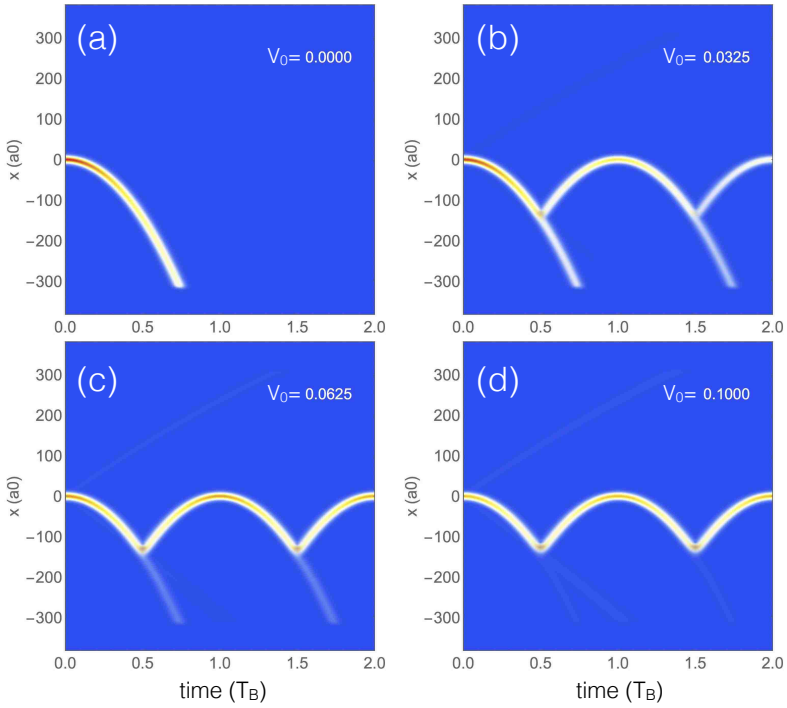

Figure 7.5: Bloch oscillations in a periodic potential with four different potential depths. The numbers indicate the value of V_0. When $V_0 = 0$ the wave packet evolution is the same as that of a free electron. When the potential is non-zero, the wave packet splits into two parts. One part performs Bloch oscillations and the other part continues the free electron behavior, which is the Zener tunneling part. As the potential gets deeper the Zener tunneling part gets smaller.The initial wave packet spans about 20 lattice sites.

increase the depth of the periodic potential in Fig. 7.5(b-d), and then plot the evolution of the wave packet when a constant field is present. When the potential depth is zero in Fig. 7.5(a), the wave packet accelerates along the force direction in space like a free particle. Then as the periodic potential get deeper in Fig. 7.5(b-d), the wave packet splits into two parts. One part stays on the same band and performs a Bloch oscillation, while the other part continues its free particle-like behavior and acts as if the band gap does not exist. This second part is the part of the wave function that tunnels through the band gap into the second band. In Fig. 7.5(b,c,d) the band gap increases as the potential get deeper, so the tunneling portion of the wave function get smaller and smaller.

Bloch oscillation does not happen only on the lowest band, but can happen on multiple bands, if they are populated, either initially or via tunneling. For a Gaussian initial wave packet in space, which is a typical initial condition for cold atoms in optical lattices [90], the dynamics of the wave packet is usually a superposition of Bloch oscillations and Zener tunneling in multiple bands. For example, Fig. 7.6(c) shows the evolution of a Gaussian wave function in space as a function of time. Fig. 7.6(a) shows how the periodic potential is tilted by the external field and

Fig. 7.6 (b) shows the initial distribution of the wave packet in space. In Fig. 7.6(c) we can see the the wave packet evolution is quite complicated. In the following we will break down this complicated process into several simpler ones by restricting the initial population.

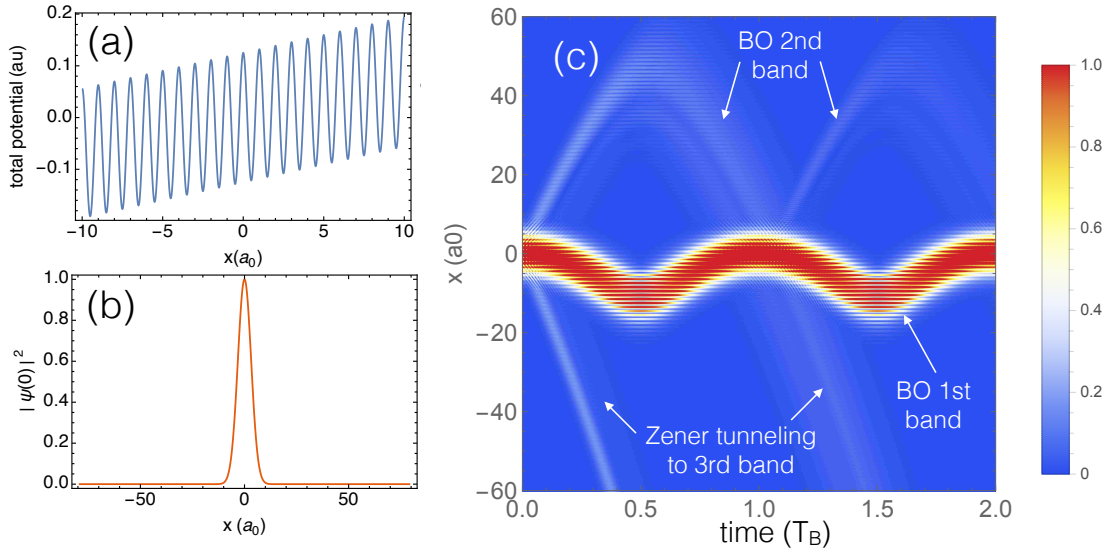

Figure 7.6: (a) shows a the tilted periodic potential by a constant laser field. (b) shows the distribution of the initial wave function in space. (c) shows the evolution of the wave packet in space. Bloch oscillations on the first and second band can be seen. Zener tunneling from the second to the third band is also present. The periodic potential has a lattice constant $a_0 = 6.28$ au and potential depth of $V_0 = 0.125$ au. The constant field has a strength of $F = 1.1 \times 10^{-3}$ au.

We take the initial Gaussian wave packet in Fig. 7.6(c) and project it on to the Bloch states of the first or the second band and reconstruct an initial wave packet that only has components on the first or second band, respectively

$$|\psi_n\rangle = \sum_k \langle \phi_{nk}|\psi\rangle \, |\phi_{nk}\rangle \, . \tag{7.17}$$

The projection removes the component of the other bands from the initial wave packet since Bloch states on different bands are orthogonal

$$\langle \phi_{nk}|\phi_{n'k'}\rangle = \delta_{nn'}\delta_{kk'}. \tag{7.18}$$

Fig. 7.7(a,b) shows the initial Gaussian wave packet and the wave packet reconstructed from the projection onto the first and second band Bloch states, respectively. Using these reconstructed wave packets as the initial condition, we get very clean Bloch oscillation on the first band as shown in Fig. 7.7(c). Since the band gap between the second and the third band is small and the Zener tunneling is large, we still have the tunneling in Fig. 7.7(d). Moreover, since the band gap between the

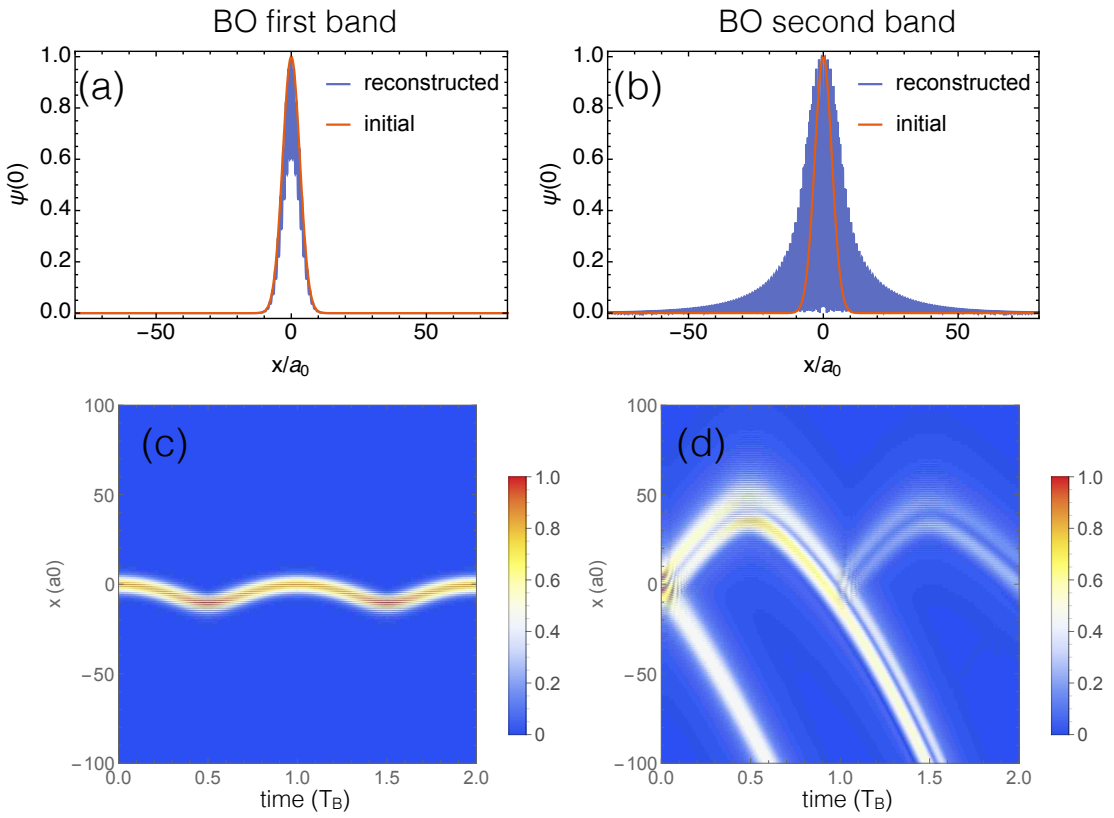

Figure 7.7: Bloch oscillations on the first and second bands. A Gaussian initial wave packet projected on the Bloch states on the (a) first band and (b) second band respectively. The evolution of the projected wave packet is shown in (c) and (d). Parameters are the same as in Fig. 7.6.

second and the third band is at the band center, the Zener tunneling happens at the integer number of Bloch periods as apposed to the half integer periods in Fig. 7.5.

Even when the Zener tunneling is small and can be safely ignored, the dynamics of Bloch oscillations on a single band differs dramatically depending on the initial condition [91]. Well-known special cases are 1) the initial wave packet strongly localized in k space and delocalized in real space, which leads to the oscillation mode or 2) the initial wave packet strongly localized in real space and delocalized in k space, which leads to the breathing mode. In the oscillation mode, the wave packet oscillates in real space, and its group velocity and averaged position both have a period of T_B. All the figures showing Bloch oscillation above are in the oscillation mode. In the breathing mode, however, the wave packet periodically collapses and revives at the Bloch frequency, and the group velocity and the averaged position of the wave packet stay zero for all the times and the system has no net current. These different behaviors are demonstrated in Fig. 7.8 (a-d), where evolution of the wave packet with different initial distributions is shown in real space. In Fig. 7.8(a) the initial wave packet spreads out about 5 lattice sites and it shows the oscillation model, while the initial wave packet in Fig. 7.8(d) spans only 1 lattice site and shows

the breathing mode. In between these two cases are a combination of breathing mode and oscillation mode as shown in Fig. 7.8(c,d). These different initial conditions are very important since the dynamics following them are completely different, so choosing the most appropriate initial condition should be considered carefully before studying the electron dynamics. We will come back to this point when we discuss the electron dynamics in a solid with a laser field in the next chapter.

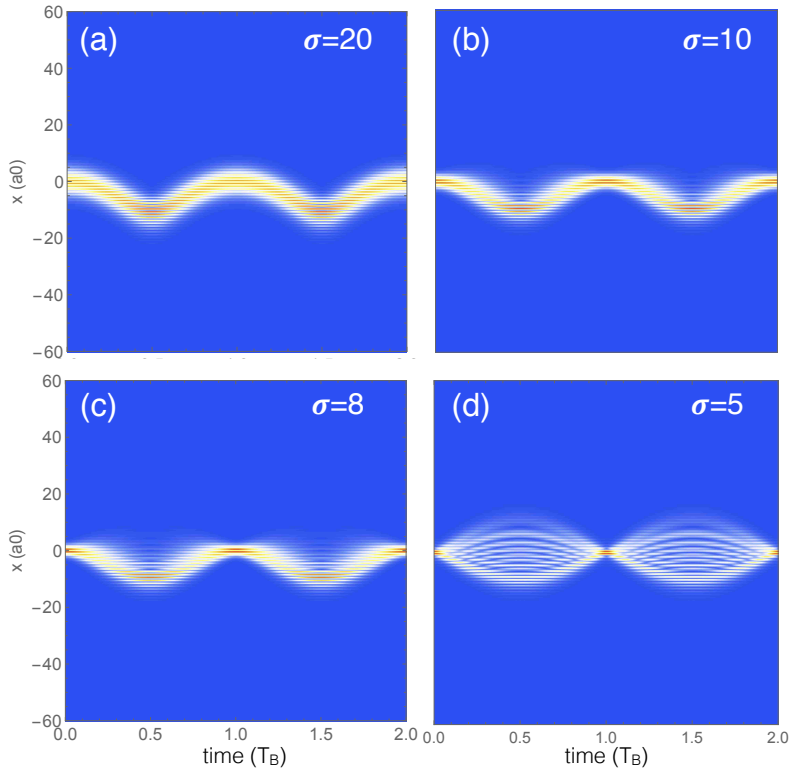

Figure 7.8: The dynamics of the wave packet change from oscillating mode to berating mode as the initial wave packet spanning broader spacial distribution. A Gaussian with standard deviation σ of (a) 20 (b) 10 (c) 8(d) 5 au is used as the initial wave function. The components on other bands are removed using Eq. 7.17. Other parameters are the same as in Fig. 7.6.

7.3 Wannier States

As we have shown in the previous section, an electron in a solid performs Bloch oscillations when subject to an external constant electric field. As the acceleration theorem in Eq. 7.8 suggests, Bloch oscillations can be pictured as a particle traversing the first Brillouin zone periodically along the band in momentum space. This picture corresponds to the velocity gauge description of the Bloch oscillations. However, sometime a length gauge description is more useful to provide a conceptual understanding of the underline physics. For instance, the three-step model [6, 7]

is constructed entirely in the length gauge, in which a clear physical picture is emerged. In this section, we will discuss the length gauge description of the Bloch oscillations using the so called Wannier-Stark states [88, 92]. We will show that the Bloch oscillations in length gauge can be understood simply as quantum beatings.

First of all, unlike the laser-free case where the allowed energies of the system form bands, the DC field changes the energies of the system into a ladder-like structure, known as a Wannier-Stark ladder. Shown in Fig 7.9 are comparisons between the eigenstates of the solid with and without a DC field. The periodic potential for the solid has a period of $a_0 = 10$ au and a potential well of $V(x) = -1.94\,\mathrm{Sech}[0.81x]$ for the single lattice cell.

Fig 7.9(a-b) shows the periodic potential with and without the field. Fig 7.9(c-d) shows the eigenenergies of the system in the two cases. The same information are plotted in Fig 7.9(e-f) in a different way such that each vertical line indicates an allowed eigenenergy of the system. In the laser-free case, some eigenstates have almost degenerate energies and they form bands, as shown in Fig 7.9(e) around -1.3 au and -0.3 au. And in the DC field case, these two bands turn into two sets of ladders. Note that in the potential we include only a few potential wells in order to clearly demonstrate the energy shifts of the eigenenergies, otherwise ladders from different bands will mix together.

The nature of the Wannier-Stark ladders can be seen more clearly from its field dependence. In Fig. 7.10 we plot the eigenenergies of the system at different field strengths. For clarity, only states belonging to the two lowest bands are shown. As the field strength increases, the almost degenerate states belonging to each band start to have "Stark" effect where the degeneracy are removed by the field, forming "Stark" states with constant energy separation. In other words, the ladder structure in the DC field case originates in the Stark effect of the almost degenerated Bloch states. Hence, these ladders are called Wannier-Stark ladders, and their corresponding eigenstates are called Wannier-Stark states. Eventually, when the field is strong enough, the two sets of Wannier-Stark ladders intercept and form avoided crossings, where the diabatic process can happen. This idea is essentially the starting point of papers by Stockman and coworkers [71, 93] in studying the HHG in solid with a short pulse, where they treat the laser field in the adiabatic limit and track down the evolution of the system using the adiabatic states.

The eigenstates of the DC-field-dressed system are also interesting. In the laser-free system, the eigenstates, i.e. the Bloch states, are delocalized as waves across the whole space, while in the DC field case, the eigenstates are localized in space. The left column in Fig. 7.11 shows the first four Bloch states belonging to the lowest band. In order to show the wave behavior, the real part of the Bloch state is plotted. In the second column, we plot the lowest four Wannier-Stark states, which are eigenstates of the DC-field-dressed system. They are very well localized at each lattice site. This process of localization of the eigenstates is essentially a Stark effect and is referred to as Wannier-Stark localization [83, 88]. We will discuss this more in the next section.

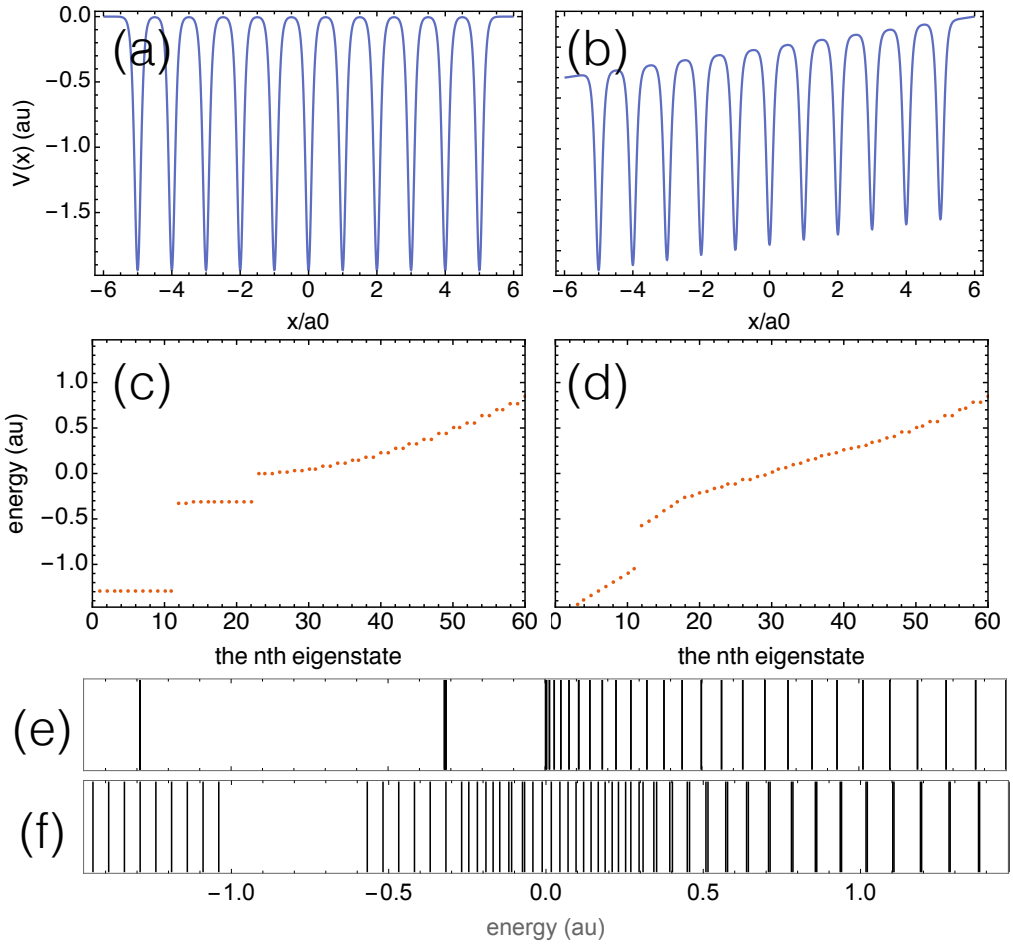

Figure 7.9: (a,b) show the periodic potential without and with the DC field. (c,d) shows the eigenenergies of the system without and with the DC field. (e,f) shows the spectrum of the eigenenergies of the system without and with the DC field.

7.3.1 Analogy to quantum double-well

The behaviors of the Wannier-Stark states can be understood from an analogy to a quantum double-well system. A quantum double well system consists of two wells, and can be thought as a first order approximation to an infinite periodic system.

Consider a quantum double-well with a bias field, the total potential of the system is

$$V(x) = -\text{sech}(x + a_0/2) - \text{sech}(x - a_0/2) + F \cdot x \tag{7.19}$$

where the distance between the well is $a_0 = 15$, and F is the DC field. For the field free case where $F = 0$, the eigenstates are delocalized into two wells, as shown in Fig. 7.12(a). When applying an small non-zero field $F = 0.001$, the eigenstates are localized at each well as shown in Fig. 7.12(b). The two eigenstates have a energy difference of that of their Stark shift energies

$$\Delta E = E_{\text{Stark}}, \tag{7.20}$$

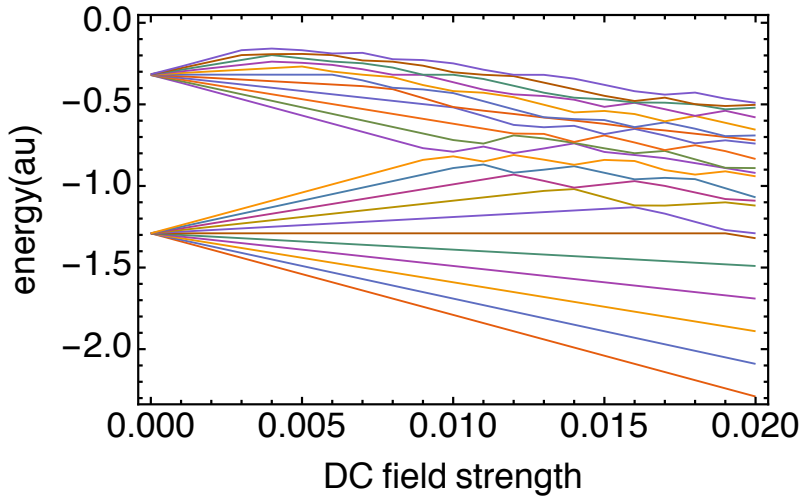

Figure 7.10: The eigenenergies of the system as a function of the field strength. A clear Stark effect can be identified. As the field strength increase, the Stark shifted states belonging to different bands intersect and form avoided-crossings, which are the places where Zener tunneling happens.

since the degeneracy of the eigenstates is lifted by the DC field. This behavior is very similar to the Wannier-Stark localization in solids, where the eigenstates of the system change from delocalized Bloch states to localized Wannier-Stark states after applying a DC field. Fig. 7.12(c) shows the time evolution of one of the field-free eigenstates when a DC field is applied. Since the field-free eigenstate is a superposition of the two field-on eigenstates (Wannier-Stark) states, as a function of time each of the individual field-on eigenstate oscillates at its natural frequency. The two field-on eigenstates have slightly different energies, so that their superposition oscillates at their energy difference, which is the Stark shift energy. If we define the Stark shift energy as a effective Bloch frequency

$$\omega_B = E_{Stark}, \tag{7.21}$$

then the averaged position of the wave packet in space is oscillating at the Bloch frequency, as shown in Fig. 7.12(d).

We can then go further and think of the 1D solid as a quantum multiple-well system, and the Bloch oscillations as the beatings between all the initially populated Stark-shifted states. Since the Stark shift splittings are the same for each eigenstate, their superposition will beat at the Stark shift energy. An example of a eight-well system is shown in Fig. 7.13. In the evolution of the wave packet and the averaged position, we again see the localization of the Wannier-Stark states as well as the Bloch oscillations as the beating in the superposition wave packet. In the above analysis, we have only considered the eigenstates of the quantum well that belong to the same atomic states, and ignored the transitions to other atomic states. For a atomic potential which has more than one bound state, each bound state will form a set of Stark states, similar to those shown in Fig. 7.10. If the Stark states in

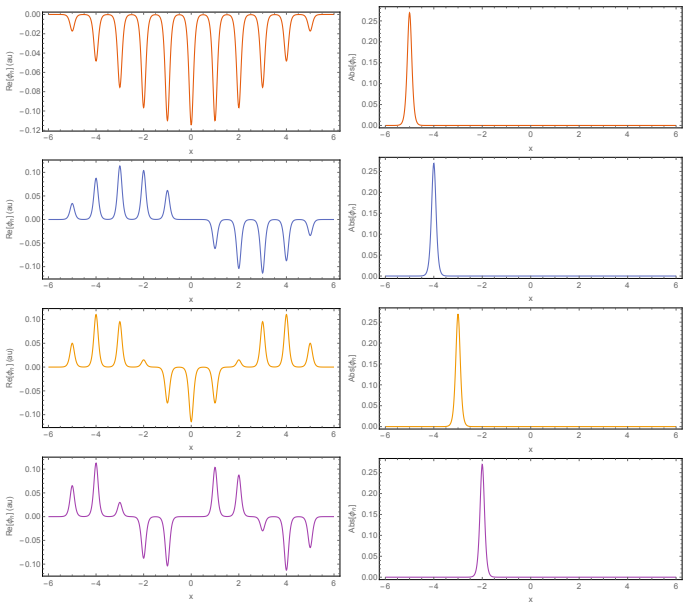

Figure 7.11: The left panel shows the first four Bloch states, which are the eigenstates of the field free system. The right panel shows the first four Wannier-Stark states, which are the eigenstates of the DC field case. The Bloch states are delocalized in space while the Wannier-Stark states are localized at each lattice site.

neighboring sets get close, avoided crossings will form and tunneling will happen. This is an analogy to Zener tunning in solids.

An initially delocalized Bloch state is one of the field-free eigenstates, which is also a superposition of all the free-on eigenstates (Wannier-Stark states). The evolution of a Bloch state in the field is then the quantum beating of all the Wannier-Stark states that are initially populated. In this sense, Bloch oscillations in the periodic potential can be understood as the quantum beatings of a superposition of the Wannier-Stark states.

In summary, in this chapter, we have discussed the motion of an electron in a solid with a constant field. We have shown that the electron dynamics are a superposition of Bloch oscillations and Zener tunnelings. The Bloch oscillations can be understood both in velocity gauge and in length gauge. In the velocity gauge, the lattice momentum of a Bloch state becomes time-dependent through the vector potential of the field. Because the allowed momenta of the electron in the solid are confined in the first Brillouin zone, the time-dependent lattice momentum traverses the first Brillouin zone periodically while the field is on. This periodic behavior is the Bloch oscillation. In the length gauge, the delocalized Bloch state can be written as a superposition of all the localized Wannier-Stark states. The Bloch oscillations then can be thought of as a quantum beating of this superposition. We have also showed that Zener tunneling is the part of the wave packet that tunnels through the band gap into other bands, and that it strongly depends on the sharpness of avoided crossing near the band gap. In the following chapters we will discuss our main results in the harmonic generation of a solid in a laser pulse. The concepts we

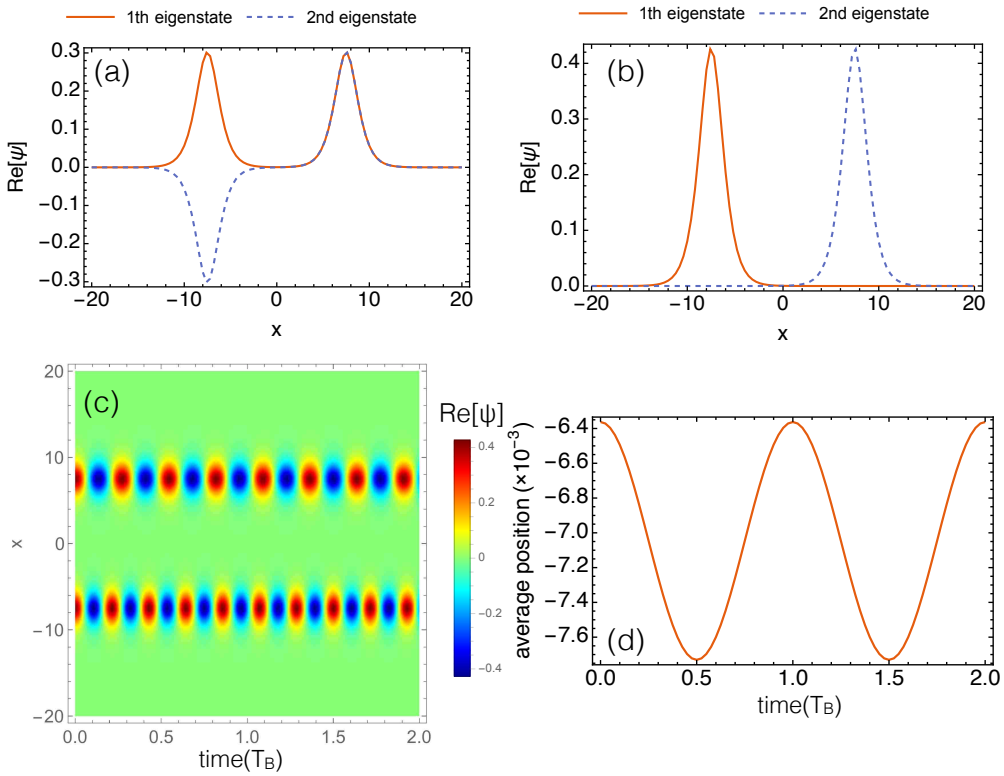

Figure 7.12: Wave function in quantum double-well. (a,b) shows the first two eigenstates of the double-well without and with field. (c) shows the evolution of the wave function with a DC field. The initial wave function is one of the eigenstate without the field. Notice the slightly different oscillation frequencies of the DC-field-dressed eigenstates. (d) The average position of the wave packet, oscillating at the Stark shift energy.

have laid down in this chapter such as Bloch oscillations and Zener tunneling will be the basic pictures to describe the electron dynamics there.

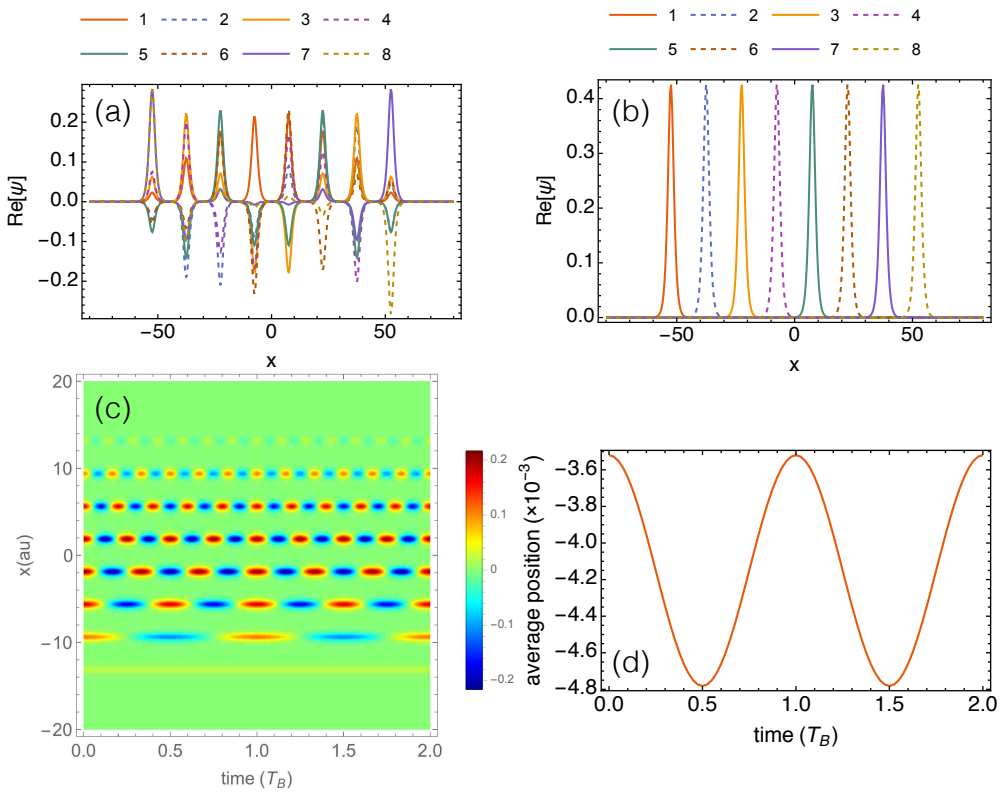

Figure 7.13: The same as in Fig. 7.12 except in a quantum 8-well. This analogizes to the Bloch oscillations in solids.

Chapter 8
Interaction of a solid with an AC field

8.1 Introduction

In the previous chapters, we discussed some of the basic concepts of the electron dynamics in a solid. The allowed energies for a single electron in a solid form the band structure, and they can be calculated by diagonalizing the single-electron Hamiltonian. The eigenstates of this Hamiltonian are Bloch states, which are delocalized in space throughout the solid. When applying a constant electric field, the electron traverses the first Brillouin zone periodically, and this periodic motion is called the Bloch oscillation. Bloch oscillations can be understood in both the velocity gauge as the acceleration of the lattice momentum and in the length gauge as the quantum beating between different Wannier-Stark states. We also showed that, in general, the dynamics are a combination of Bloch oscillations and Zener tunnelings on different bands.

In this chapter, we will focus on the studying of a single electron in a solid interacting with an AC field, which aims to model the high harmonic generation (HHG) process in solids by interacting with a mid-infrared laser. We will start from the time-dependent Schrödinger equation (TDSE) for an electron in a periodic potential, and discuss the two commonly used methods in solving the Schrödinger equation, namely in terms of Bloch states and Houston states. We will also show the harmonic spectrum from these two methods and present a physical interpretation for the origins of the harmonics, together with a simple formula for the high harmonic cutoff. Finally, we will draw a connection between the Houston treatment of the solid-laser system and a strongly driven two-level system.

8.2 Solving the TDSE in a Bloch state basis

8.2.1 Formalism

We consider a linearly polarized laser field propagating through a thin crystal along the optical axis. We describe the laser-solid interaction in one dimension, along the laser polarization which lies in the crystal plane. We follow the velocity gauge treatment in [76], in which the TDSE reads

$$i\hbar\frac{\partial}{\partial t}\left|\psi(t)\right\rangle = (\hat{H}_0 + \hat{H}_{\text{int}})\left|\psi(t)\right\rangle, \tag{8.1}$$

where H_0 is the field-free Hamiltonian and H_{int} is the interaction Hamiltonian between the laser and the electron

$$\hat{H}_0 = \frac{\hat{p}^2}{2m} + V(\hat{x}) \tag{8.2}$$

$$\hat{H}_{\text{int}} = \frac{e}{m} A(t)\hat{p}. \tag{8.3}$$

$A(t)$ is the vector potential, and is related to the electric field by

$$A(t) = -\int_{-\infty}^{t} E(t')dt'. \tag{8.4}$$

$\hat{p}$ is the momentum operator and $V(x)$ is the periodic lattice potential. We have employed the dipole approximation $A(x,t) \approx A(t)$ because the wavelengths we are interested in (μm) are much larger than the lattice constant (nm). According to Bloch's theorem, the eigenstates of the field-free Hamiltonian are the Bloch states

$$\hat{H}_0 \left|\phi_{nk}\right\rangle = \varepsilon_n(k) \left|\phi_{nk}\right\rangle, \tag{8.5}$$

where n is the band index and the eigenvalues $\varepsilon_n(k)$ represent the dispersion relationships of the bands. Each Bloch state can be written as a product of a plane wave and a function periodic in the lattice spacing a_0:

$$\langle x|\phi_{nk}\rangle = e^{ikx} u_{nk}(x), \tag{8.6}$$

where $u_{nk}(x)$ satisfy

$$u_{nk}(x + a_0) = u_{nk}(x). \tag{8.7}$$

Because the vector potential is independent of x, the lattice momentum k is still a good quantum number [94], which means the dynamics of the different lattice momentum channels are independent, and the TDSE can be solved independently for each k [76].

To solve the TDSE for a specific k_0, we express the wave function in Bloch states

$$\left|\psi_{k_0}(t)\right\rangle = \sum_n C_{nk_0}(t) \left|\phi_{nk_0}\right\rangle, \tag{8.8}$$

and solve for the time-dependent coefficients $C_{nk_0}(t)$

$$i\hbar \frac{\partial}{\partial t} C_{nk_0} = C_{nk_0}\varepsilon_n(k_0) + \frac{eA}{m} \sum_{n'} C_{n'k_0} p_{k_0}^{nn'}, \tag{8.9}$$

where the $p_{nn'}$ matrix element is the integration of the momentum operator over a lattice cell in space

$$\begin{aligned} p_{k_0}^{nn'} &= \langle \phi_{nk_0} | \hat{p} | \phi_{n'k_0} \rangle \\ &= \frac{1}{a_0} \int_0^{a_0} dx\, \phi_{nk_0}^*(x) \left(\frac{\hbar}{i} \frac{\partial}{\partial x} \right) \phi_{n'k_0}(x). \end{aligned} \tag{8.10}$$

Usually, the p matrix is dominated by its tri-diagonal matrix elements, which means the transitions to higher bands are most likely to happen through successive transitions between intermediate bands. Finally, we calculate the time-dependent laser-induced current as the sum of of the current in each of the different k_0 channels j_{k_0} [76] where :

$$j_{k_0} = -\frac{e}{m}\left[\mathrm{Re}\left[\langle\psi_{k_0}|\hat{p}|\psi_{k_0}\rangle\right] + eA(t)\right]. \tag{8.11}$$

Fourier transforming this current gives us the harmonic spectrum corresponding to that been measured in the experiments.

8.2.2 Harmonic spectrum

In this section, we use the formalism described above to calculate the harmonic spectrum for a 1D solid with a periodic potential $V(x) = -0.37(1+\cos(2\pi x/a_0))$ in atomic units with a lattice constant $a_0 = 8$ au. This periodic potential corresponds to a band gap of about 4.2 eV. The band structure of this potential is shown in Fig. 8.1. We have used 51 Bloch states in our expansion of the wave function, which means that 51 bands are included in the calculations for each k value. Since the lowest band (band 1) is deeply bound and very flat, we use the second band as the initially populated valence band. We have checked that transitions involving band 1 play a negligible role in the harmonic generation dynamics.

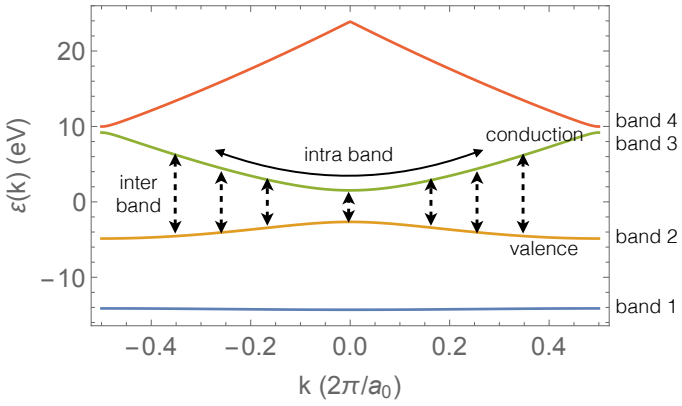

Figure 8.1: The band structure used in our calculation and the scheme of the inter-band and intra-band dynamics. The intra-band dynamics involves the motion of the electron on the same band, while inter-band dynamics describes the transitions of the electron between different bands. We regard the second band as the valence band and the third band as the conduction band. Taken from [95].

To begin with, the initial population is a small superposition ($\Delta k_0 = \pi/20a_0$) of Bloch states near $k_0 = 0$ on the valence band, corresponding to a wave function which is initially spatially delocalized through-out the solid. The laser pulse has a $\cos^4$ envelope in its electric field, with a full width at half maximum (FWHM)

pulse duration of 3 optical cycles for all the wavelengths. We have considered laser wavelengths λ between 2 μm and 5 μm, and intensities between 1×10^{10} W/cm^2 and 2×10^{12} W/cm^2. The harmonic spectrum is calculated as the modulus square $|j(\omega)|^2$ of the Fourier transform of the time-dependent current in Eq.(8.11). A window function is used in order to suppress the resonant dipole radiation that would otherwise dominate the spectrum in the region around the band-gap energy. The window function matches the envelope of the laser pulse.

Fig. 8.2 shows the harmonic spectra for our model system calculated using a laser wavelength $\lambda = 3.2$ μm and intensity 4.5×10^{11} W/cm^2. This corresponds to a Bloch frequency $\omega_B = Ea_0/\hbar = 0.78$ eV. Although this intensity is low compared to the experiment in [67], it is high enough to generate rich nonlinear dynamics. The harmonic spectrum exhibits both a perturbative regime (harmonic order < 10), a plateau regime ($10 \sim 30$) and a cutoff (~ 30), very similar to the general structure of the harmonic spectrum generated by atoms [6, 7]. As we will show in the following section, the plateau is due to inter-band transitions between the conduction and valence band. This agrees with the prediction in [70]. However, in contrast to that paper, we find that harmonics can be generated with photon energies well above the minimum and maximum band gap energies, as shown in Figs. 8.2.

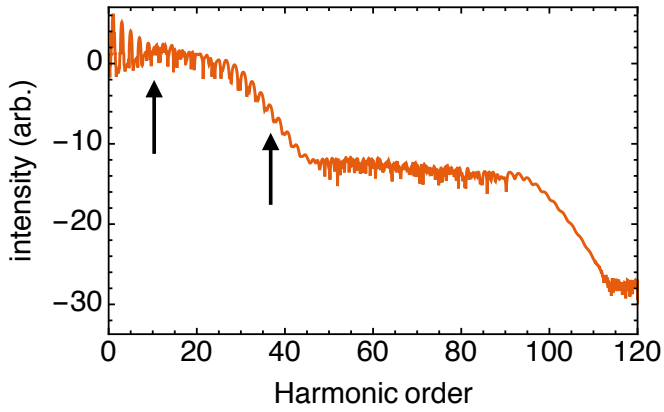

Figure 8.2: High harmonic spectra of the laser induced current calculated by solving the TDSE in the velocity gauge. The laser wavelength and peak intensity are 3.2 μm and 4.5×10^{11} W/cm^2. The black arrows indicate the minimum and maximum band gap energies.

8.2.3 Cutoff scaling

In this section we investigate the intensity and wavelength dependence of the harmonic plateau and cutoff. Fig. 8.3(a) shows the harmonic yield as a function of laser strength. The thick black lines indicate the minimum and the maximum of the band gap between the valence and conduction bands. The cutoff of the first and second plateaus are linear in the field strength, as indicated by the white dashed lines.

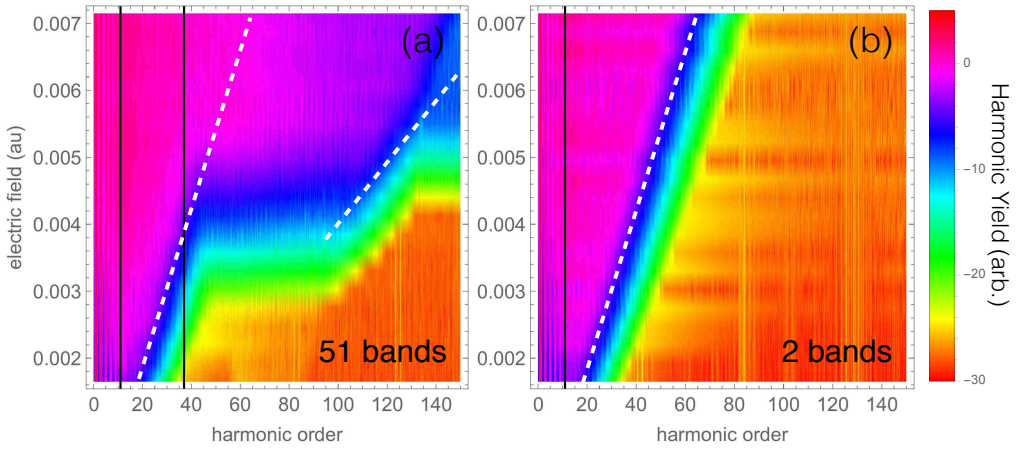

Figure 8.3: Harmonic yield as a function of electric field strength for $\lambda = 3.2\mu m$ using (a) 51 bands (b) 2 bands. The cutoff energy of each plateau is linear in the field strength. The two-band model can reproduce the 51-band model in the first plateau very well. The white dashed lines for the first plateau in (a) and (b) are for guiding the eye and they are identical. reprinted from [95] with permission.

Let's first focus on the first cutoff of the plateau. In order to investigate its origin, we perform a calculation using only the valence and the conduction bands, the result of which is shown in Fig. 8.3(b). This is done by using only the two out of the 51 Bloch states as a basis to propagate the TDSE. As we can see, the behavior of the first plateau is well reproduced by using only two bands. Notice that the white dashed lines for the first cutoff in the Fig. 8.3(a) and Fig. 8.3(b) are identical. The good reproduction of the first cutoff in the two-band model indicates that the first plateau comes from the dynamics involving only the valence and the first conduction band in this parameter regime.

Since our initial amplitude is only a small distribution around $k = 0$, the band gap for different k channels are about the same. In this sense, the two-band version of our model may be approximated as a two-level system. The harmonic cutoff in a two-level system can be written as [**?**]

$$E_{\text{cut}} = 2\sqrt{\Omega^2 + (\omega_0/2)^2}, \tag{8.12}$$

where Ω is the Rabi frequency between the two-level system and ω_0 is the two-level energy difference. By analogy, in the solid case, the Rabi frequency is proportional to the momentum operator matrix element between the valence and conduction band p_{vc} and the electric field F_0, so that the corresponding cutoff formula for the harmonic spectrum in a solid is

$$E_{\text{cut}} = 2\sqrt{\left(\frac{p_{vc}F_0}{\omega_L}\right)^2 + \left(\frac{\omega_{\text{gap}}}{2}\right)^2}, \tag{8.13}$$

where ω_L is the laser frequency and $\hbar\omega_{\text{gap}}$ is the band gap energy between the valence and conduction bands. For strong laser fields, the second term under the square-root

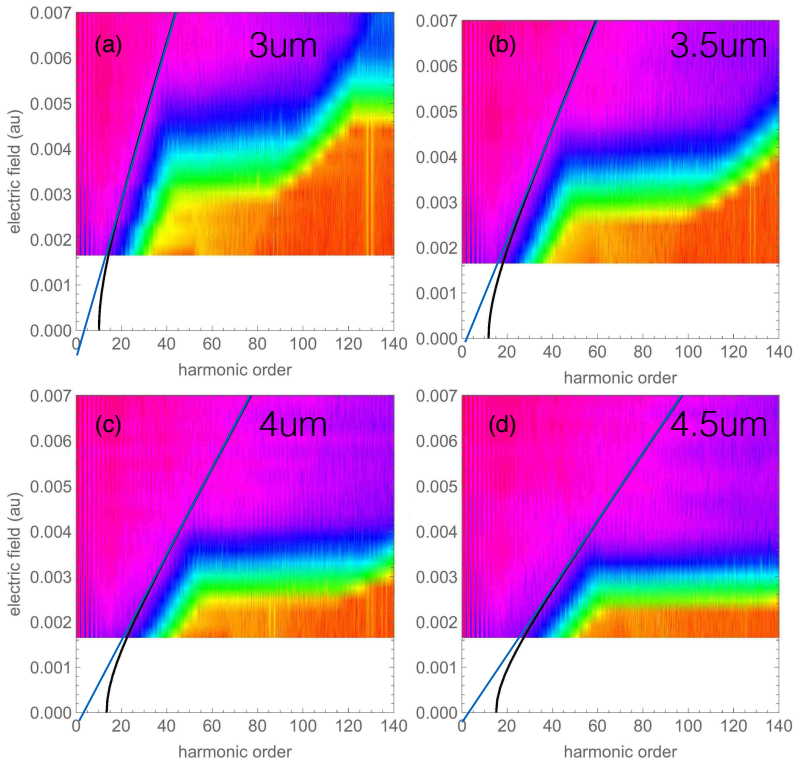

Figure 8.4: Intensity scan of harmonic yield in different wavelengths (a) 3 μm (b) 3.5 μm (c) 4 μm (a) 4.5 μm. Overlaid on top of the spectra are the prediction from the formula Eq. 8.13 in black and Eq. 8.14 in blue.

can be ignored and the cutoff energy is simply

$$E_{\text{cut}} = \frac{2p_{vc}F_0}{\omega_L} = \frac{p_{vc}}{\pi c}F_0\lambda. \tag{8.14}$$

Thus the cutoff energy in the solid harmonic spectrum is both linear in the electric field strength and the wavelength, where the proportionality constant is the momentum operator between the valence and conduction bands. This is very different than the cutoff scaling in gases where the cutoff is linear in intensity and wavelength squared.

In order to see how well this simple formula works, we overlay predictions from this simple formula onto intensity scans at four different wavelengths, as shown in Fig. 8.4. At each wavelength, the harmonic yield is plotted as a function of the electric field strength of the laser pulse. The cutoff energy from Eq. 8.13 is shown in blue and the cutoff energy from Eq. 8.14 is shown in Black. We can see that the simple cutoff formula generally works very well in predicting the cutoff of the first plateau of these wavelengths. One thing to notice is that this cutoff scaling predicts that the extrapolation of the cutoff scaling at large intensities will go through zero at zero field. This is another difference compared to HHG in gases where the extrapolation goes to the ionization potential [6, 7] at zero field. We will come back to this simple two-level model in the following sections when we explicitly compare the harmonic generation in a solid and that in a two-level system.

8.2.4 Initial condition for the Bloch state model

In concluding the discussion of harmonic generation in the Bloch state basis, we will discuss the initial condition used, where only a small number of lattice momentum near $k = 0$ is populated. This initial condition corresponds to an initial wave function which is spatially delocalized across the entire (1D) crystal. Other recent calculations have considered a different initial condition in which the valence band is initially fully populated [70,96], which in our model would correspond to an initial wave function localized at one particular lattice site. In this section, we will argue that our initial condition is a more reasonable choice for our single-active electron model.

Throughout the single-electron model we have discussed above, we solve the TDSE in the Bloch state basis. There is, however, another complete basis set, the Wannier states, can be used to describe the dynamics. The Wannier states are linear combinations of the Bloch states, and they are related by the Fourier transform

$$|W_{nr}\rangle = \frac{1}{a_0}\int_0^{a_0} |\phi_{nk}\rangle\, e^{-ikr} dk, \tag{8.15}$$

where $|\phi_{nk}\rangle$ is a Bloch state and $|W_{nr}\rangle$ is a Wannier states. Three Bloch states and Wannier states in space are shown schematically on the left and right column in Fig. 8.5, respectively. As we have described above, Bloch states are similar to plane waves and they are delocalized in space. The Wannier states, in the contrary, are localized in space, as can be seen on the right column of Fig. 8.5. Since the Wannier states and Bloch states are connected by the Fourier transform, both basis are complete in describing the dynamics, but the interpretation of the dynamics can sometimes be easier in one basis as compared to the other [97].

The Wannier states are not unique since we have the freedom to choose the phase factor e^{-ikr} in Eq. (8.15). As described in detail in [98] and sketched in Fig. 8.5, depending on how we choose the phase factor, the Wannier state can be localized at different lattice sites. For instance, if we take all the Bloch states in the left column in Fig. 8.5 and add them together, we get one of the localized Wannier states at the right column depending on the phase. This is also true for the opposite process, that if we add all the right column together, we get one of the Bloch states in the left column. So in this sense, a Bloch state is also a superposition of a number of Wannier states that are localized at every lattice site. Note that the Wannier states should not be confused with the Wannier-Stark states we discussed in the previous chapter when describing the Bloch oscillation in length gauge. There are two main differences between the Wannier states and the Wannier-Stark states. The first one is that the Wannier states are used for a field-free case, while Wannier-Stark states are used for a DC-field case. The second difference is that the Wannier states are not true eigenstates of the system themselves, but the Wannier-Stark states are.

In a real insulating material, the filled valence band means that all the different electronic states of the valence band are occupied by different electrons. The *full* valence band thus only has meaning in the multi-electron context. In a single-electron framework the valence band can never be filled in the same way, since we

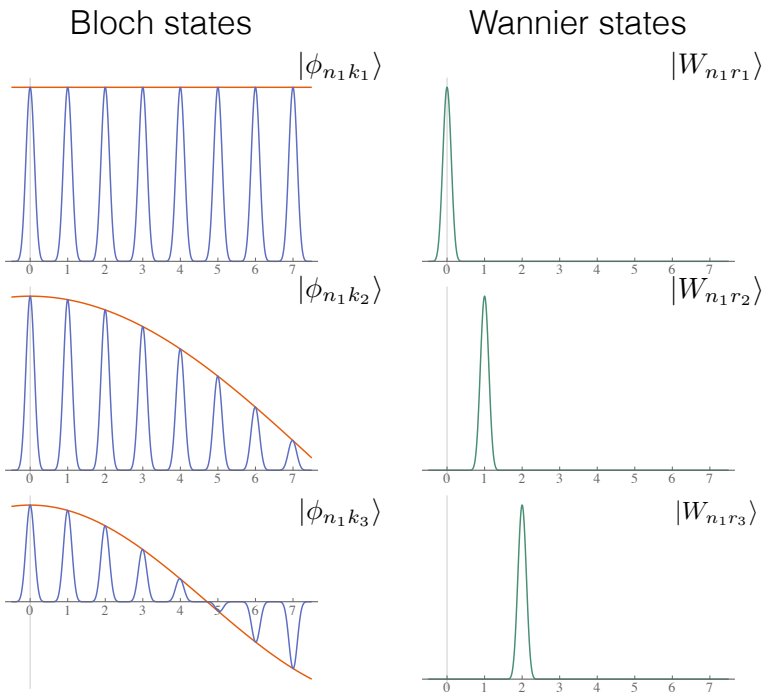

Figure 8.5: Scheme of Bloch states and Wannier states. The left column shows three Bloch states and the right column shows three Wannier states. The Bloch states are delocalized in space and localized in momentum space, while the Wannier states are localized in space and delocalized in momentum space.

only have one electron, which corresponds to a much lower dimensional Hilbert space than the multi-electron wave function. In this sense, in the single-electron framework the solid is modeled like a super-atom with a atomic potential that is periodic. What we can choose is only the initial wave function for this super-atom. For instance, we can choose the initial condition of the super-atom to be a Bloch state (few k's, spatially delocalized) or a Wannier state (many k's, spatially localized).

To argue that using Bloch states as the initial condition is more appropriate for the single-electron model, consider a simpler version of the problem in a quantum double-well system. Consider we have a super-atom with a double-well potential as shown in Fig. 8.6, and we are interested in the electron dynamics in this system. For this double well system, we have two eigenstates with opposite parities that are both delocalized into the two wells. We can also construct two localized wave function from linear combinations of these two delocalized eigenstates. Thus, for this double-well atom, we can either choose the initial wave packet localized at one well (Fig. 8.6(b) or (c)), or the initial wave packet spreading out to the two wells (Fig. 8.6(a)). From a symmetry point of view, the wave function spreading out is more fundamental and simpler. If we take the initial wave packet to be localized at one site, then it seems that we should also take the initial condition that localized at the other site and then sum the answers from those two. But the result from that combination is exactly as if we take the spreading wave packet as the initial condition in the first place. Similarly, using a full band as the initial condition in

the one-electron model for the solid seems more symmetric and reasonable.

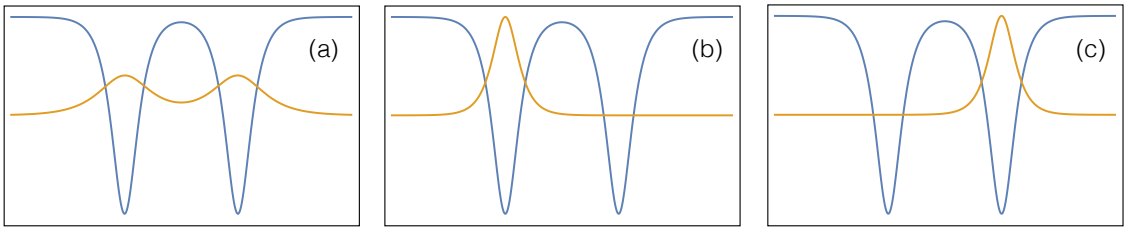

Figure 8.6: Representation of different initial conditions of the double-well potential. The blue curves represent the potential well, and the orange curves represent the initial wave function. The initial wave function are (a) delocalized, (b) localized at the first well and (c) localized at the second well. Similar to that of the Bloch state (a) and Wannier state (b) or (c) as the initial condition used for a SAE solid.

Another perspective to argue for our initial condition is that the localized Wannier state is not stable in a periodic potential. As we have discussed above, Wannier states are not the eigenstates of the laser-free potential, and they consist of Bloch states with different energies. This means that an initially localized Wannier state will soon dissipate in space. The rate of the dissipation is proportional to the width of the band and can be on the same order of the laser frequency in a typical semiconductor. For example, Fig. 8.7 (a) and (b) show the wave function evolution for a initial wave function that is localized over two and 20 lattice sites, respectively. It clearly shows that the initial wave function localized in 2 lattices spreads much faster than the wave function initially localized over 20 lattices. This suggests that the dynamics that would be initiated from a Wannier state would depend very much on the delay between the initial time when the Wannier state is localized and the time when the laser pulse arrives. For a typical laser pulse with a wavelength of 800 nm and a typical valence band with a width of 2 eV, the initially localized wave packet will spread out over nearly 100 lattice sites in 10 laser cycles. In this sense, using a stable initial state, such as a superposition of a few Bloch states, seems more reasonable and fundamental.

8.3 Solve the TDSE in Houston state basis

In the previous section, the electron dynamics was described in a static basis of Bloch states using the velocity gauge interaction. In this picture the time dependence of the wave function is due solely to the time dependence of the Bloch state coefficients $C_{nk}(t)$. Though computationally convenient, this method provides a time-dependent current which is hard to understand at an intuitive level. For example, the familiar Bloch oscillation of an electron with a momentum k_0 in a static field is built from the superposition of a large number of bands all at the same k_0. Obviously, in this picture there can be no separation of the current into intra-band and inter-band contributions.

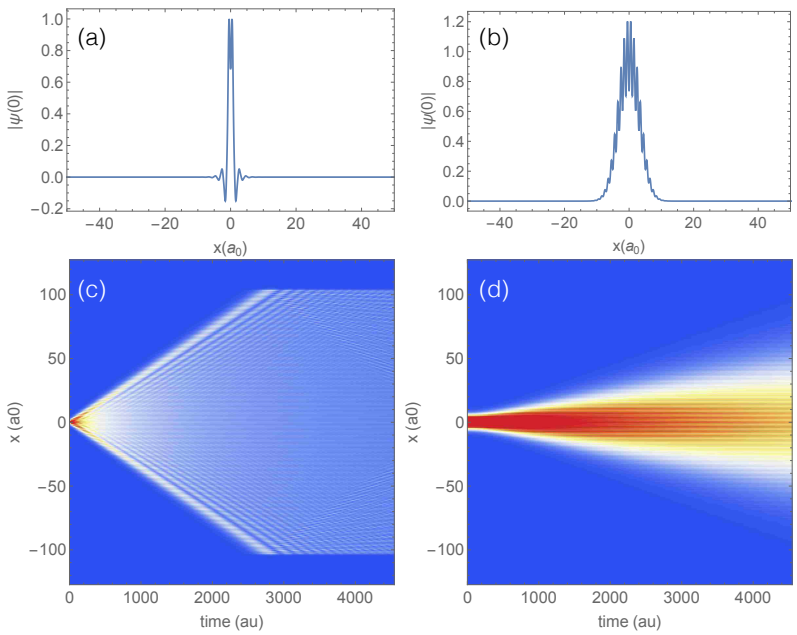

Figure 8.7: (a) shows the initial wave function that is localized over two lattice sites. (c) show the initial its time evolution when there is no laser field. (b,d) show the same as (a,c) but for a wave function initially spread over 20 lattice sites. The wave function dissipate much faster for the strongly localized initial wave packet.

In this section we describe an alternative way to calculate the electron dynamics using a time-dependent basis set, the Houston states [87]. As demonstrated in the following sections, the two solutions are equivalent, since they are related by a unitary frame transformation. In the Houston basis, however, we can obtain a separation of the induced current into intra- and inter-band components. This will allow us to separately explore the time-frequency characteristics of the two contributions, and show that they exhibit very different emission times.

The Houston states are best thought of as an adiabatic basis in which the lattice momentum that would be k_0 in the absence of a field has the time-dependence:

$$k(t) = k_0 + \frac{eA(t)}{\hbar}. \tag{8.16}$$

By construction the Houston states are the instantaneous eigenstates of the time-dependent Hamiltonian $H(t)$:

$$H(t)\,|\widetilde{\phi}_{nk_0}(t)\rangle = \varepsilon_n(k(t))\,|\widetilde{\phi}_{nk_0}(t)\rangle\,, \tag{8.17}$$

where $H(t)$ is the Hamiltonian in the same single-electron Schrödinger equation as above Eq. (8.1) [87] except for an additional term proportional to A^2:

$$i\hbar\frac{\partial}{\partial t}\,|\psi(t)\rangle = \left[\frac{(\hat{p}+eA)^2}{2m} + V(x)\right]|\psi(t)\rangle\,. \tag{8.18}$$

Including this term in the Schrödinger equation makes the form of the Houston states simpler, but it has no effects on the current since the wave function only differs by an overall time-dependent phase. In this convention, the Houston states are related to the Bloch states with lattice momentum $k(t)$ by [87]

$$|\widetilde{\phi}_{nk_0}(t)\rangle = e^{-ieA\hat{x}/\hbar}\,|\phi_{nk(t)}\rangle\,. \tag{8.19}$$

Expanding the time-dependent wave function with initial lattice momentum k_0 in Houston states

$$|\psi(t)\rangle = \sum_n a_{nk_0}(t)\,|\widetilde{\phi}_{nk_0}(t)\rangle\,, \tag{8.20}$$

we find equations of motion for the coefficients

$$i\hbar\frac{\partial a_{nk_0}}{\partial t} = \sum_{n'}\Big[\varepsilon_n(k(t))\delta_{nn'} - eE(t)X_{nn'}(k(t))\Big]a_{n'k_0}, \tag{8.21}$$

where we have made use of Eq. (8.4). $X_{nn'}$ is the inter-band transition matrix element defined by

$$X_{nn'}(k) = \frac{1}{ia_0}\int_0^{a_0} U^*_{nk}\frac{\partial}{\partial k}U_{n'k}dx, \tag{8.22}$$

and can be written in relation to the momentum operator [99]

$$X_{nn'}(k) = \begin{cases} i\frac{p_{nn'}(k)}{E_n - E'_n} & n' \neq n \\ 0 & n' = n \end{cases}. \tag{8.23}$$

The time-dependent Houston states describe the electron dynamics in a moving frame in which the lattice momentum is prescribed by the vector potential as in Eq. (8.16). Pictured in k space, one can think of an electron wave packet oscillating on each energy band, while at the same time some of the amplitude transitioning between different bands, corresponding to the intra- and inter-band dynamics, respectively. The motion on each band is governed by the time-dependent band structure $\varepsilon_n(k(t))$. For the intensity used in Fig. 8.2, the motion of the wave packet in k space samples about 2/3 of the first Brillouin zone.

The total current can be calculated from Eq. (8.11), using Eq. (8.20) for the wave function:

$$j_{\text{tot}} = -\frac{e}{m}\text{Re}\left[\sum_{nn'} a^*_{nk_0}a_{n'k_0}\,\langle\phi_{nk(t)}|\hat{p}|\phi_{n'k(t)}\rangle\right]. \tag{8.24}$$

Since now the system is described in the frame that moves along with the field, there is no A term in the expression for the current, as opposed to that of Eq. (8.11).

The calculation of the X matrix is not trivial [99]. Because the Bloch states are calculated from numerical diagonalizing the laser-free Hamiltonian, they are subject to random phases. These random phases will not effect the current and all other observables because they are all canceled out as we calculate the expectation values of the observables. However, since the Bloch oscillation and inter-band transitions

are not observables themselves, they do depend on these random phases. To ensure that the X matrix is calculated correctly, we first correct these random phases in the Bloch states before using them in Eq. (8.22). To correct the phases, we follow the prescription in [99] and first calculate an overlapping integral between the periodic part of the neighboring Bloch states:

$$z = \frac{1}{a_0}\int_0^{a_0} u_{n,k_{i+1}} u_{n,k_i} dx, \tag{8.25}$$

and then normalize the $u_{n,k_{i+1}}$ by

$$u_{n,k_{i+1}} = \frac{z^*}{|z|} u_{n,k_{i+1}}. \tag{8.26}$$

We start from the first set of Bloch states at one end of the Brillouin zone, and cascade this process until all the phases in all the Bloch states for different lattice momentum are fixed. A comparison between the X matrix calculated from the unfixed and fixed Bloch states are shown in Fig. 8.8, and we can see the process indeed works.

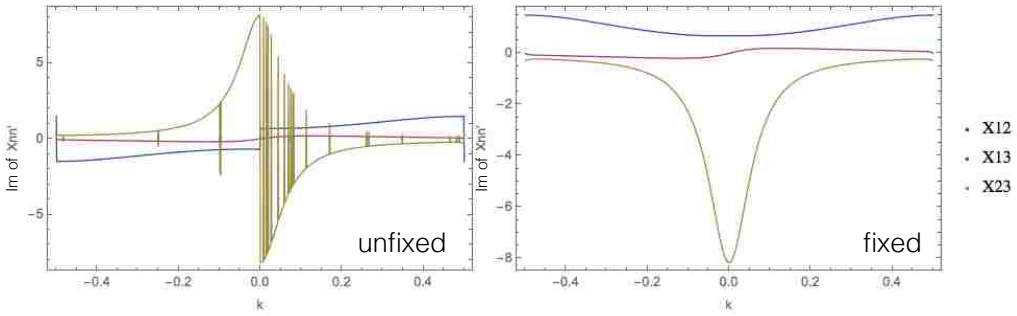

Figure 8.8: Compare the X matrix calculated without and with the phases fixed.

After we fix the phase of the Houston states, we can use them as a basis to calculate the time-dependent current. Fig. 8.9 shows the spectrum calculated in the Houston basis and compares it to that in the Bloch basis. In the Houston basis, we use three bands, while in the Bloch basis we use as many as 51 bands to calculate the band structure as are necessary for numerical convergence. The reason for using only three bands in the Houston basis will be discussed in following sections in connection with the numerical properties of the X matrix elements. The initial condition used in both cases is a single k state ($k = 0$) in the valence band where the band gap is the smallest. The band structure and laser parameters are the same as in Fig. 8.2. Fig. 8.9 shows that the calculation in the Houston basis agrees with that in the Bloch basis very well up to the 39th harmonic. This agreement is expected, since the two wave functions are related by a unitary transformation, as we will show in the next section.

One advantage of the Houston basis is that the electron dynamics naturally separate into an intra- and inter-band contribution, and can be studied separately.

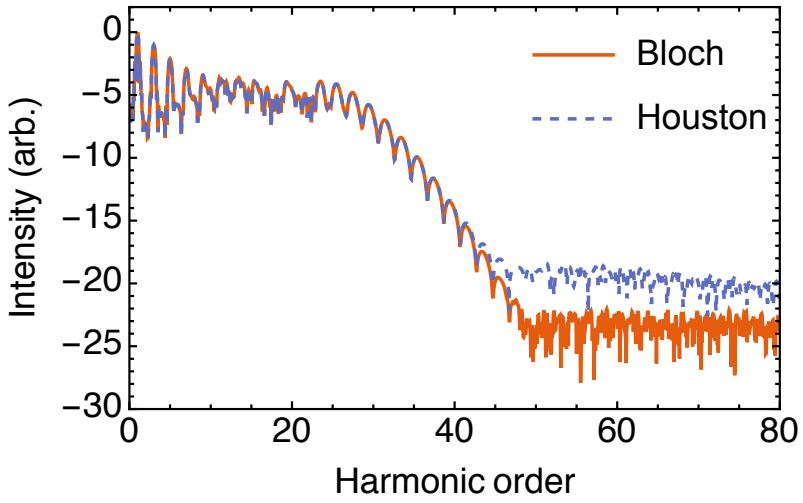

Figure 8.9: Comparison of a three-band Houston basis calculation and a 51-band Bloch basis calculation. The initial condition used in both cases here is a single $k = 0$ in the valence band. The band structure and laser parameters are the same as in Fig. 8.2. We can see the Houston basis calculation agrees with the Bloch basis very well up to 39th harmonic order. Note that for the Houston basis, we don't have the second plateau but merely a noise floor there.

In Eq. (8.24), the intra-band contribution to the current involves only Houston states on the same band ($n = n'$), whereas the inter-band contribution involves transitions between different bands ($n \neq n'$):

$$\begin{aligned} j_{\text{intra}} &= -\frac{e}{m}\sum_{n} |a_{nk_0}|^2 \langle \phi_{nk(t)}|\hat{p}|\phi_{nk(t)}\rangle \\ j_{\text{inter}} &= -\frac{e}{m}\text{Re}\left[\sum_{\substack{n,n' \\ n\neq n'}} a^*_{nk_0} a_{n'k_0} \langle \phi_{nk(t)}|\hat{p}|\phi_{n'k(t)}\rangle\right] \end{aligned} \tag{8.27}$$

The intra- and inter-band contributions to the current are shown in Fig. 8.10 (a). We find that the inter-band contribution to the plateau in the spectrum is stronger than the intra-band contributions by serval orders of magnitude in the plateau regime. This is in agreement with the prediction in [70]. In Fig. 8.10 (b), we show the intra-band contribution from the valence and conduction band separately. This is done by plotting separately the terms in the sum in Eq. (8.27). Note that the valence band contribution to the intra-band current has a generally perturbative behavior whereas that from the conduction band has a clear plateau. We can also show that the single conduction band model used in [67,100] comes naturally from the Houston model without inter-band transitions, as we will discuss in detail in the following sections.

In order to investigate the electron temporal dynamics using the Houston basis wave function, we perform a wavelet transform of the intra- and inter-band currents.

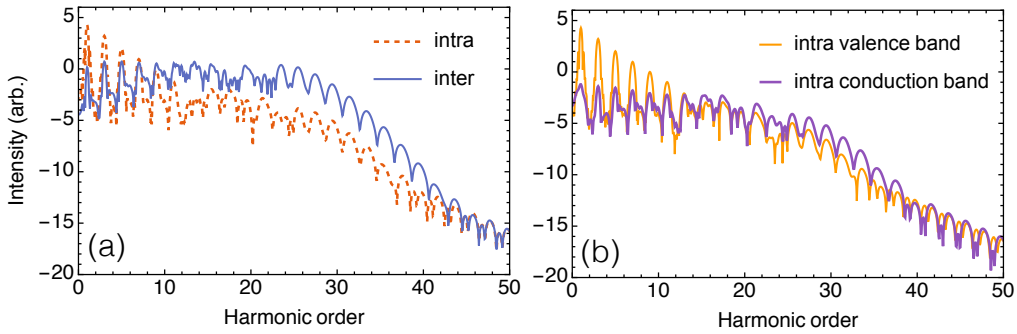

Figure 8.10: (a) The intra-band (red, dashed) and inter-band (blue, solid) current calculated using the Houston model. The low order harmonics mainly due to intra-band current while the harmonics in the plateau are mainly due to the inter-band current. (b) The valence band (orange) and conduction band (purple) contributions to the intra-band current. reprinted from [95] with permission.

The wavelet transform is similar to a windowed Fourier transform and provides the time-frequency information of the two contributions. In the wavelet transform we use an order 10 Gabor wavelet to achieve a balanced resolution in both the time and frequency domains. Fig. 8.11 shows the resulting time-frequency profiles for the two different contributions, which clearly exhibit two distinct types of dynamics. We will discuss these separately in the following.

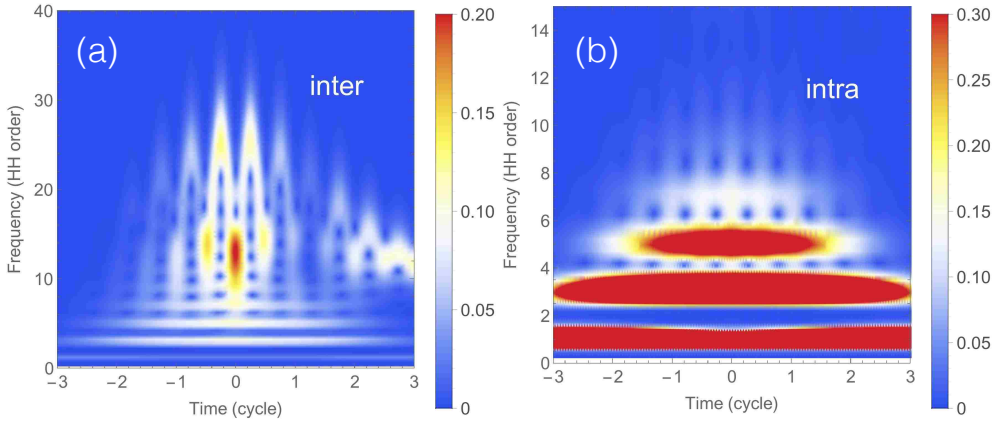

Figure 8.11: The wavelet transform of the intra-band and inter-band current of a Houston model. The harmonics generated from inter-band dynamics mainly happens at the peak of the vector potential and there is a clear chirp, while the harmonics generated from intra-band dynamics mainly happens at the peak of the field and don't have clear chirp. reprinted from [95] with permission.

The time structure of the inter-band current in Fig. 8.11(a), exhibits two emission times that are symmetrically placed around the peak of the vector potential in each half cycle. These two emission time profiles have opposite chirps, and are merged at the cutoff frequency. In the momentum picture we described above, these two

emission times arise from the fact that the lattice momentum $k(t)$, and thereby the time-dependent band gap $\varepsilon(k(t))$, traverses all allowed values twice in a half cycle. Since the two emission times contribute to the current with about the same strength, our model suggests that one or the other must be filtered out to obtain a train of identical attosecond pulses from the plateau. In contrast, harmonics near the cutoff frequency are generated near the time when the band gap $\varepsilon(k(t))$ is the largest, corresponding to the peaks of the vector potential in our case.

The time structure of the intra-band current Fig. 8.11(b), on the other hand, follows simply from the time-dependence of the band structure $\varepsilon(k(t))$, *i.e.*, the curvature of the bands. The emission times correspond to those times when the band has the largest curvature (the largest rate of change in the group velocity), which corresponds to the zeros of the vector potentials, as shown in Fig. 8.11(b). The time-frequency features of the intra-band current can also be seen from the cosine expansion of the conduction band in [67]

$$j_{\text{intra}}(t) = \sum_{s=1}^{\infty} D_s \sin\left[(2s-1)\omega t\right] \tag{8.28}$$

where D_s is related to the band structure and the strength of the field. From this expansion, it is clear that all the harmonics are generated at the same time and there is no chirp in the generated field. The differences in the two time-frequency characteristics could potentially be used as an experimental signature of the intra- and inter-band dynamics.

In conclusion, in this sub-section, we showed that the intra- and inter-band dynamics can be clearly separated, and they have very different time-frequency signatures. Moreover, we showed that the cutoff in the harmonic spectrum is tied to inter-band dynamics through the time-dependence of the population in the valence and conduction bands. We also showed that the spectrum calculated in the Houston basis agrees with that calculated in the Bloch basis.

8.4 The unitary transformation between solutions in the Bloch and Houston basis

In the previous section, we showed that harmonic spectrum calculated in Bloch state basis agrees with that calculated from Houston state basis. In this section, we will show that this agreement results from the fact that these two basis are connected by a unitary transformation. We will derive this unitary transformation matrix by matching the wave functions in these two basis.

In the Bloch state approach, we solve the TDSE in the velocity gauge, and the equation reads

$$i\hbar\frac{\partial}{\partial t}\left|\psi^B_{k_0}(t)\right\rangle = \left[\frac{p^2}{2m} + V(x) + \frac{eA(t)}{m}p\right]\left|\psi^B_{k_0}(t)\right\rangle, \tag{8.29}$$

where k_0 labels the single lattice momentum channel that we consider. The solution can be expressed in the basis of Bloch states

$$|\psi^B_{k_0}(t)\rangle = \sum_n c_n(t)\,|\phi_{nk_0}\rangle\,, \tag{8.30}$$

where c_n's are the time-dependent energy band amplitudes that this model solves for. In the Houston approach, TDSE reads

$$i\hbar\frac{\partial}{\partial t}\,|\psi^H_{k_0}(t)\rangle = \left[\frac{(p+eA(t))^2}{2m} + V(x)\right]|\psi^H_{k_0}(t)\rangle\,. \tag{8.31}$$

The wave function is expressed in the Houston states

$$|\psi^H_{k_0}(t)\rangle = \sum_n a_{nk_0}(t)\,|\widetilde{\phi}_{nk_0}(t)\rangle\,, \tag{8.32}$$

The Houston states are related to the Bloch states by [87]

$$|\widetilde{\phi}_{nk_0}(t)\rangle = e^{-ie\hat{x}A(t)/\hbar}\,|\phi_{nk(t)}\rangle\,. \tag{8.33}$$

We can then match the wave function in these two basis, and get the unitary transformation matrix between the expansion coefficients. Since $|\psi^B_{k_0}\rangle$ and $|\psi^H_{k_0}\rangle$ satisfy the Schrödinger equations that differ by a time-dependent A^2 term, they must be related by a phase factor

$$|\psi^B_{k_0}(t)\rangle = e^{-ie\Lambda/\hbar}\,|\psi^H_{k_0}(t)\rangle \tag{8.34}$$

where

$$\Lambda = -\frac{e}{2m}\int_0^t A^2(t')dt'. \tag{8.35}$$

Substitute Eq. (8.30) and Eq. (8.32) in to Eq. (8.34), we finally come to

$$a_{nk_0}(t) = e^{ie\Lambda/\hbar}\sum_{n'} c_{n'k_0}(t)\,\langle\phi_{nk(t)}|e^{ie\hat{x}A(t)/\hbar}|\phi_{n'k_0}\rangle\,. \tag{8.36}$$

The term $\langle\phi_{nk(t)}|e^{ie\hat{x}A(t)/\hbar}|\phi_{n'k_0}\rangle$ is the unitary transformation we are seeking. Using this unitary matrix, we can transform between the expansion coefficients in the Bloch and Houston basis. Note that this unitary transformation is very similar to the Kramers-Henneberger transformation in the atomic case, where a spatial transformation shifts the system into the accelerated frame, corresponding to the motion of a charged particle in the electric field [101]. The Kramers-Henneberger transformation is a transformation in space whereas the transformation here is in momentum space.

After calculating the Bloch states and the Houston states, the unitary transformation can be calculated from Eq. (8.36). Fig. 8.12 shows a plot of its matrix elements as a function of k, with the same parameters as that in Fig. 8.9. As a demonstration of this unitary transformation matrix, we use it to calculate the

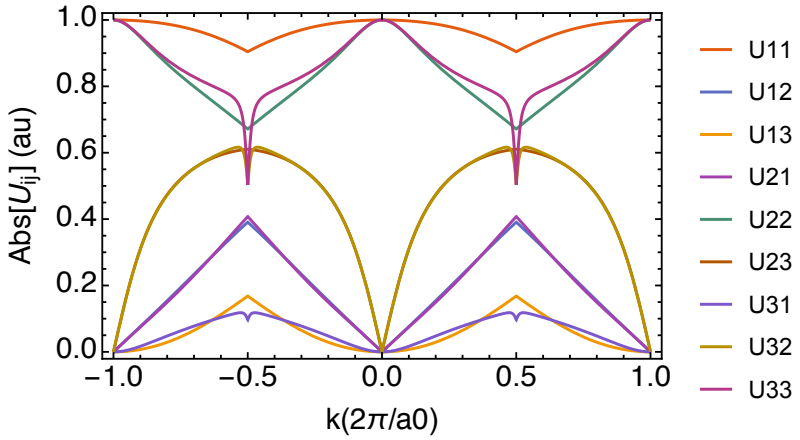

Figure 8.12: Plot of the matrix elements of the unitary transformation matrix that takes the solution in the Bloch state basis to that in the Houston state basis. In order to show the structure clearly, two Brillouin zones are plotted.

inter- and intra-band currents from the Bloch basis. This is done by taking the expansion coefficients in Bloch state basis and calculate those in the Houston state basis using the unitary transformation Eq. (8.36). Then we use Eq. (8.27) to calculate the inter- and intra-band currents. The currents calculated in this way is compared to those calculated directly in the Houston basis in Fig. 8.13, and they show a very good agreement.

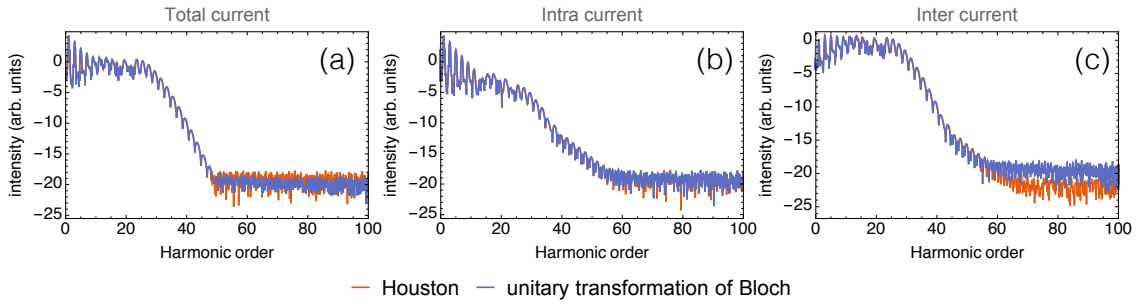

Figure 8.13: Compare the (a) total (b) intra-band (c) inter-band currents calculated directly in the Houston basis to those from the unitary transformation of currents in Bloch basis. They show very good agreements.

8.5 Connection of the single band model to the intra-band motion

In the original paper of high harmonic generation in solids experiment [67, 100], Ghimire *et. al.* proposed a single-band model accounting for the nonlinear current in the solids. In this section we will show that this single-band model is essentially a limiting case of the Houston model when the inter-band transitions are ignored.

If the inter-band dynamics is not allowed in the system, the inter-band transition matrix X vanishes in Eq. (8.21), and the population on each band stays the same as the initial condition. The solutions for Eq. (8.31) are exactly the Houston states apart from a phase

$$a_{nk_0}(t) = a_{nk_0}(0)e^{-\frac{i}{\hbar}\int_0^t \varepsilon_n(k(t'))dt'} \tag{8.37}$$

$$|\psi^H_{k_0}(t)\rangle = e^{-ieA(t)\hat{x}/\hbar}\sum_n a_{nk_0}(t)\,|\phi_{nk(t)}\rangle\,. \tag{8.38}$$

Substituting a_{nk_0} into Eq. (8.24) the total current is

$$j_{\text{tot}} = -\frac{e}{m}\sum_n |a_{nk_0}(0)|^2\,\langle\phi_{nk(t)}|\hat{p}|\phi_{nk(t)}\rangle\,. \tag{8.39}$$

If we consider the same situation as in [67, 100] where initially only the lowest conduction band is populated and other bands are empty, then the total current reduces to

$$j_{\text{tot}} = -\frac{e}{m}\,\langle\phi_{ck(t)}|\hat{p}|\phi_{ck(t)}\rangle\,. \tag{8.40}$$

This then reduces to the single conduction band model used in [67, 100], where the semi-classical current is derived from a group velocity

$$j_{\text{tot}} = -ev_g = -\frac{e}{\hbar}\,\frac{\partial\varepsilon_c}{\partial k}\bigg|_{k=k(t)}\,, \tag{8.41}$$

since the diagonal elements of the momentum operator is related to the band structure by

$$\langle\phi_{nk}|\hat{p}|\phi_{nk}\rangle = \frac{m}{\hbar}\frac{\partial\varepsilon_n}{\partial k}. \tag{8.42}$$

The proof of the last step can be found in many textbooks. For example, see chapter III in [102] or Appendix E in [72].

8.6 Numerical Difficulty in Houston Basis

In this section we will discuss the numerical difficulties of including more bands in Houston basis. As we include more bands, the band gap between high lying bands becomes very small, and the X matrix elements increase rapidly, which makes the numerical calculation difficult to converge. In this section we will first show this problem and then give some insights on the origin of this problem.

As we go to higher and higher bands, the band gap becomes smaller and smaller. An important consequence of the decrease of the band gap is the blow up of the X matrix at the avoided crossings and are almost zero at anywhere else. This is exactly the case as we try to calculate the X matrix directly, as shown in Fig. 8.14 (a). In fact, the X matrix seems to grow exponentially as a function of the number of bands, as shown in Fig. 8.14 (b). One can also expect the blow up of the X

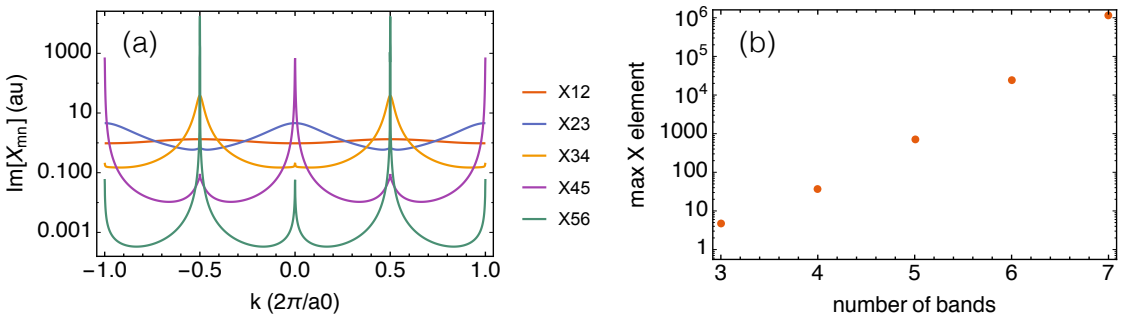

Figure 8.14: (a) The X matrix elements as a function of lattice momentum. (b) The largest element of X matrix as a function of the number of bands.

matrix from Eq. (8.23) where the band gap is in the denominator, which means the X matrix blows up as the band gap get smaller and smaller in high bands.

Since the X matrix is responsible for the inter-band transitions, in order to have the TDSE numerically converged, we have to use a time step that is small enough to resolve its largest matrix element

$$\Delta t \leq \frac{1}{2}\frac{2\pi}{X_{\max}\dot{A}}. \tag{8.43}$$

Apart from resolving the X matrix, the time step must be also small enough to resolve the largest band gap in the band structure. As the number of bands is increased, the requirement of the X matrix on the time step becomes the dominant one. For example, to include 7 bands, the highest X matrix element values requires a million time steps per laser cycle, which is about 3 order of magnitude more points than the usual case.

Another numerical problem encountered in the Houston basis is the discontinuity in the momentum operator matrix. As we go to high bands, the band structure has sharp turning points at the band center and band edge. These turning points result an almost discontinuous behavior of the momentum operator matrix element as shown in Fig. 8.15. This discontinuous behavior can also be expected from the relationship between the momentum operator and the derivative of the band structure Eq. (8.42). For higher bands, the slope of the band structure changes suddenly near the band center and band edge, giving almost discontinuities in the momentum operator at both of these points. In the previous section we have shown the unitary transformation between the Houston and the Bloch basis. Even we can get numerically stable results in the Bloch basis, the unitary transformation will not save us from the problem when transform into the Houston basis. This is because the unitary matrix itself is illy behaved. It can be already seen in Fig. 8.12 that the unitary operator element will peak at the points where the bands form avoided crossings, this behavior will get worse as we go higher bands.

These numerical difficulties suggest that separation of the inter-band and intra-band dynamics may not be an optimal picture for an electron in the higher bands where Zener tunneling between the neighboring bands is so large that an electron

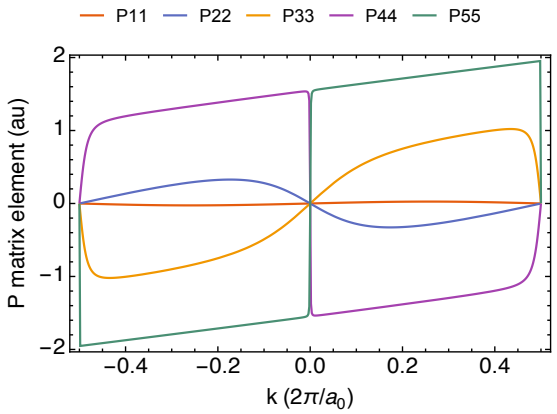

Figure 8.15: The diagonal part of the P matrix is approaching discontinuous as the bands get higher.

never performs solely intra-band motion, as sketched in Fig.8.16. Instead, it tunnels through the avoided crossing almost like a free electron [96]. The artificial separation of a Bloch oscillation motion from the almost free electron motion complicates the physical picture as well as makes the numerical calculation difficult. This separation is the underlying cause of the problematic behaviors of the p and X matrix shown in Fig. 8.14 and Fig. 8.15. This is also a general problem for studying strongly driven systems using an adiabatic basis. In these systems, the avoided crossings between the adiabatic states are so small that the transitions between them blow up.

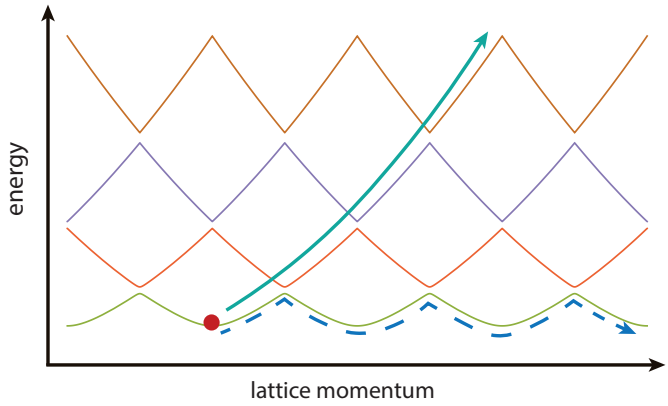

Figure 8.16: In high lying bands, the electron almost never perform solely Bloch oscillation (dashed line), but mainly tunnel the band gap like a free electron (solid line).

8.7 Analogy of the Houston treatment to a two-level system

In this section, we will drawn an analogy between the Houston state treatment of the laser-solid interaction and a strongly driven two-level system. Through this analogy, we will show that the intra- and inter-band dynamics in the solids are in fact the adiabatic and diabatic dynamics of the system, respectively. We will first setup the general formalism for describing the dynamics of a system in the adiabatic basis, and then use this formalism to solve a two-level system, from which a strong connection to the Houston basis treatment of the laser-solid system is made.

8.7.1 Formalism of adiabatic basis

The time-dependent Schrödinger equation for a general system reads

$$i\hbar \left|\dot{\psi}(t)\right\rangle = H(t) \left|\psi(t)\right\rangle , \tag{8.44}$$

and the adiabatic states are the instantaneous eigenstates of the time-dependent Hamiltonian

$$H(t) \left|\phi_n(t)\right\rangle = \mathcal{E}_n(t) \left|\phi_n(t)\right\rangle . \tag{8.45}$$

Note that the adiabatic states are time-dependent themselves, but they are orthogonal to each other at the same time

$$\langle \phi_n(t) | \phi_m(t) \rangle = \delta_{nm}, \tag{8.46}$$

and they form a complete basis set. This means the wave function can be expanded in this adiabatic basis as

$$\left|\psi(t)\right\rangle = \sum_n C_n(t) \left|\phi_n\right\rangle . \tag{8.47}$$

In the following, we will leave out the explicit indication of time-dependence of the adiabatic states and write $|\phi(t)\rangle$ as $|\phi\rangle$ for short. Substituting the wave function into the Schrödinger equation, we have

$$i\hbar \sum_n \dot{C}_n \left|\phi_n\right\rangle + i\hbar \sum_n C_n \left|\dot{\phi_n}\right\rangle = \sum_n C_n H \left|\phi_n\right\rangle . \tag{8.48}$$

Project on one of the adiabatic states, we have the equation for the expansion coefficients

$$i\hbar \dot{C_n} + i\hbar \sum_m C_m \left\langle \phi_n | \dot{\phi_m} \right\rangle = C_n \mathcal{E}_n. \tag{8.49}$$

To calculate the term $\langle \phi_n | \dot{\phi_m} \rangle$, we take the derivative of Eq. (8.45) and projecting on one of the adiabatic states

$$\begin{aligned} \dot{H} \left|\phi_m\right\rangle + H \left|\dot{\phi_m}\right\rangle &= \dot{\mathcal{E}}_m \left|\phi_m\right\rangle + \mathcal{E}_m \left|\dot{\phi_m}\right\rangle \\ \left\langle \phi_n | \dot{H} | \phi_m \right\rangle + \mathcal{E}_n \left\langle \phi_n | \dot{\phi_m} \right\rangle &= \dot{\mathcal{E}}_m \delta_{mn} + \mathcal{E}_m \left\langle \phi_n | \dot{\phi_m} \right\rangle . \end{aligned} \tag{8.50}$$

So we have

$$\langle \phi_n | \dot{\phi}_m \rangle = \begin{cases} -\frac{\langle \phi_n | \dot{H} | \phi_m \rangle}{\mathcal{E}_n - \mathcal{E}_m} & m \neq n \\ 0 & m = n \end{cases} . \tag{8.51}$$

We further write down the Hamiltonian as a sum of time-independent and time-dependent part

$$\begin{aligned} H(t) &= H_0 + H_I(t) \\ H_I(t) &= F(t) * \hat{X}, \end{aligned} \tag{8.52}$$

where H_0 is the laser free Hamiltonian, H_I is the interaction Hamiltonian, $F(t)$ is some general time-dependent force, and the $\hat{X}$ is the coupling operator that the force acts on. Substituting Eq. (8.51) and Eq. (8.52) into Eq. (8.49), the TDSE in the adiabatic basis can be written as

$$i\hbar \dot{C}_n = \sum_m \left[\mathcal{E}_m \delta_{mn} + \dot{F}(t) X_{mn}(t) \right] C_m, \tag{8.53}$$

where

$$X_{nm}(t) = \begin{cases} i\hbar \frac{\langle \phi_n | \dot{\hat{X}} | \phi_m \rangle}{\mathcal{E}_n - \mathcal{E}_m} & m \neq n \\ 0 & m = n \end{cases} \tag{8.54}$$

indicates the transition probabilities between the adiabatic states.

So in the adiabatic basis, studying the dynamics of the system is reduced to calculating the adiabatic states $|\phi\rangle$ and solving the coefficient equation Eq. (8.53). In the next section, we will use this formalism to study a two-level system and draw a connection to the Houston treatment of the solid-laser interaction system.

8.7.2 Two-level system in adiabatic basis

After setting up the general formalism for describing the dynamics in the adiabatic basis, we will now apply it to a two-level system for demonstration. The Hamiltonian for a two-level system can be written as

$$\begin{aligned} H(t) =& \hbar \begin{pmatrix} \frac{\omega_0}{2} & \Omega(t) \\ \Omega(t) & -\frac{\omega_0}{2} \end{pmatrix} \\ =& \hbar \sqrt{\frac{\omega_0^2}{4} + \Omega^2(t)} \begin{pmatrix} \cos\theta(t) & \sin\theta(t) \\ \sin\theta(t) & \cos\theta(t) \end{pmatrix}, \end{aligned} \tag{8.55}$$

where

$$\theta(t) = \tan^{-1}\left[\frac{2\Omega(t)}{\omega_0} \right], \tag{8.56}$$

and $\Omega(t)$ is the time-dependent Rabi frequency

$$\Omega(t) = \frac{\mu \cdot F(t)}{\hbar}. \tag{8.57}$$

The instantaneous eigenstates are

$$|\phi_1\rangle = \begin{pmatrix} -\sin\frac{\theta}{2} \\ \cos\frac{\theta}{2} \end{pmatrix}, |\phi_2\rangle = \begin{pmatrix} \cos\frac{\theta}{2} \\ \sin\frac{\theta}{2} \end{pmatrix}, \tag{8.58}$$

and the instantaneous eigenenergies are

$$\begin{aligned} \mathcal{E}_1 &= -\sqrt{\Omega^2(t) + \frac{\omega_0^2}{4}} \\ \mathcal{E}_2 &= +\sqrt{\Omega^2(t) + \frac{\omega_0^2}{4}}. \end{aligned} \tag{8.59}$$

Using Eq. (8.54), the X matrix is then

$$X = \frac{\omega_0 \dot{\Omega}(t)}{\omega_0^2 + 4\Omega^2(t)} \begin{pmatrix} 0 & -i \\ i & 0 \end{pmatrix}. \tag{8.60}$$

Fig. 8.17(a) and (b) show the energies of the two adiabatic states and the magnitude of the X matrix elements as a function of time. The time-dependent Rabi frequency used in these figures is

$$\Omega(t) = 1.6 \cos^6\left(\frac{\omega t}{16\pi}\right) \sin(\omega t) \tag{8.61}$$

and the driving frequency is very detuned

$$\omega = \omega_0/11. \tag{8.62}$$

The grid lines are placed at the times when the electric field crosses zero. At those times, the two adiabatic states form sharp avoided crossings as shown in Fig. 8.17(a) and the X matrix has sharp peaks as shown in Fig. 8.17(b). This behavior is expected from general physics about dynamics near avoided crossings. When the field is strong compared to the two-level energy spacing, the avoided crossings are very sharp so that the amplitude tunnels through the avoided crossings very easily, which means the transition probability between the two instantaneous eigenstates peaks at those places. As a result, the X matrix element is very large at the avoided crossings.

We can solve the TDSE in the adiabatic basis using Eq. (8.53), and the populations of the two adiabatic states are shown in Fig. 8.18. In this basis, the adiabatic process manifests itself as the populations staying the same, while the diabatic process manifests itself as the population changing abruptly. We can clearly see the diabatic process happens at the peaks of the field when the two states form avoided crossings. Between the avoided crossings the system evolves almost adiabatically, so the populations on the two instantaneous eigenstates stay almost the same. In summary, in the adiabatic basis, the evolution of the system is like this: When the system is far from the avoided crossings, it is almost stationary. The populations on the adiabatic states stays the same as a function of time. When the system is close to the avoided crossings, it evolves very diabatically, and the populations on the two adiabatic states change dramatically.

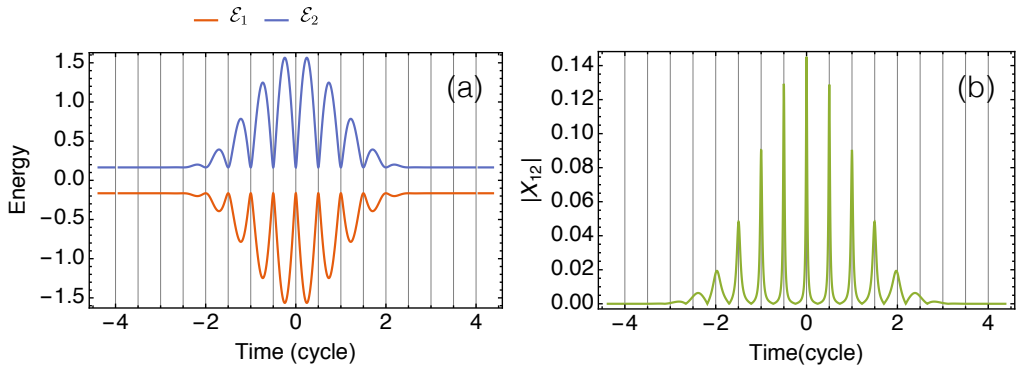

Figure 8.17: (a) The energies of the adiabatic states of the two-level system. At the peak of the field, the adiabatic states form avoided crossings. (b) The X matrix transition matrix element, which has sharp peaked at the avoided crossings. Grid lines indicate the zeros of the field.

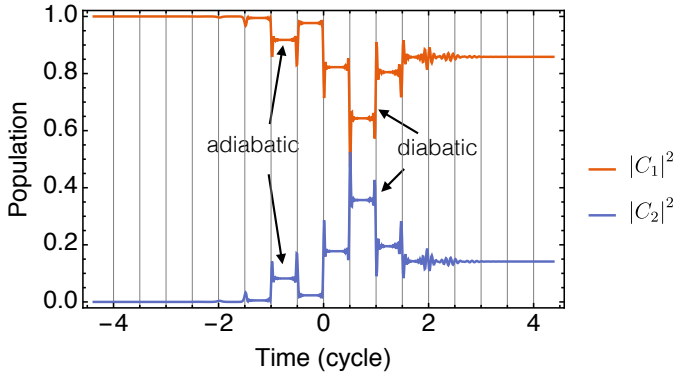

Figure 8.18: Amplitude on the adiabatic states as a function of time. As time when the adiabatic states form sharp avoided crossings, the amplitude jump suddenly, indicating the diabatic transitions. As times far from avoided crossings, the amplitudes are almost states the same, indicating the adiabatic following. Grid lines indicate the zeros of the field.

We can get additional insight by calculating the dipole moment in this basis. The time-dependent dipole moment is

$$d(t) = \langle\psi|\hat{D}|\psi\rangle \tag{8.63}$$

$$= \mathrm{Re}\left[\sum_{mn} C_m^* C_n \langle\phi_m|\hat{D}|\phi_n\rangle\right], \tag{8.64}$$

where $\hat{D}$ is the dipole operator. Similar to the separation of inter- and intra-band current in the solids, the two-level time-dependent dipole moment also can be sep-

arated into an adiabatic and a diabatic contributions

$$d(t) = d_{\mathrm{ad}}(t) + d_{\mathrm{da}}(t) \tag{8.65}$$

$$d_{\mathrm{ad}}(t) = \sum_n |C_n|^2 \langle \phi_n | \hat{D} | \phi_n \rangle \tag{8.66}$$

$$d_{\mathrm{da}}(t) = \mathrm{Re}\left[\sum_{\substack{m,n \\ m \neq n}} C_m^* C_n \langle \phi_m | \hat{D} | \phi_n \rangle \right]. \tag{8.67}$$

The adiabatic dipole moment involves the dynamics on the adiabatic states, while the diabatic dipole involves the transitions between different adiabatic states. This separation is essentially the same as the separation of the current into the intra- and inter-band contributions in the Houston treatment of the dynamics in solids. Fig. 8.19(a) shows the total dipole moment and Fig. 8.19(b) shows the adiabatic and diabatic dipole moment separately. Since there is no decay for the coherence in the simple two-level system, this diabatic coherence continuous after the pulse is ended.

The wavelet transforms (time-frequency analysis), as shown in the Fig. 8.20, giving more information on the high harmonics. In Fig. 8.20 we see that both the adiabatic and diabatic dipole moment can generate high harmonics. In particular, two-branch structures are presented in the diabatic dipole moment, and a harmonic cutoff can be read off at the joining of these two branches. The adiabatic harmonics, however, don't have this branch structure. Moreover, the harmonics are generated at different times in the laser cycle for the adiabatic and diabatic dipole moment. The diabatic harmonics are generated at peaks of the field while the adiabatic harmonics are generated at the zeros of the field. These structures in the wavelet spectrum of the diabatic and adiabatic dipole moment are very similar to that of the inter- and intra-band current shown in Fig. 8.11.

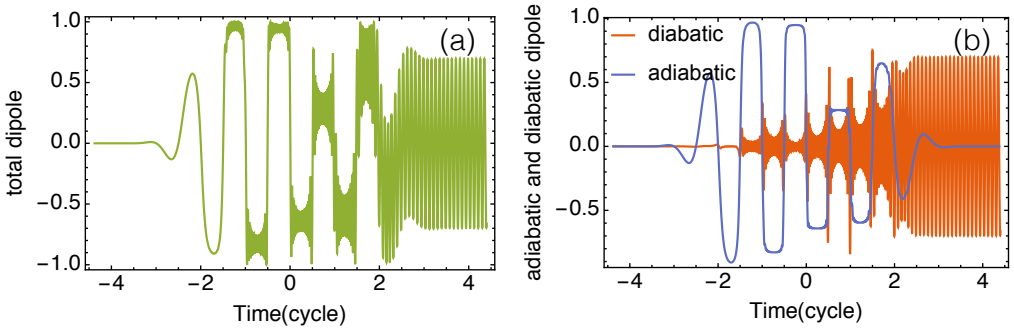

Figure 8.19: (a) The total time-dependent dipole. (b) The adiabatic and diabatic part of the dipole, analogy to the intra- and inter-band current.

From the above results of the two-level system, we see strong similarities to the laser-solid interaction system we described in previous sections of this chapter. First of all, in both systems there are avoided crossings. In the laser-solid system, the avoided crossings are in the band structure, while in the two-level system the

avoided crossings are in the instantaneous energies. Secondly, X matrix has sharp peaks in both systems at the avoided crossings, meaning that large population can tunnel through the avoided crossings easily. Thirdly, the dynamics in both system can be separated into an adiabatic part and a diabatic part. The adiabatic dynamics involves the evolution of the system along the adiabatic states. In the laser-solid system, this adiabatic dynamics is the intra-band motion (laser driven Bloch oscillations). The diabatic dynamics involves the transitions between the adiabatic states, corresponding to the inter-band motion in the laser-solid system. Finally, in both system both the adiabatic and diabatic dynamics can generate high harmonics, but the harmonics from the adiabatic motion are mainly generated at the zeros of the driving field, and the harmonics from the diabatic motions are mainly generated at the peaks of the driving field. And high harmonics in both system are dominated by the diabatic contribution. Note that the driving field is the electric field in the two-level case and vector potential in the laser-solid case.

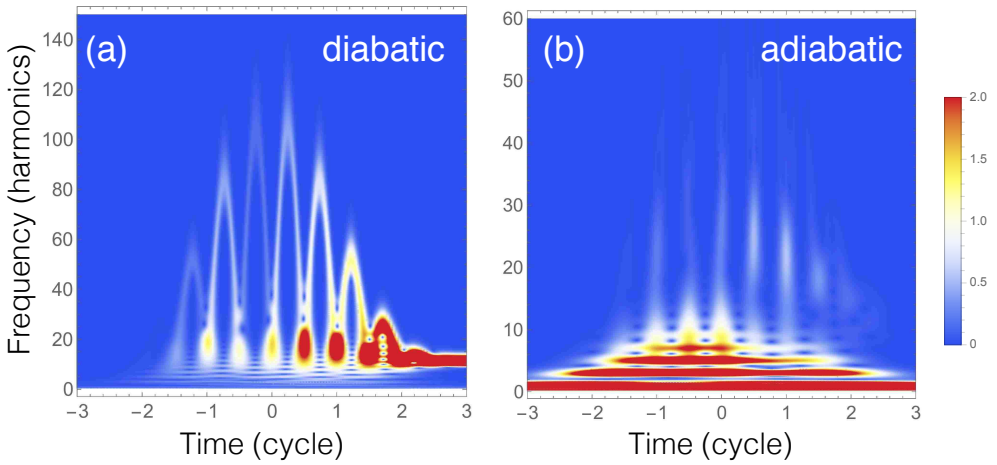

Figure 8.20: The wavelet transform of the diabatic and adiabatic dipole. Harmonics from diabatic dipole mainly generated at the peak of the field while harmonics from adiabatic dipole mainly generated at the zeros of the field. The structures are very similar to those in Fig. 8.11.

In summary, in this chapter, we have studied high harmonic generation in a model transparent solid using a 1D single-electron model and found that this system presents rich nonlinear dynamics. In the laser induced current, we see a high harmonic spectrum with multiple plateaus. Using the numerically robust Bloch basis, we have shown that the primary plateau is due to transitions between the valence band and the lowest conduction band, whereas the secondary plateau and more generally higher frequencies in the spectrum are due to contributions from higher lying bands. We find that the cutoff of the primary plateau scales linear in the field strength and the wavelength. We have also shown that the dynamics of our model system can be expressed in either the Bloch basis or the Houston basis, and solutions in these two basis are connected through a unitary transformation. The Houston basis allow for an intuitive separation of intra- and inter-band dynamics,

and we found that for moderate intensities the harmonic radiation is due primarily to inter-band dynamics. Finally, we showed that in dynamics in the Houston state picture is very similar to that of a strongly driven two-level system. Namely, the dynamics can be separated into a diabatic and an adiabatic part. The harmonic from the diabatic parts are mainly generated at the peaks of the field while the harmonics from the adiabatic parts are mainly generated from at the zeros of the field.

Bibliography

[1] P. Agostini and L. F. DiMauro. *The physics of attosecond light pulses.* Reports Prog. Phys. **67**, 813 (2004).

[2] L. Plaja. *Attosecond Physics*, volume 177 of *Springer Series in Optical Sciences.* Springer Berlin Heidelberg, Berlin, Heidelberg (2013).

[3] P. B. Corkum and F. Krausz. *Attosecond science.* Nat. Phys. **3**, 381 (2007).

[4] A. McPherson, G. Gibson, H. Jara, U. Johann, T. S. Luk, *et al. Studies of multiphoton production of vacuum-ultraviolet radiation in the rare gases.* J. Opt. Soc. Am. B **4**, 595 (1987).

[5] M. Ferray, A. L'Huillier, X. F. Li, L. A. Lompre, G. Mainfray, *et al. Multiple-harmonic conversion of 1064 nm radiation in rare gases.* J. Phys. B At. Mol. Opt. Phys. **21**, L31 (1999).

[6] K. J. Schafer, B. Yang, L. F. DiMauro, and K. C. Kulander. *Above threshold ionization beyond the high harmonic cutoff.* Phys. Rev. Lett. **70**, 1599 (1993).

[7] P. B. Corkum. *Plasma perspective on strong field multiphoton ionization.* Phys. Rev. Lett. **71**, 1994 (1993).

[8] P. M. Paul, E. S. Toma, P. Breger, G. Mullot, F. Auge, *et al. Observation of a train of attosecond pulses from high harmonic generation.* Science (80-.). **292**, 1689 (2001).

[9] M. Hentschel, R. Kienberger, C. Spielmann, G. a. Reider, N. Milosevic, *et al. Attosecond metrology.* Nature **414**, 509 (2001).

[10] E. Goulielmakis, Z.-H. Loh, A. Wirth, R. Santra, N. Rohringer, *et al. Real-time observation of valence electron motion.* Nature **466**, 739 (2010).

[11] A. Wirth, M. T. Hassan, I. Grguras, J. Gagnon, A. Moulet, *et al. Synthesized Light Transients* (2011).

[12] S. Baker, J. S. Robinson, C. A. Haworth, H. Teng, R. A. Smith, *et al. Probing proton dynamics in molecules on an attosecond time scale.* Science **312**, 424 (2006).

[13] H. Niikura, F. Légaré, R. Hasbani, M. Y. Ivanov, D. M. Villeneuve, *et al. Probing molecular dynamics with attosecond resolution using correlated wave packet pairs.* Nature **421**, 826 (2003).

[14] M. Uiberacker, T. Uphues, M. Schultze, a. J. Verhoef, V. Yakovlev, *et al. Attosecond real-time observation of electron tunnelling in atoms.* Nature **446**, 627 (2007).

[15] M. Drescher, M. Hentschel, R. Kienberger, M. Uiberacker, V. Yakovlev, *et al. Time-resolved atomic inner-shell spectroscopy.* Nature **419**, 803 (2002).

[16] P. Johnsson, J. Mauritsson, T. Remetter, a. LHuillier, and K. Schafer. *Attosecond Control of Ionization by Wave-Packet Interference.* Phys. Rev. Lett. **99**, 233001 (2007).

[17] H. N. Chapman, P. Fromme, A. Barty, T. a. White, R. a. Kirian, *et al. Femtosecond X-ray protein nanocrystallography.* Nature **470**, 73 (2011).

[18] M. M. Seibert, T. Ekeberg, F. R. N. C. Maia, M. Svenda, J. Andreasson, *et al. Single mimivirus particles intercepted and imaged with an X-ray laser.* Nature **470**, 78 (2011).

[19] J. R. Helliwell. *Biochemistry. How to solve protein structures with an X-ray laser.* Science **339**, 146 (2013).

[20] L. Redecke, K. Nass, D. P. DePonte, T. a. White, D. Rehders, *et al. Natively inhibited Trypanosoma brucei cathepsin B structure determined by using an X-ray laser.* Science **339**, 227 (2013).

[21] A. Schiffrin, T. Paasch-Colberg, N. Karpowicz, V. Apalkov, D. Gerster, *et al. Optical-field-induced current in dielectrics.* Nature **493**, 70 (2013).

[22] M. Schultze, E. M. Bothschafter, A. Sommer, S. Holzner, W. Schweinberger, *et al. Controlling dielectrics with the electric field of light.* Nature **493**, 75 (2013).

[23] T. Glover, M. Hertlein, S. Southworth, and T. Allison. *Controlling x-rays with light.* Nat. Phys. **6** (2009).

[24] F. Kelkensberg, C. Lefebvre, W. Siu, O. Ghafur, T. T. Nguyen-Dang, *et al. Molecular dissociative ionization and wave-packet dynamics studied using two-color XUV and IR pump-probe spectroscopy.* Phys. Rev. Lett. **103**, 123005 (2009).

[25] J. Mauritsson, T. Remetter, M. Swoboda, K. Klünder, a. LHuillier, *et al. Attosecond Electron Spectroscopy Using a Novel Interferometric Pump-Probe Technique.* Phys. Rev. Lett. **105**, 053001 (2010).

[26] G. Cerullo, C. Manzoni, L. Luer, and D. Polli. *Time-resolved methods in biophysics. 4. Broadband pump-probe spectroscopy system with sub-20 fs temporal resolution for the study of energy transfer processes in photosynthesis.* Photochem. Photobiol. Sci. **6**, 135 (2007).

[27] M. B. Gaarde, C. Buth, J. L. Tate, and K. J. Schafer. *Transient absorption and reshaping of ultrafast XUV light by laser-dressed helium.* Phys. Rev. A **83**, 013419 (2011).

[28] Z.-h. Loh and S. Leone. *Capturing Ultrafast Quantum Dynamics with Femtosecond and Attosecond Xray Core-Level Absorption Spectroscopy.* J. Phys. Chem. Lett. (2013).

[29] W. C. Chu and C. D. Lin. *Absorption and emission of single attosecond light pulses in an autoionizing gaseous medium dressed by a time-delayed control field.* Phys. Rev. A **87**, 013415 (2013).

[30] C. Ott, A. Kaldun, P. Raith, K. Meyer, M. Laux, *et al. Lorentz Meets Fano in Spectral Line Shapes: A Universal Phase and Its Laser Control.* Science (80-.). **340**, 716 (2013).

[31] A. Kaldun, C. Ott, A. Blättermann, M. Laux, K. Meyer, *et al. Extracting Phase and Amplitude Modifications of Laser-Coupled Fano Resonances.* Phys. Rev. Lett. **112**, 103001 (2014).

[32] A. Kaldun. *Fano Resonances in the Time Domain.* Ph.D. thesis (2014).

[33] A. Blättermann, C. Ott, A. Kaldun, T. Ding, and T. Pfeifer. *Two-dimensional spectral interpretation of time-dependent absorption near laser-coupled resonances.* J. Phys. B At. Mol. Opt. Phys. **47**, 124008 (2014).

[34] C. Ott, A. Kaldun, L. Argenti, P. Raith, K. Meyer, *et al. Reconstruction and control of a time-dependent two-electron wave packet.* Nature **516**, 374 (2014).

[35] A. R. Beck, D. M. Neumark, and S. R. Leone. *Probing ultrafast dynamics with attosecond transient absorption.* Chem. Phys. Lett. **624**, 119 (2014).

[36] S. Chen, M. J. Bell, A. R. Beck, H. Mashiko, M. Wu, *et al. Light-induced states in attosecond transient absorption spectra of laser-dressed helium.* Phys. Rev. A **86**, 063408 (2012).

[37] S. Chen, M. Wu, M. Gaarde, and K. Schafer. *Quantum interference in attosecond transient absorption of laser-dressed helium atoms.* Phys. Rev. A **87**, 033408 (2013).

[38] K. Klünder, P. Johnsson, M. Swoboda, a. L'Huillier, G. Sansone, *et al. Reconstruction of attosecond electron wave packets using quantum state holography.* Phys. Rev. A - At. Mol. Opt. Phys. **88**, 1 (2013).

[39] X. Li, B. Bernhardt, A. R. Beck, E. R. Warrick, a. N. Pfeiffer, *et al. Investigation of coupling mechanisms in attosecond transient absorption of autoionizing states: comparison of theory and experiment in xenon.* J. Phys. B At. Mol. Opt. Phys. **48**, 125601 (2015).

[40] M. Wu, S. Chen, M. B. Gaarde, and K. J. Schafer. *Time-domain perspective on Autler-Townes splitting in attosecond transient absorption of laser-dressed helium atoms.* Phys. Rev. A **88**, 043416 (2013).

[41] J. Herrmann, M. Lucchini, S. Chen, M. Wu, A. Ludwig, *et al. Multiphoton transitions for delay-zero calibration in attosecond spectroscopy.* New J. Phys. **17**, 013007 (2015).

[42] J. H. Eberly, R. Grobe, C. K. Law, and Q. Su. *Numerical Experiments in Strong and Super-Strong Fields.* In M. Gavrila (ed.), *Atoms in Intense Radiation Fields*, pp. 301–334. Academic Press, New York (1992).

[43] K. Schafer and K. Kulander. *High Harmonic Generation from Ultrafast Pump Lasers.* Phys. Rev. Lett. **78**, 638 (1997).

[44] M. Lindberg and S. Koch. *Transient oscillations and dynamic Stark effect in semiconductors.* Phys. Rev. B **38**, 7607 (1988).

[45] S. Yan, M. T. Seidel, and H. S. Tan. *Perturbed free induction decay in ultrafast mid-IR pump-probe spectroscopy.* Chem. Phys. Lett. **517**, 36 (2011).

[46] S. Wolfram. *Ten Thousand Hours of Design Reviews* (2008).

[47] L. Allen. *Optical resonance and two-level atoms.* John Wiley \& Sons Inc (1975).

[48] S. H. Autler and C. H. Townes. *Stark effect in rapidly varying fields.* Phys. Rev. **100**, 703 (1955).

[49] M. O. Scully and M. S. Zubairy. *Quantum Optics.* Cambridge University Press (1997).

[50] D. Griffiths. *Introduction to Quantum Mechanics.* Pearson Prentice Hall, 2 edition (2005).

[51] J. Shirley. *Solution of the Schrödinger equation with a Hamiltonian periodic in time.* Phys. Rev. **138**, B979 (1965).

[52] S.-K. Son, S. Han, and S.-I. Chu. *Floquet formulation for the investigation of multiphoton quantum interference in a superconducting qubit driven by a strong ac field.* Phys. Rev. A **79**, 032301 (2009).

[53] M. Grifoni and P. Hänggi. *Driven quantum tunneling.* Phys. Rep. **304**, 229 (1998).

[54] S.-I. Chu and D. a. Telnov. *Beyond the Floquet theorem: generalized Floquet formalisms and quasienergy methods for atomic and molecular multiphoton processes in intense laser fields.* Phys. Rep. **390**, 1 (2004).

[55] T. Brabec and F. Krausz. *Intense few-cycle laser fields: Frontiers of nonlinear optics.* Rev. Mod. Phys. **72**, 545 (2000).

[56] F. Krausz and M. Ivanov. *Attosecond physics.* Rev. Mod. Phys. **81**, 163 (2009).

[57] O. Smirnova, Y. Mairesse, S. Patchkovskii, N. Dudovich, D. Villeneuve, *et al. High harmonic interferometry of multi-electron dynamics in molecules.* Nature **460**, 972 (2009).

[58] H. J. Wörner, J. B. Bertrand, D. V. Kartashov, P. B. Corkum, and D. M. Villeneuve. *Following a chemical reaction using high-harmonic interferometry.* Nature **466**, 604 (2010).

[59] T. Morishita, A. T. Le, Z. Chen, and C. D. Lin. *Accurate retrieval of structural information from laser-induced photoelectron and high-order harmonic spectra by few-cycle laser pulses.* Phys. Rev. Lett. **100**, 1 (2008).

[60] Wikipedia. *High harmonic generation — Wikipedia, The Free Encyclopedia* (2015). [Online; accessed 27-May-2015].

[61] K. Midorikawa. *High-order harmonic generation and attosecond science.* Jpn. J. Appl. Phys. **50**, 090001 (2011).

[62] X. Zhang, A. L. Lytle, T. Popmintchev, X. Zhou, H. C. Kapteyn, *et al. Quasi-phase-matching and quantum-path control of high-harmonic generation using counterpropagating light.* Nat. Phys. **3**, 270 (2007).

[63] M. Zepf, B. Dromey, M. Landreman, P. Foster, and S. M. Hooker. *Bright quasi-phase-matched soft-X-ray harmonic radiation from argon ions.* Phys. Rev. Lett. **99**, 143901 (2007).

[64] J. Seres, V. S. Yakovlev, E. Seres, C. Streli, P. Wobrauschek, *et al. Coherent superposition of laser-driven soft-X-ray harmonics from successive sources.* Nat. Phys. **3**, 878 (2007).

[65] V. Tosa, V. S. Yakovlev, and F. Krausz. *Generation of tunable isolated attosecond pulses in multi-jet systems.* New J. Phys. **10**, 025016 (2008).

[66] E. a. Gibson, A. Paul, N. Wagner, R. Tobey, D. Gaudiosi, *et al. Coherent soft x-ray generation in the water window with quasi-phase matching.* Science (80-.). **302**, 95 (2003).

[67] S. Ghimire, A. D. DiChiara, E. Sistrunk, P. Agostini, L. F. DiMauro, *et al. Observation of high-order harmonic generation in a bulk crystal.* Nat. Phys. **7**, 138 (2011).

[68] J. P. Marangos. *High-harmonic generation: Solid progress.* Nat. Phys. **7**, 97 (2011).

[69] G. Farkas and C. Tóth. *Observation of multiple-harmonic radiation induced from a gold surface by picosecond neodymium-doped yttrium aluminum garnet laser pulses.* Phys. Rev. A **46**, 1 (1992).

[70] G. Vampa, C. R. McDonald, G. Orlando, D. D. Klug, P. B. Corkum, *et al. Theoretical Analysis of High-Harmonic Generation in Solids*. Phys. Rev. Lett. **113**, 073901 (2014).

[71] T. Higuchi, M. I. Stockman, and P. Hommelhoff. *Strong-Field Perspective on High-Harmonic Radiation from Bulk Solids*. Phys. Rev. Lett. **113**, 213901 (2014).

[72] N. W. Ashcroft and N. D. Mermin. *Solid state physics*. Holt, Rinehart and Winston, New York (1976).

[73] G. H. Wannier. *Elements of solid state theory*. University Press, Cambridge England (1960).

[74] M. A. Omar. *Elementary Solid State Physics: Principles and Applications*. Addison-Wesley, 4 edition (1994).

[75] J. C. Slater. *A soluble problem in energy bands*. Phys. Rev. **87**, 807 (1952).

[76] M. Korbman, S. Yu Kruchinin, and V. S. Yakovlev. *Quantum beats in the polarization response of a dielectric to intense few-cycle laser pulses*. New J. Phys. **15**, 013006 (2013).

[77] R. Aldrovandi and J. G. Pereira. *An Introduction to Geometrical Physics*. World Scientific Pub Co Inc (1995).

[78] B. M. Breid, D. Witthaut, and H. J. Korsch. *BlochZener oscillations*. New J. Phys. **8**, 110 (2006).

[79] M. Glück, A. Kolovsky, and H. Korsch. *Bloch Particle in the Presence of dc and ac Fields: Statistics of the Wigner Delay Time*. Phys. Rev. Lett. (1999).

[80] M. Abramowitz and I. A. Stegun. *Handbook of Mathematical Functions with Formulas, Graphs, and Mathematical Tables*, volume 56. Courier Corporation (1964).

[81] M. Trott. *The Mathematica GuideBook for Symbolics*. Springer (2005).

[82] M. Lewenstein, P. Balcou, M. Y. Ivanov, A. L'Huillier, and P. B. Corkum. *Theory of high-harmonic generation by low-frequency laser fields*. Phys. Rev. A **49**, 2117 (1994).

[83] E. E. Mendez and G. Bastard. *Wannier-Stark Ladders and Bloch Oscillations in Superlattices*. Phys. Today **46**, 34 (1993).

[84] F. Rossi. *Bloch oscillations and WannierStark localization in semiconductor superlattices*. Theory Transp. Prop. Semicond. ... (1998).

[85] M. Raizen, C. Salomon, and Q. Niu. *NEW LIGHT ON QUANTUM transport*. Phys. Today pp. 30–34 (1997).

[86] J. N. Churchill and F. E. Holmstrom. *Energy States and Bloch States for an Accelerated Electron in a Periodic Lattice.* Phys. Scr. **27**, 91 (1983).

[87] J. Krieger and G. Iafrate. *Time evolution of Bloch electrons in a homogeneous electric field.pdf.* Phys. Rev. B **33**, 5494 (1986).

[88] E. Schöll. *Theory of Transport Properties of Semiconductor Nanostructures (Electronic Materials Series)* (1998).

[89] R. H. Silsbee. *Simulations for Solid State Physics: An Interactive Resource for Students and Teachers, Volume 1.* Cambridge University Press, Cambridge England (1997).

[90] T. Hartmann, F. Keck, H. J. Korsch, and S. Mossmann. *Dynamics of Bloch oscillations.* New J. Phys. **6**, 2 (2004).

[91] H. Liu and F. Capasso. *Intersubband transitions in quantum wells: physics and device applications*, volume 40 of *European Materials Research Society Symposia Proceedings.* Elsevier (1999).

[92] O. D. Mücke. *Isolated high-order harmonics pulse from two-color-driven Bloch oscillations in bulk semiconductors.* Phys. Rev. B **84**, 81202 (2011).

[93] V. Apalkov and M. I. Stockman. *Theory of dielectric nanofilms in strong ultrafast optical fields.* Phys. Rev. B **86**, 165118 (2012).

[94] M. Holthaus and D. Hone. *Quantum wells and superlattices in strong time-dependent fields.* Phys. Rev. B **47**, 6499 (1993).

[95] M. Wu, S. Ghimire, D. a. Reis, K. J. Schafer, and M. B. Gaarde. *High-harmonic generation from Bloch electrons in solids.* Phys. Rev. A **91**, 043839 (2015).

[96] P. G. Hawkins, M. Y. Ivanov, and V. S. Yakovlev. *Effect of multiple conduction bands on high-harmonic emission from dielectrics.* Phys. Rev. A **91**, 013405 (2015).

[97] N. Marzari, I. Souza, and D. Vanderbilt. *An introduction to maximally-localized Wannier functions.* Psi-K Newsl. pp. 129–168 (2003).

[98] N. Marzari, A. a. Mostofi, J. R. Yates, I. Souza, and D. Vanderbilt. *Maximally localized Wannier functions: Theory and applications.* Rev. Mod. Phys. **84**, 1419 (2012).

[99] U. Lindefelt, H.-E. Nilsson, and M. Hjelm. *Choice of wavefunction phases in the equations for electric-field-induced interband transitions.* Semicond. Sci. Technol. **19**, 1061 (2004).

[100] S. Ghimire, A. D. Dichiara, E. Sistrunk, G. Ndabashimiye, U. B. Szafruga, *et al. Generation and propagation of high-order harmonics in crystals.* Phys. Rev. A **85**, 043836 (2012).

[101] F. Grossmann. *Theoretical Femtosecond Physics: Atoms and Molecules in Strong Laser Fields.* Springer Berlin Heidelberg (2008).

[102] N. F. Mott and H. Jones. *The theory of the properties of metals and alloys.* Dover Publications, New York (1958).

Vita

Mengxi Wu was born in Xishui city of Hubei province, People's Republic of China. He attended Huazhong University of Science and Technology at Wuhan and received a Bachelor of Science degree in Physics in July 2009. Afterwards, he began his graduate study at Louisiana State University in 2010 under supervision of Kenneth Schafer and Mette Gaarde. He will receive the degree of Doctor of Philosophy at August 2015 commencement.